ADDITIVELY MANUFACTURED LATTICES FOR ORTHOPEDIC IMPLANTS AND PROCESS MONITORING OF LASER-POWDER BED FUSION USING NEURAL NETWORKS

Thesis

Submitted to

The School of Engineering of the

UNIVERSITY OF DAYTON

In Partial Fulfillment of the Requirements for

The Degree of

Master of Science in Electrical Engineering

By

Dimitri Pierre Papazoglou

Dayton, Ohio

May 2019

ADDITIVELY MANUFACTURED LATTICES FOR ORTHOPEDIC IMPLANTS

AND PROCESS MONITORING OF LASER-POWDER BED FUSION

USING NEURAL NETWORKS

Name: Papazoglou, Dimitri Pierre

APPROVED BY:

Amy Doll, Ph.D., P.E.
Advisor, Committee Chairperson
Faculty of Practice, Department of
Electrical and Computer Engineering

Vamsy Chodavarapu, Ph.D., P.E.
Committee Member
Professor, Department of
Electrical and Computer Engineering

Guru Subramanyam, Ph.D.
Committee Member
Professor, Department of
Electrical and Computer Engineering

Dathan S. Erdahl, Ph.D.
Committee Member
Adjunct Professor, Department of
Mechanical Engineering
University of Dayton Research Institute

Robert J. Wilkens, Ph.D., P.E.
Associate Dean for Research and
Innovation
Professor, School of Engineering

Eddy M. Rojas, Ph.D., M.A., P.E.
Dean, School of Engineering

ABSTRACT

ADDITIVELY MANUFACTURED LATTICES FOR ORTHOPEDIC IMPLANTS AND PROCESS MONITORING OF LASER-POWDER BED FUSION USING NEURAL NETWORKS

Name: Papazoglou, Dimitri Pierre
University of Dayton

Advisor: Dr. Amy Doll

The call for orthopedic implants is a growing concern with a vastly enlarging elderly population and countries with developing healthcare, such as China and India. Lattice structures created by additive manufacturing offer patient specific orthopedic implants with viscoelastic properties similar to bone, less material consumption (such as titanium) and promotion of internal bone growth for better fixation. Patient specific lattices are possible with the onset of medical imaging technologies, allowing for custom additive manufacturing implants suited to each individual. Current orthopedic implants are restricted to numerous standard sizes, where a surgeon will choose between two or more sizes for implant insertion. An implant with better fitment will reduce complications and make the surgical process simpler. Two different biomimetic lattice structures with cubic and diamond strut geometries were printed in Ti-6Al-4V of an open architecture selective laser melting machine. These lattice structures varied in pore size of 400, 500, 600 and 900μm to mini varying densities of trabecular bone in-vivo. Properties needed to promote osseointegration were reviewed, such as pore size and lattice geometry. A convolutional

neural network was employed to detect defects and geometries during the selective laser melting process. Identifying defects and geometries is called process monitoring. Combining process monitoring, along with non-destruction evaluation such as computer tomography scanning and scanning electron microscope techniques, can properly identify defects for biomedical and aeronautical applications.

Dedicated to Mr. Quick, for instilling the possibilities of becoming an engineer into me, leading to eventual success of what was once deemed impossible by others.

This work is also dedicated to a certain guidance counselor from high school, providing "guidance" on my supposed inability of becoming an engineer due to my grades. Intelligence has nothing to do with becoming an engineer or anything worthwhile in life, for it all lays in perseverance. An ideology that cannot be taught but developed by an individual's thought patterns.

ACKNOWLEDGMENTS

A big thank you to my advisor, Dr. Amy Doll, for her expertise, guidance, patience and belief in my abilities in conducting research and implementing this thesis.

In addition, I would like to thank the following people for aiding me in my thesis work. Dr. Dathan Erdahl, Dr. Guru Subramanyam, Dr. Vamsy Chodavarapu, Jared Spletz and the group at University of Dayton Resarch Insitute, Dr. Eric Balster, Dr. Jason Kaufman, Dr. Bradley Ratliff, Dr. Margaret Pinnell, Eric Grimm, Monica Yeager, Nancy Striebich and Hamed Elwarfalli. Lastly, I'd like to thank Dr. Jordan B. Peterson for inspiring me to clean my room.

TABLE OF CONTENTS

LIST OF FIGURES

LIST OF TABLES

LIST OF ABBREVIATIONS AND NOTATIONS

μm	Micrometer
3D	Three-Dimensional Space
ADL	Activities of Daily Living
AM	Additive Manufacturing
ASTM	American Society for Testing and Materials
bFGF	basic Fibroblast Growth Factor
BMP	Bone Morphogenic Proteins
BoW	Bag-of-Words
BW	Body Weight
CAD	Computer Aided Design
CNN	Convolutional Neural Network
CT	Computer Tomography
CTGF	Connective Tissue Growth Factor
CYS	Compressive Yield Strength
DMLS	Direct Metal Laser Sintered
DPN	Deep Belief Network
EBM	Electron Beam Melting
ELI	Extra Low Interstitials
ERK	Extracellular Signal Regulated Kinases
FDA	Food and Drug Administration
FDM	Fused Deposition Modeling

FFT	Fast Fourier Transform
GPa	Gigapascal
HAP	Hydroxyapatite
HIF-1	Hypoxia Inducible Factor
HIP	Hot Isostatic Pressing
ICAM-1	Intercellular Adhesion Molecule-1
ICAM-2	Intercellular Adhesion Molecule-2
IL-8	Interleukin-8
iNOS	Inducible Nitric Oxide Synthase
IR	Infrared
ISO	International Organization for Standardization
LENS	Laser Engineer Net Shaping
LMD	Laser Metal Deposition
L-PBD	Laser-Powder Bed Fusion
MAPK	Mitogen Activated Protein Kinase
M-CSF	Macrophage Colony Stimulating Factor
mm	Millimeter
MPa	Megapascal
MPNN	Multilayer Perceptron Neural Networks
MsCNN	Multi-scale CNN
N	Newton
NDE	Non- Destructive Evaluation
Nm	Newton Meters

NO	Nitric Oxide
OL	One-legged
P/M	Powder Metallurgy
PAF	Platelet Activating Factor
PC	Principal Components
PCA	Principle Component Analysis
PCT	Principal Component Thermography
PDGF	Platelet-Derived Growth Factor
PF4	Platelet Factor 4
PMN	Poly Morphonuclear Leucocyte
PTH	Parathyroid Hormone
RANK	Receptor Activator of Nuclear Factor Kappa Beta
S1P	Chemokine Sphingosine 1 Phosphate
SDF-1	Stromal Cell Derived Factor
SEM	Scanning Electron Microscope
SLM	Selective Laser Melting
SLS	Selective Laser Sintering
STL	Stereolithography
TGF-β	Transforming Growth Factor Beta
THA	Total Hip Arthroplasty
TIMPs	Tissue Inhibitors of Metalloproteinases
TNF-alpha	Tumor Necrosis Factor alpha
TYS	Tensile Yield Strength

UCS	Ultimate Compression Strength
UTS	Ultimate Tensile Strength
VCAM-1	Vascular Cell Adhesion Molecule-1
VEGF	Vascular Endothelial Growth Factor

CHAPTER 1

INTRODUCTION

Orthopedic implants are used for a variety of medical applications, such as soft tissue repair, reconstruction/stabilization of the spine, fracture fixation, bone defects, tumor reconstruction and more [153]. The aging population are prime candidates for orthopedic implants due to musculoskeletal diseases and injuries that increase with age. A study on global orthopedic devices for the market of 2016-2020 revealed that markets will grow due to an increasing elderly population and the introduction of orthopedic technology into countries experiencing rapid economic and technical growth such as India, Brazil and China. Around 70% of the United States population from 55 to 75 years old suffer from osteoarthritis and rheumatoid arthritis is believed to affect 0.5-1% of worldwide population every year. The onset of osteoporosis and arthritis is common for ages 60 and higher, these orthopedic disease and disorders can lead to orthopedic implantation [154]. Obesity is known to cause soft tissue damage, osteoarthritis for the hip and knee regions, arthritis and various musculoskeletal health issues [155]. For 2016, 1.9 billion adults over the age of 18 were overweight, where 650 million were obese – these values have almost tripled since 1975 [156].

For over 200 years, various materials have been used for orthopedic implants. One of the first hip fixation implants was created around the 1800's. Early research in osteointegration conducted by Dr. Leventhal and Dr. Bothe in the 1940's lead to advances in bone and titanium integration Dr. Brånemark in the 1950's [157,158]. The ability to fixate skeletal

attachment with a metal substrate such as titanium was not possible until the work of osseointegration was discovered, where further advances such as dental implants, spinal fusion implants, total joint replacement and hip implants have seen long-term clinical success, greatly expanding the field of orthopedic implants. Various metals are now used to promote osseointegration, such as a stainless steel, tantalum, chromium and titanium [158] and research is still ongoing on the ideal structures that can promote osseointegration [140-148].

Laser-Powder Bed Fusion (L-PBF) is an Additive Manufacturing (AM) technology where 3D metallic objects are created in a layer-by-layer manner to replicated parts defined by a 3D-model created in Computer-Aided Design (CAD) software. Volumes of research have been documented on AM-created orthopedic implants [19,20,25,26,52,55-56,59-57]. The Food and Drug Administration (FDA) has also approved various AM orthopedic implants, such as cervical spacers [159] and spinal implants [160-163]. This approval from FDA further cements the future of AM for orthopedic implants. In 2016, the FDA acknowledged the importance of AM in medicine and orthopedics with a publication highlighting recent advances of the technology and the FDA's observations [164]. In 2017, the FDA also published "Technical Considerations for Additive Manufactured Medical Devices". In this document the FDA gives considerations for design and manufacturing of medical devices, device testing considerations and process validation. Process validation is where device qualities such as dimensions, mechanical properties and material characteristics are verified through applications of monitoring of input parameters and processing steps.

Process validation is performed to ensure medical devices have consistent quality throughout various AM technologies, most notably L-PBF.

These are the following monitoring methods the FDA recommends:

- temperature at the beam focus,
- melt pool data,
- build-space environmental conditions (e.g., temperature, pressure, humidity),
- power of the energy delivery system (e.g., laser, electron beam, extruder), and
- status of mechanical elements of the printing system (e.g., recoater, gantry)

In addition to the above monitoring methods, these methods should be validated with the use of:

- manual or automated visual inspection with defined acceptance criteria,
- non-destructive evaluation (see Section V.E.3 Verification), and
- test coupon evaluation (see Section V.E.4 Test Coupons).

This thesis features a type of process monitoring that involves awareness of build-space environmental conditions; along with identifying the importance of Non-Destructive Evaluation (NDE) coupled with process monitoring [197].

To properly design orthopedic implants, an understanding of human bone construction and its respective mechanical properties was reviewed. The onset of L-PBF has allowed the creation of complex structures, such as porous/lattice structures. The lattice structure is one of the key elements of this thesis, as its structure can be adjusted to approximate the mechanical properties and viscoelasticity of human bone [60]. Using L-PBF, customized lattice structures can be designed to match the ideal mechanical properties for a specific

patient, as well as to promote osseointegration. The osteogenesis process is highly influenced by surface area, pore size, and pore geometry. Volumes of research have been published highlighting different lattice designs, pore sizes and materials to promote osteogenesis [55,60,62,73,89,140-148].

As L-PBF is an emerging technology, defects will occur during production of 3D objects. NDE provides numerous techniques such as Computer Tomography (CT) scanning and Scanning Electron Microscope (SEM) to evaluate if parts have internal or surface defects, respectively [168-169]. In addition to NDE, *in situ* process monitoring may be performed on L-PBF parts to ensure defect-free parts. Process monitoring is utilization of machine learning algorithms to detect defects and geometries to ensure that parts meet a quality standard [165-167]. This definition of process monitoring aligns with the definition of the FDA's process validation. The long-term goal of *in-situ* process monitoring is to use the data in a closed-loop feedback control system to change machine parameters on the fly when defects are detected at an early stage in the build job.

The three main goals of this Master's thesis are:

1. Review various processes and information related to design of lattice structures for orthopedic implants, such as AM processes and biocompatible metallic materials, bone properties and bone mechanical properties, lattice structures and respective mechanical properties, and the osseointegration process and influence on lattice design

2. Validate two biomimetic lattice structures with varying strut geometries (diamond and cubic) and pore sizes (400µm, 500µm, 600µm, 900µm) additively manufactured in Ti-6Al-4V through post-process NDE via x-ray radiography and SEM.
3. Implement *in-situ* process monitoring of global infrared and infrared tomography via machine learning algorithms to recognize geometries during L-PBF. This use of these algorithms is to confirm that parts were built properly in comparison to the CAD design. Utilization of NDE and process monitoring can ensure parts are built properly for medical implants and other industries.

CHAPTER 2

ADDITIVE MANUFACTURING FOR ORTHOPEDIC IMPLANTS

Additive manufacturing is the creation of three-dimensional (3D) objects via incremental layer-by-layer manufacturing. Since the conception of AM in the late 80's, the field was deemed ideal for rapid prototyping due to the ability to quickly fabricate a scale model of a custom part using 3D CAD drawings. AM does have some downfalls, such as unsatisfactory cost, decreased lifecycle and/or mechanical performance, and longer production times when compared to conventional manufacturing methods [1]. Recent advances in the field of Laser-Powder Bed Fusion (L-PBF) have led to the ability to create metallic complex shapes and custom parts. This work is focused on manufacturing of biomedical implants via additive manufacturing, with a specialization in orthopedic implants with porous/lattice structures. AM for biomedical implants can be broken down into two categories: Powder Bed and Powder-Fed systems. Both of these categories are in relation to metal and metallic-alloy powders. Selective Laser Melting (SLM), Direct Metal Laser Sintered (DMLS), Selective Laser Sintering (SLS) and Electron Beam Melting [EBM] all fall under the powder bed category. Powder-fed systems consist of Laser Metal Deposition (LMD) and Laser Engineer Net Shaping (LENS) [2]. The only technologies that use raw metallic biomaterials are SLM, SLS, EBM and LENS. There are other non-L-PBF technologies that are used for biomedical devices. Stereolithography has applications in tissue scaffolds and implantable devices [3]. Fused Deposition Modeling (FDM) is a popular alternative for craniofacial reconstruction, orthopedic spacers and hip implants, although research has shifted to use of L-PBF [4,5].

2.1 Biocompatible Materials in Additive Manufacturing

There are many reasons why metal is ideal for biomedical implants. Metal used in layer-by-layer manufacturing can produce geometries not possible by conventional manufacturing means. The creation of lightweight and viscoelastic components is possible with metal via L-PBF, and the scalability of metal is useful in creation of lattice structures and hollow materials. These metals must be biocompatible with the human body. The standard of quality for these implants must be stringent; no lose powders can be present on or inside the implant, and various machine parameters such as laser power, scanning strategies, cooling rate and gas flow must be properly strategized to produce parts without defects, which is an ongoing effort of AM industry for L-PBF. The quality of the metallic powder quality, itself, influences part quality. A wider range of powder particle sizes can generate smoother surface finishes, whereas a narrower range of particle sizes can affect ultimate tensile strength and other material properties [17]. Fine particles melt better than coarse particles, resulting in improved scan surface quality, higher part densities and higher mechanical strength [18].

2.1.1 Ti-6Al-4V

A common material used in both standard orthopedic implants and L-PBF is Ti-6Al-4V. This titanium alloy is popular due to its high strength-to-weight ratio, biocompatibility, corrosion resistance and good fatigue resistance properties. The Young's modulus (a measure of material stiffness) of the alloy can be controlled via change of porosity and chemical composition, which is vital in reducing stress shielding in orthopedic implants. Biocompatibility of Ti-64 is due to the low electrical conductivity of the metal - this low

conductivity leads to electrochemical oxidation, causing formation of a thin passive oxide layer. The oxide layer is not affected by corrosion [6]. Titanium and its oxides have low reactivity with macromolecules and low ion-formation tendency, aiding in biocompatibility with the human body [7]. The passive oxide layer has pH values consistent with the human body, due to titanium's oxide isoelectric point of 5-6 in vivo [8]. AM-produced Ti-6Al-4V is shown to have adequate or better mechanical properties than conventional manufacturing for this alloy, such as higher tensile strength than cast or wrought Ti-6Al-4V [16]. Research on porous Ti-6Al-4V structures has demonstrated mechanical properties comparable to human bone. However, these properties can vary based on porosity levels [19]. Standards for Ti-6Al-4V in use for AM have been established as ASTM F2924 [9] and ASTM F3001 [10]. These standards are important as they certify this material for use in industry, which is important for medical implant adoption, research and FDA acceptance.

2.1.2 Cobalt-based Alloy

Used widely in general orthopedic implants, cobalt-based alloys have high wear resistance and good corrosion resistance [16]. Commonly used for dentistry applications [22], cobalt alloys have shown compatibility for orthopedic implants [20], used in hip bearings [21] and hip implants [23]. Biocompatible alloys are Ni-free cobalt chromium tungsten (CoCrW) [27], cobalt chromium (CoCr), and cobalt chromium molybdenum (CoCrMo) [16,26,28]. Research has shown that osseointegration of CoCr is possible via EBM [24]. Porous CoCrMo has ideal stiffness and strength properties in comparison to femoral cortical and cancellous bone for orthoepic implant use [25]. Co-29Cr-6Mo of porous

structures are fit for knee replacements manufactured by EBM and comparable to Ti-6Al-4V for bone stiffness in terms of densities. Co-based alloys are commonly used in total joint replacement, dental implants, removable partial dentures, femoral stems, bone implant applications, load-bearing implants and bearing-surface implants [30]. Industry standards for Cobalt-based alloys include ASTM F3213, which provides guidelines for Co-28Cr-6Mo manufactured via L-PBF, along with ASTM F75 of Co-28Cr-6Mo for the design of surgical implants [194-195].

2.1.3 316L Stainless Steel

Stainless Steel 316L is common in orthopedic implants due to its suitable mechanical properties relative to human bone, corrosion resistance and low material cost. 316L was used for Total Hip Arthroplasty (THA) on the femoral stem and head during the 1970's. After 9-20 years of implantation, it was revealed that corrosion occurred on surface of the stem or head, leading to periprosthetic metallosis and rapid failure. Due to these series of corrosion failures, 316L is now only recommended for temporary use, such as screws, plates and hip nails instead of long-term use [30]. Coatings such as Hydroxyapatite (HAP) [31] and bioactive glass ceramic films [32] can improve corrosion resistance, making 316L biocompatible for long term service. 316L can also corrode *in vivo* in highly stressed oxygen-depleted environments [29]. In terms of AM compatibility, research has shown 316L being processed via SLM, SLS and EBM [16,33]. Mechanical properties such as elastic modulus and compressive yield strength can be matched to cancellous bone [34], and SLS-produced porous structures can match human cortical bone for elastic modulus

and compression strength [35]. Standards for 316L can abide by ASTM F138 for stainless steel bar and wire used in surgical implants [196].

2.1.4 Nickel-titanium (Nitinol)

Nitinol is a biocompatible metal with good mechanical properties for medical implants. What makes nitinol unique is the shape memory effect nitinol possess. There are two reasons why this is beneficial: encouragement of bone fixation; and allowance for minimization of invasive surgery. Shape memory is activated by temperature. Figure 1 is an example of a wire changing from modified form to original via high temperature liquid. Porous nitinol has also been proven to be suited for bone growth due to its biocompatibility. An *in vitro* study showed hMSC cells were able to grow on nitinol [36,39]. Mechanical properties of nitinol can vary depending on the compositions and alloys used. The stress-strain behavior of nitinol can replicate that of human bone. Nitinol shows no cytotic, neurotoxic, genotoxic or allergic activity when compared to 316 SLM stainless steel [38]. Nickel content in nitinol may cause harm to the body with the release of nickel ions, however alloying and surface treatment can reduce this, assuring good biocompatibility [37]. Nitinol has been produced via SLM [39], LENS [13,14,15] and EBM [16]. Current uses for nitinol include vascular stents, vena cava filter, intracranial aneurysm clips, catheter guide wires and orthopedic staples, all of which are currently FDA approved [30]. Research for nitinol is concurrent and applications for orthopedic implants are currently being researched. [30,38,37,39,36].

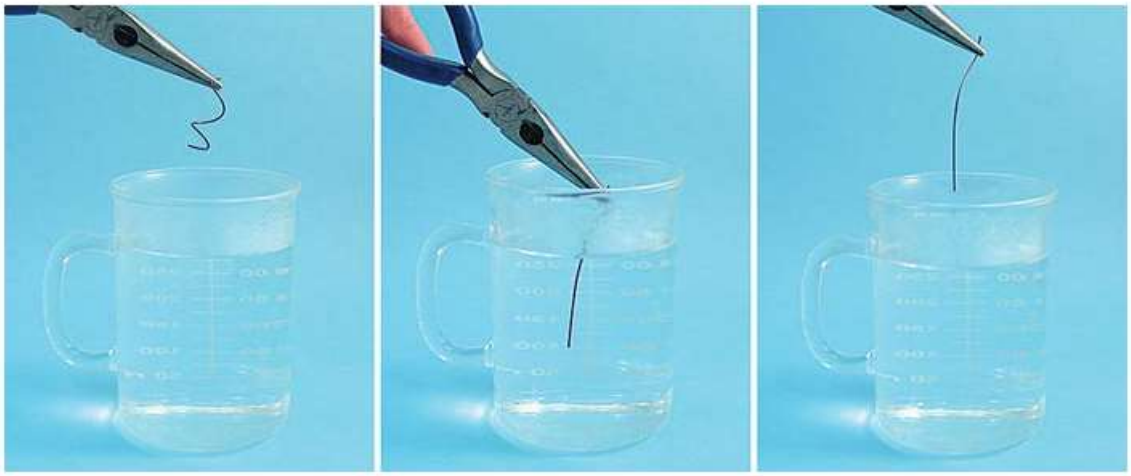

Figure 1. Nitinol shape memory from non-original form to original due to high temperature liquid [40]

2.2 Laser-Powder Bed Fusion Technologies

Laser-Powder Bed Fusion is an additive manufacturing technology that can produce metal and metallic 3D objects. There are two types of LPBF technologies: powder bed systems and powder-fed systems. For powder bed, the following technologies exist: Selective Laser Melting (SLM), Direct Metal Laser Sintered (DMLS), Selective Laser Sintering (SLS) and Electron Beam Melting [EBM]. Powder-fed systems are Laser Metal Deposition (LMD) and Laser Engineer Net Shaping (LENS) [2].

2.2.1 Laser Engineered Net Shaping (LENS)

Developed by Sandia National Laboratories, Laser Engineered Net Shaping produces metal parts using metal powder with an inert gas injected into a molten pool that is created via a focused high-powered laser beam. The substrate (build plate) is fixed, where the laser system is moving, creating the 3D object; as with most L-PBF, LENS operates in an enclosed environment with controlled oxygen content to reduce oxidation. Figure 2

illustrates the LENS process. The density of the parts is over 99%, comparable to SLM. It is possible to modify already existing parts with LENS technology. Machine parameters that affect part quality include scanning speed of laser, laser powder, feed rate of materials and melting point of feedstock [12]. LENS may use biocompatible metals such as Ti-based alloys, Co-based alloys, Nitinol and Tantalum [11]. Various biomedical implant research has been performed using LENS, for example, load bearing implants [13], Ti-6Al-4V coatings for load bearing implants [14], and microstructure/corrosion properties of NiTi alloy for bone implants [15,16].

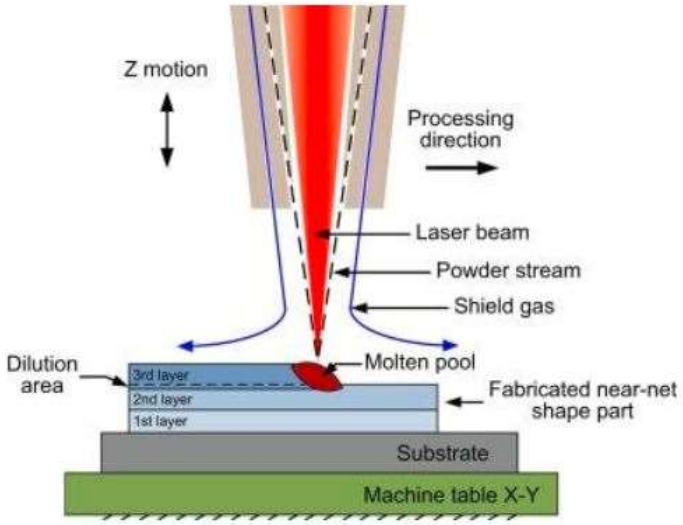

Figure 2. Laser Engineered Net Shaping (LENS) process [12]

2.2.2 Laser Metal Deposition (LMD)

Laser Metal Deposition produces 3D objects via one or multiple nozzles wherein powder and a laser meet, creating a melt pool onto a substrate. Metal powder is injected using a gas stream to the melt pool, and the absorbed metal powder is deposited onto the surface. Figure 3 provides a diagram of the LMD process. LMD can not only produce parts, but

repair surfaces, similar to welding. The laser and powder nozzle move in the Z-axis, whereas the work table can move in the X-axis and Y-axis in conjunction with the nozzle/laser to produce the required geometries. Multiple layers are built in consecutive order to produce a 3D part. The ability to move the work table aids in the process of high dimensional accuracy [41]. Uses for LMD for creation of biomedical implants are limited, in comparison to SLM. The ability to print complex parts is limited, but LMD can produce larger parts than SLM. Research is concurrent on titanium composites and improving process parameters for use of producing biomedical implants [41,42]. LMD is also used for surface modification. Gum metal coating was applied to Ti-6Al-4V to improve surface properties in [43], and ceramic thin films were applied to metallic implants to improve biological behavior for hard tissue restoration in [44].

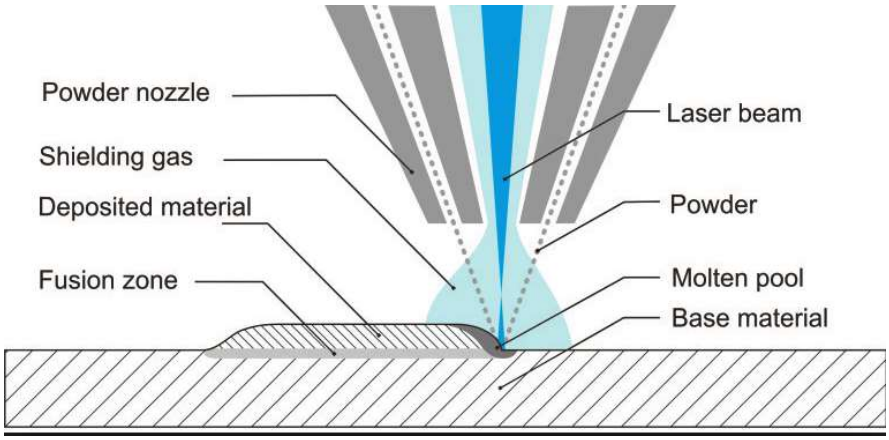

Figure 3. Laser Metal Deposition process [183]

2.2.3 Selective Laser Sintering (SLS)

Selective Laser Sintering begins with a layer of powder on top of a build plate. One or multiple lasers sinter the powder to a specific geometry. The particles at this step will fuse

together but won't completely melt. Built upon the initial layer, more powder is spread via a roller/recoater, and the laser will melt continuous layers to produce an object one cross-section at a time, leading to a 3D object. The powder may consist of metal composite [45,46], thermoplastic polymer [48], or ceramics. Direct selective laser sintering (DSLS) refers to sintering metal powders [16]. SLS is popular for porous applications due to low compaction forces of the sintering process, creating porous structures and ability to produce complex shapes. It is possible to produce metallic porous structures that can match human cancellous and cortical bones mechanical properties for Ti-Mo alloys [45]. In addition to titanium, 316L Stainless Steel can also be made porous to match cancellous bone [46]. Process parameters such as laser power, scan speed, hatch distance, laser energy density, scan pattern, powder quality/size/composition, shielding gas flow and pre/post processing, all affect part quality in terms of surface finish, mechanical properties and porosity [46,47]. Components after printing may go through a post-process heat treatment for better mechanical properties, different post-processing temperatures can affect mechanical properties [50]. Applications exist from dental implant of atrophied posterior mandible [49] to bio-metal bone scaffolds [50].

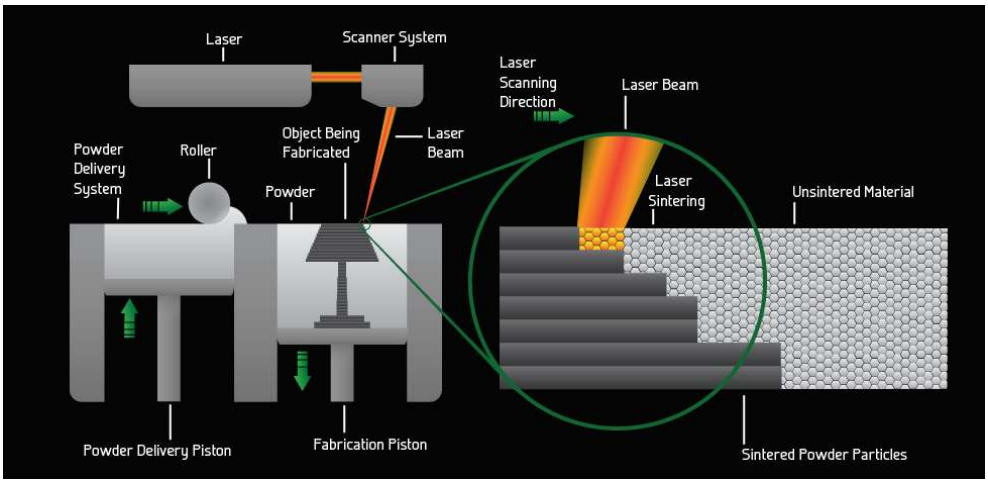

Figure 4. Selective Laser Sintering process [51]

2.2.4 Selective Laser Melting (SLM)

Like SLS, selective laser melting fully melts the powder instead of sintering, creating parts with approximately 99.9% relative density. The process of SLM begins in a controlled and closed chamber, filled with argon or dinitrogen gas, including over pressure conditions. The purpose of this inert chamber is to prevent oxygen contamination during the melting process [78]. SLM is also called Direct Metal Laser Sintering (DMLS). Due to this melting, only pure and alloyed metal powder may be used. Figure 5 provides a diagram of the SLM process. SLM is one of the most, if not the most popular type of L-PBF. This is due to the numerous advances of the technology in terms of speed, lower cost, innovation, and implantation of various alloys to use. Process parameters of SLS are the same for SLM. Various patents from the 1970's and 1980's discusses working fundamentals, but the first true commercial system resulted in the year 2000 [59]. Numerous applications exist for SLM in biomedical implant use including orthopedic implants [19,20,52], dental implants [22,26,28], in vitro research [25,26,54,55.57], and scaffolding [39,56,58].

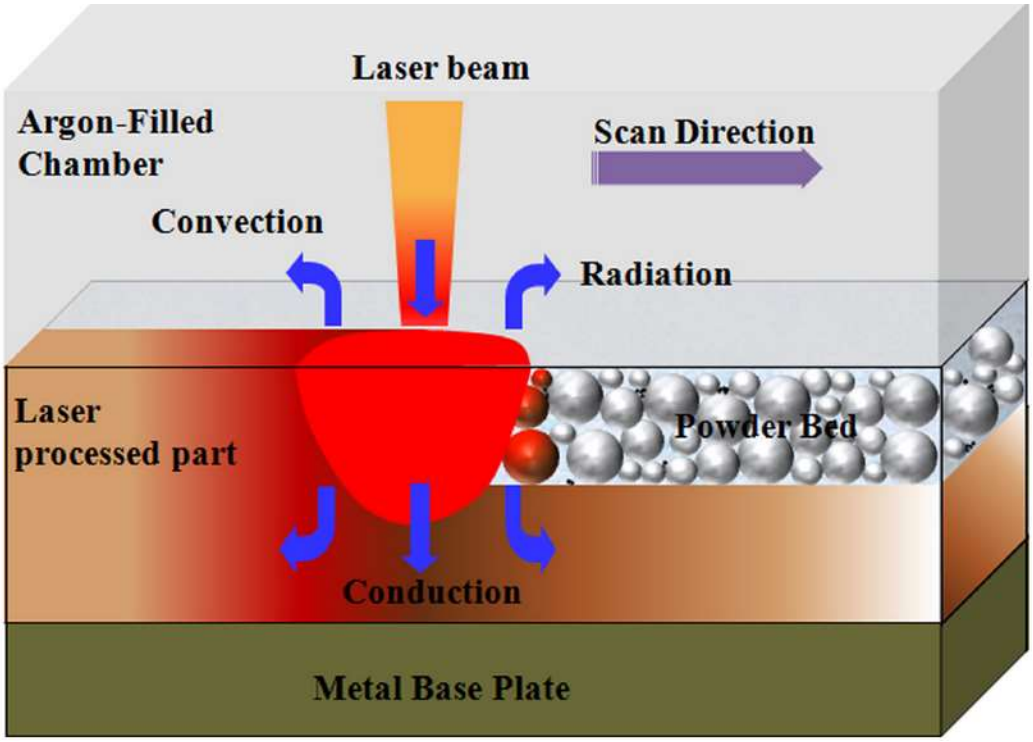

Figure 5. Selective Laser Melting process, closeup view [79]

2.2.5 Electron Beam Melting (EBM)

EBM has a similar process to SLS and SLM; however, instead of a laser beam, electron beam energy is used to melt powder. An electron beam is initiated via a tungsten filament that is superheated in an electron beam gun, creating electrons that can melt powder. To control the beam diameter, a magnetic field is used, following a second magnetic field that directs the electrons to desired location on the printing platform [77]. To control temperature gradient during EBM process, preheating is performed by scanning the beam across the entire layer. After preheating, the cross-section is melted via two stages, contouring and hatching. Contouring melts the perimeter of the part cross section with constant beam power and velocity, this improves surface finish of the part. Hatching is a

back and forth raster pattern, unlike contouring, beam power and velocity are not constant, but vary based on various thermal conditions analyzed by the system [68]. EBM operate in vacuum to reduce energy dissipation before the beam melts the powder [69]. Figure 6 provides an image of the EBM process. Process parameters of EBM are similar to SLM, wherein laser energy is now beam energy, and scanning speed can also be set by two independent parameters: point distance and exposure time [69]. In terms of popularity and use, EBM and SLM are the two most common and popular L-PBF technologies. The differences between these two techniques are discussed in [16]. EBM can produce parts with lower residual stress and increased surface roughness due to the higher power of the electron beam [16]. Most of the previous materials mention in Section 2.1 can be created via EBM, along with Inconel 718 and marginal steel. Applications of EBM for biomedical implants include orthopedic implants [60,63,65,67], in-vitro research [24,62], in vivo research [61], and cranial implant [64].

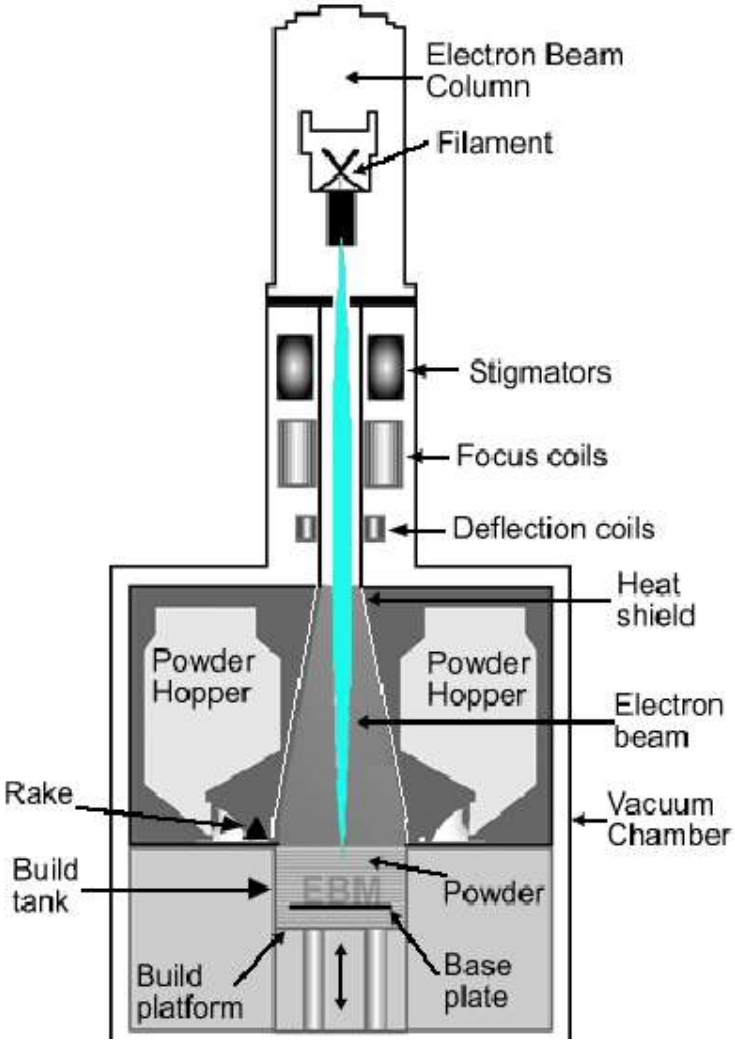

Figure 6. Electron Beam Melting process [80]

2.3 Electron Beam Melting and Selection Laser Melting Comparison

EBM and SLM are the two most popular and promising L-PBF technologies in the current market for biomedical applications. Research is ongoing to improve dimensional accuracy, higher resolution, faster build time, reducing excess material waste, and various economic factors. EBM finished products have an ideal surface finish for orthopedic implants; surface roughness aids in the osseointegration process, which increases bone apposition.

This surface roughness is controlled by various process parameters and can also be harmful to mechanical properties of the part, reducing tensile strength and ductility, and causing premature part failure. A highly rough surface may increase the chance of bacteria growth for areas of low blood flow [70,71,72,73,74,60,76]. SLM has a slower build rate compared to EBM; this is due to the higher power outputs of the electron beam. EBM production rate is 80 $cm^3 \cdot h^{-1}$ compared to SLM 20-40 $cm^3 \cdot h^{-1}$ [16,75,60]. The choice of powder selection for EBM is 45-105µm compared to SLM 20-45µm. EBM's larger range of sizes allows for affordability of various powders, such as titanium [60]. However, EBM parts typically require overnight cooling due to higher temperatures on the powder bed [78]. Both EBM and SLM parts require post-processing, but EBM is more likely to need it when compared to the smoother surfaced SLM parts [77]. Usage of process parameters and utilizing them for materials is considered more difficult for EBM. SLM offers a wide range of material powders, such as Aluminum, Titanium, Iron, Nickel, Cobalt, Copper and their respective alloys, where EBM can produce Ti grade 2, Ti-6Al-4V, Inconel 718, Stainless Steel 316L and CoCrMo. EBM can produce brittle materials, where SLM has high cooling rates, which can cause solidification cracks. [78].

2.4 Hot Isostatic Pressing (HIP)

During the production of parts created via EBM and SLM, the occurrence of defects, in this case porosity, have a significant effect on life-cycle of parts. These pores form from gas trapped in molted metal while the melt pool solidifies. Lack of fusion between two layers forms pores, along with lack of melting during laser scanning and the ability to fully melt all areas [127]. To overcome these characteristic defects, HIP is commonly used to

close internal pores in metal parts, along with reducing surface finish. A part is placed in a high temperature and pressurized environment with an inert gas. Pores close due to high diffusion rates from high temperatures with applied pressure and reduced yield stress. Internal pores as large as 20 μm and below can be closed with HIP. Internal pores are initiation sites for cracking, thus reducing porosity results in better high-cycle fatigue. Research has shown that surface connected porosity will be unchanged from HIP, hence HIP is ideal for removal of gas pores, internal porosity, and lack of fusion defects [126]. Parts processed by HIP have improved ductility, but reduced strength when compared to non-HIP parts. These effects on mechanical properties must be considered when HIP is applied to implant parts. [127].

CHAPTER 3

MECHANICAL PROPERTIES AND MATERIALS TESTING

AM produced metallic implants are ideal for replacement of bone in biomedical implants for numerous reasons, such as mechanical properties, biocompatibility, manufacturing means and more. As previously mentioned in chapter 1, various metals and alloys can be placed into the human body without ill-advised side effects, such as corrosion, release of harmful ions and bone resorption (stress shielding). Biocompatible materials can also promote osteointegration, which aid in bone fixation and greater mechanical performance, this is further discussed in chapter 4. These metallic implants can provide identical mechanical properties in place for bone, as this chapter will analyze the mechanical properties of bone and Ti-6Al-4V.

3.1 Bone Properties

To insure proper performance of an orthopedic implant, the mechanical properties and viscoelasticity of the implant must match the bone it replaces and the bones that it interacts with the implant. Bone is a hierarchal structure, wherein each structure are unique mechanical, chemical and biological functions. This structure can be broken into levels, such as macroscale, microscale, sub-microscale, nanoscale and sub-nanoscale, as seen in Fig. 7.

3.1.1 Macroscale

The macroscale is composed of two type of bone, the cortical (compact) and cancellous (trabecular) bone. Bones in the human body will have a combination of these two bone types, such as the femur with a cortical shell and a cancellous interior [91]. Cortical porosity is 3-5%, almost solid; cancellous bone porosity is 50-90%. [87,60]. Cortical bone mechanical properties are influenced by three properties, porosity, mineralization level and organization of solid matrix. Cortical bone of femur, tibia, and humerus will vary for mechanical properties, but density will remain the same. Elastic moduli in a longitudinal direction did not have a variation between different cortical bone types. However, there is a greater modulus variability along length of whole bone than around its circumference, which is an anisotropic property. Cancellous bone contains no difference in mechanical properties of proximal tibia, humerus and lumbar spine. The strength and stiffness of these bone were lower than patella, distal and proximal femur. Mechanical properties of the cancellous vary largely around the periphery, along the length and showcasing inter-subject differences [91].

3.1.2 Microstructure

Microstructure of bone is made up of mineralized collage fibers that form into lamella. Sheets of lamella of mineralized collagen fibers are wrapped in concentric layers around a central canal, forming the osten/Haversian. The osten is a cylinder parallel to the long axis of bone. Cortical bone are mineralized collagen fibers, this is called woven bone. In some cases, lamella and woven bone tissue will form a plywood-type stack of thick layers around circumference of bone, called lamellar bone. Lastly, the cancellous is made of the

interconnecting framework of trabeculae, this framework is composed of various cellular structures such as plate-plate, rod-rod, and rod-plate [91].

3.1.3 Sub-microstructure, Nanostructure and Sub-nanostructure

The bone lamella arrangement and orientation that make up the sub-microstructure is not well known. Although ideas of orientation and structure is discussed [60]. The nanostructure is made of collagen fibers that are surrounded and ingested with mineral. The sub-nanostructure consists of three materials, collagens, non-collagenous and crystals [91].

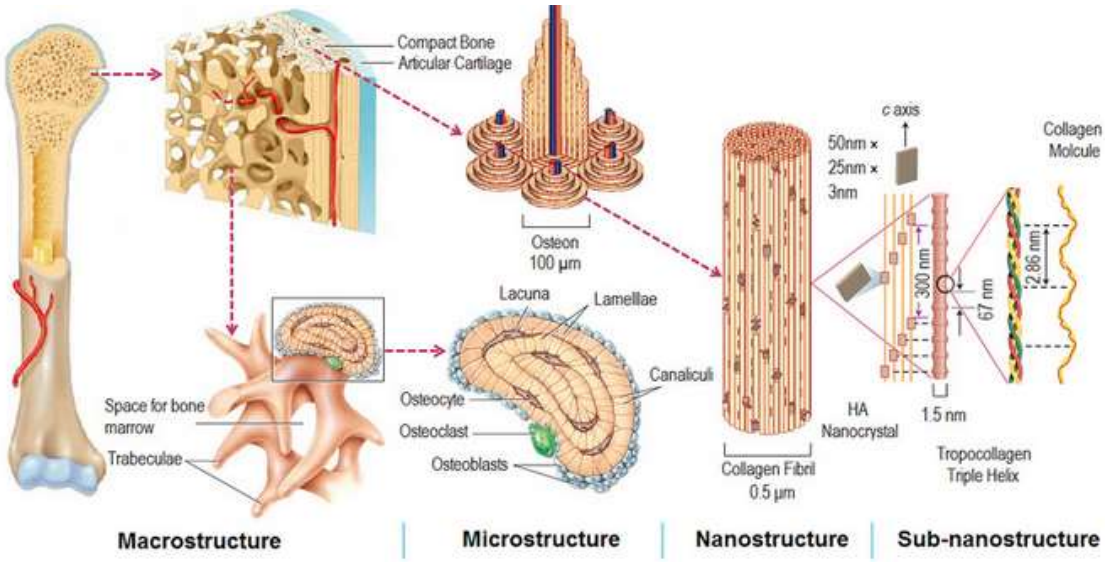

Figure 7. Hierarchal structure of bone [87,60]

3.1.4 Bone Mechanical Properties

Based upon a large data set of bone mechanical properties [60], specifics of mechanical properties will be discussed. Ultimate strength and elastic modulus differ for cortical and cancellous bone, as cortical is less porous than cancellous bone. Cortical bone of different

types, such as femur and tibial have different mechanical properties. It is in this difference that it is recommend using different grades of Ti-6Al-4V to meet various properties of bone. It is also observed that most fractural failures of cortical bone occur from tensile stress and strain of torsional and bending type, the failure site of the bone is where tension occurs, because tensile strength is significantly lower than compressive strength. Ultimate tensile and compressive strains of human bone decrease as age increases, differences between genders exist, but are not distinct. Cortical fibular and femoral bone tensile strength decrease with an increase of age, but tibia does not change for age in terms of tensile, but ultimate strain is affected. Cancellous tibia ultimate compressive strength and stain will decrease with increasing age. Elastic modulus does not change with age. Increasing bone density, the strain, elastic modulus and ultimate strength will rise. Lumbar spines are anisotropic, densities are similar for vertical and horizontal directions, but the elastic modulus and ultimate compressive strength for vertical direction are higher than horizontal direction; ultimate compressive strain is the opposite. The mechanical properties of bone will vary with age, bone quality, health, anatomical site and gender [87-89,60,91]. Cancellous bone is anisotropic and non-homogenous, where cortical bone is linearly elastic, transversely isotropic and relatively homogeneous. Cortical bone is two decades stiffer than cancellous bone, meaning cortical can sustain more stress but less strain before failure. For example, cancellous bone can withhold 75% strain before failure in vivo, where cortical bone will fracture at strain of 2%. The cancellous bone can store more energy compared to compact bone due the pores filled with fluids. The bone of a child can absorb 45% more energy before failure compared to adults, but children bones are weaker with children's stiffness being 68% more than adult bones [103].

Bone is viscoelastic, meaning the behavior is viscous, in terms of time and history dependent, and elastic. Characteristics of viscoelasticity are stress-relaxation, creep, strain-rate sensitivity and hysteresis. Stress-relaxation is when tissue is stretched at a fixed length, as time progresses the stress in the tissue will continually decline. Creep is when constant force/stress is applied on a tissue - constant tensile force causes tissue to elongate through time. Strain-rate sensitivity will vary with age of tissue. Lastly, loading and unloading curves from force-deformation test of bone don't always follow the same path. This difference in calculated area under the loading and unloading curves is termed hysteresis – the energy lost due to internal friction of material [103].

Table 1: Tensile Properties of Cortical Bone [60,92] Note: [a] based-on Ref [93]

Bone	Age	TYS (MPa)	UTS (MPa)	Elastic Modulus	Ultimate strain (%)	Density ($g \cdot cm^{-3}$)	Source of bone (moist)	Cross head speed (mm/min)	Ref.
Fibula	33	N/A	100	19.2	2.1	1.91	Embalmed body	1.1	[60,93]
	59	N/A	80	15.2	1.19	1.73	Embalmed body	1.1	[60,93]
Humerus	15-89	N/A	149	15.6	1.2	1.77	N/A	0.5	[60,94,95]
	20-39	N/A	125	17.5	1.43	N/A	Moist	N/A	[103]
	15-89 female	N/A	151	16.1	1.9	1.72	N/A	0.5	[60,94,95]
Tibia	41.5 male	N/A	106	18.9	1.76	1.96	Embalmed body	1.1	[60,93]
	71 male	N/A	84	16.2	1.56	1.83	Embalmed body	1.1	[60,93]
	20-29	126	161	18.9	4	1.83[a]	Frozen	N/A	[60,96]
	30-39	129	154	27	3.9	1.83[a]	Frozen	N/A	[60,96]
	40-49	140	170	28.8	2.9	1.83[a]	Frozen	N/A	[60,96]
	50-59	133	164	23.1	3.1	1.83[a]	Frozen	N/A	[60,96]
	60-69	124	147	19.9	2.7	1.83[a]	Frozen	N/A	[60,96]
	70-79	120	145	19.9	2.7	1.83[a]	Frozen	N/A	[60,96]
	80-89	131	156	29.2	2.3	1.83[a]	Frozen	N/A	[60,96]
	20-39	N/A	174	18.4	1.5	N/A	Moist	N/A	[103]
Femur	41.5 male	N/A	102	14.9	1.32	1.91	Embalmed body	1.1	[60,93]
	71 male	N/A	68	13.6	1.07	1.85	Embalmed body	1.1	[60,93]
	15-89 male	N/A	141	15.2	2	1.9	N/A	0.5	[60,94,95]
	15-89 female	N/A	134	15	1.8	1.8	N/A	0.5	[60,94,95]
	20-29	120	140	17	3.4	1.85[a]	Frozen	N/A	[60,96]
	30-39	120	136	17.6	3.2	1.85[a]	Frozen	N/A	[60,96]
	40-49	121	139	17.7	3	1.85[a]	Frozen	N/A	[60,96]
	50-59	111	131	16.6	2.8	1.85[a]	Frozen	N/A	[60,96]
	60-69	112	129	17.1	2.5	1.85[a]	Frozen	N/A	[60,96]
	70-79	111	129	16.3	2.5	1.85[a]	Frozen	N/A	[60,96]
	80-89	104	120	15.6	2.4	1.85[a]	Frozen	N/A	[60,96]
	20-39	N/A	124	17.6	1.41	N/A	Moist	N/A	[103]
Radius	20-39	N/A	152	18.9	1.5	N/A	Moist	N/A	[103]

Table 2: Compressive strength and elastic modulus of human cortical bone. [60,93] Note: [a] based-on Ref [93]

Bone	Age	UCS (MPa)	Elastic modulus (GPa)	Density ($g \cdot cm^{-3}$)	Source of bone (moist)	Ref
Tibia	20-29	N/A	N/A	1.83[a]	Frozen	[60.93]
	30-39	213	35.3	1.83[a]	Frozen	[60.93]
	40-49	204	30.6	1.83[a]	Frozen	[60.93]
	50-59	192	24.5	1.83[a]	Frozen	[60.93]
	60-69	183	25.1	1.83[a]	Frozen	[60.93]
	70-79	183	26.7	1.83[a]	Frozen	[60.93]
	80-89	197	25.9	1.83[a]	Frozen	[60.93]
Femur	20-29	209	18.1	1.85[a]	Frozen	[60.93]
	30-39	209	18.6	1.85[a]	Frozen	[60.93]
	40-49	200	18.7	1.85[a]	Frozen	[60.93]
	50-59	192	18.2	1.85[a]	Frozen	[60.93]
	60-69	179	15.9	1.85[a]	Frozen	[60.93]
	70-79	190	18	1.85[a]	Frozen	[60.93]
	80-89	180	15.4	1.85[a]	Frozen	[60.93]
	20-39	107	N/A	N/A	Moist	[103]

Table 3: Compressive properties of human cancellous bone [60,92]

Bone	Age	CYS (MPa)	UCS (MPa)	Elastic modulus (GPa)	Ultimate Strain (%)	Density ($g \cdot cm^{-3}$)	Source of bone	Test condition of bone	Cross head speed (mm/min)	Ref
Lumbar Vertebra	14-89 male	N/A	4.6	0.06	6.7	0.2	N/A	Dried	0.05	[60,97]
	14-89 male	N/A	2.7	0.04	6.1	0.2	N/A	Dried	0.05	[60,97]
Tibial head	14-89 male	N/A	3.9	0.03	8.3	0.22	N/A	Dried	0.05	[60,97]
	14-89 male	N/A	2.2	0.02	6.9	0.22	N/A	Dried	0.05	[60,97]
Tibia	16-39	N/A	10.6	0.65	2.48	N/A	Frozen	Moist	0.02	[60,98]
	40-59	N/A	9.86	0.83	2.12	N/A	Frozen	Moist	0.02	[60,98]
	60-83	N/A	7.27	0.61	2.05	N/A	Frozen	Moist	0.02	[60,98]
roximal tibia	59-82	N/A	5.33	0.45	N/A	0.29	Frozen	Moist	N/A	[60,99]
Femur	58-83	N/A	7.26	0.39	N/A	0.5	Frozen	Moist	N/A	60,100]
umbar spine	15-87 Vertical)	N/A	2.45	0.07	7.4	0.25	Frozen	Moist	N/A	60,101]
	15-87 orizontal)	N/A	0.88	0.02	8.5	0.24	Frozen	Moist	N/A	60,101]
	71-84	1.37	1.55	0.02	7.4	0.19	Frozen	Moist	5	60,102]

3.2 Ti-6Al-4V Mechanical Properties

Ti-6Al-4V is popular due to its high strength to weight ratio, biocompatibility, corrosion resistance and good fatigue resistance properties, making this metal alloy ideal for

biomedical implants. Table 4 features tensile properties from various research of solid Ti-6Al-4V manufactured via SLM, EBM, wrought and casting. The various manufactured specimens allow a wide overview of the influence of manufacturing on the metal's properties. Densities for EBM and SLM will be over 99% due to the nature of the manufacturing process, unless there was an error during production and a defect occurred, however such defects would have a considerable effect on yield strength results. Table 5 lists compressive properties of Ti-6Al-4V for SLM and EBM, compressive properties are limited for solid materials.

Table 4: Tensile Properties of Ti-6Al-4V

Density (%)	UTS (MPa)	TYS (MPa)	Elastic modulus (GPa)	Elongation (%)	Manufactured	Ref
N/A	1140±10	1040±10	N/A	8.2±0.3	SLM	[105,106]
99.7±0.1	1095±10	990±5	110±5	8.1±0.3	SLM	[105,106]
N/A	1248	1043	112	8.5	SLM	[105,107]
N/A	1269±9	1195±19	N/A	5±0.5	SLM	[105,108]
N/A	1407	1333	N/A	4.54	SLM	[105,109]
99.5	1321±6	1166±6	112	2±0.7	SLM	[105,110]
N/A	Min 860	Min 758	N/A	Min 8	SLM	[105,111]
99.9	1220±60	1140±60	N/A	8-10	SLM	[112]
99.8	1250	1125	94	6	SLM	[113,114]
N/A	1200-1150	1150-1100	N/A	16-25	EBM	[113,115]
N/A	1002	902	113	6.9	EBM	[120]
N/A	1220-1170	1290-1230	N/A	12-14	Wrought	[113,115]
N/A	1173	999	113	6	Casting	[113,116]
N/A	934	862	N/A	7	Casting	[113,117]

Table 5: Compressive Properties of Ti-6Al-4V

CYS (MPa)	UCS (MPa)	Strain (%)	Manufactured	Ref
1328.4	2265.3	35.4	SLM	[118]
1300-1099	1763-1620	42-23	SLM	[119]
950	1826	N/A	EBM	[120]

3.3 Materials Testing of Bone

Bone testing is applied via various techniques such as, tensile, compressive, bending and torsion testing. Popular companies used for mechanical testing are Instron, MTS and McMesin [103]. Storage and preparation of bone can affect mechanical testing outcome. Dried bone has an increased Young's moduli and strength – toughness will also decrease. Thusly, it is ideal for bone to be hydrated for testing purposes. Bone mechanical properties are also ideal at 37°C but testing at room temperature 27°C does not cause a large error, however fatigue tests at room temperature will endure twice as many loading cycles before failure compared to 37°C [121].

Bone is viscoelastic in its natural state, when dried the viscous nature is no longer active and thusly behaves like a spring. When the bone is moist, strain rate will vary, a certain strain rate range must be applied in order to properly measure stiffness and strength, the strain rate of 0.01 to 0.08/s is what occurs *in vivo* [91]. Cortical bone has an ultimate strain rate of 1.2% moist and 0.4% dry [103]. Tensile testing is typically performed using universal joints, some bone can be machined to create test specimens for the cortical and cancellous bone. A negative about tensile testing is that specimens must be large and machined carefully. Compression testing is also possible, but complications exist, such as

the need for parallel loading to be applied to a bone. For example, where the specimen contacts the plate, some trabeculae may be unsupported from machining the face flat, leading to less than ideal results. If the loading platens are misaligned, end results will be incorrect. There are advantages for compression testing over tensile, such as the ability to test with smaller specimen, fabrication is simpler and vertebral specimens are also preferred for compression testing [121]. Human bones such as femur, tibia, humerus, mandible, lumbar vertebrae and patella for orthotropic elastic modulus, shear moduli, Poisson's ratios and densities are measured via ultrasonic techniques. [91]

3.4 Ti-6Al-4V Testing and Standards

Mechanical testing for Ti-6Al-4V such as compression and tensile are typically guided by ASTM and ISO standards. ISO 6892 are for metallic tensile testing at room temperature [107]. ASTM standards E8 are for tensile testing of metallic materials. ASTM F2924 involves additive manufacturing of Ti-6Al-4V for powder bed fusions, this standard defines terminology, chemical composition, microstructure, mechanical properties and various processes to insure high quality parts for purchasers and producers of AM Ti-6Al-4V. ASTM F1108 is standard specifications for Ti-6Al-4V alloy castings for surgical implants. ASTM F136 is standard specification for wrought Ti-6Al-4V ELI (Extra Low Interstitial) alloy for surgical implant applications.

3.5 Stress Shielding

Using a femur bone as an example, a femur in a natural state carries the loads of the hip joints and muscle itself. When an implant is added, such as an intramedullary stem, the

femur now shares the load with the implant. Before, the load was carried by one structure, now the load is carried by two structures, implant and bone. The bone is thusly shielded from stress, hence the term the stress shielding [122]. According to Wolff's law, bone develops a structure as a reaction to forces acting upon it. When bone experiences high stress/load, the reaction will be to increase bone mass in those areas and decrease bone mass in lower load/stressed areas. Bone resorption is known as the decreasing of bone mass, which leads to loosening of implant, resulting in implant failure [90]. **It's for these reasons that matching the mechanical properties of the implant to the bone it neighbors is vital for long term implant life and function.**

3.6 Bone and Ti-6Al-4V Mechanical Properties Comparison

Comparing Table 1 tensile properties of various bone to Table 4 tensile properties of Ti-6Al-4V, it's apparent that a large difference exists for TYS, UTS and the elastic modulus. The differences are almost tenfold, regardless of manufacturing method. For example, the femur for 50-59 age has a UTS 131 MPa and Elastic modulus 16.6 GPa, compared to SLM Ti-6Al-4V UTS 1095 MPa and Elastic modulus 110 GPa. The differences remain similar for compressive data for cortical or cancellous bone compared to Ti-6Al-4V. Table 2 compressive properties of cortical bone, tibia for age 40-49 UCS 204 MPa, compared to SLM Ti-6Al-4V UCS 1620 MPa. With these high differences in mechanical properties, stress shielding occur, and the implant would fail due to implant loosening. However, creating cellular porous structures or lattice structures with Ti-6Al-4V reduces the differences in mechanical properties, allowing for Ti-6Al-4V to match bone for implants.

3.7 Loads on Various Orthopedic Implants and Bones

This section reviews various loads present on orthopedic implants and bones. The purpose of this review is to clearly document forces placed onto implants/bones as the data is vital to creation of functional and long-term implants. In order to analyze the loads placed on various implants and bones, one must determine the body weight (BW) of an individual, as this criterion will vary with individuals. Determining which loads are appropriate is another aspect to be considered. Activities of daily living (ADL) such as walking, climbing stairs, sitting and lifting are activities that humans perform with great frequency. Analyzing the loads from these activities will give a good baseline of loads orthopedic implants replacing these bones would experience.

3.7.1 Standardized Forces and Moments in Knee Implants

This study seeks to standardize forces and moments based on *in vivo* data. These *in vivo* data is measured via an instrumented knee implant that measures tibio-femoral contact forces and moments – ISO 14243 for testing wear in knee implants is used to define loads. ADL analyzed are walking, ascending stairs, descending stairs, one-legged (OL) stance, stand up, sitting down, knee bend and jogging. 8 subjects were used for the study, average and high BW were defined from data set of Americana and German individuals of age 60 and 69, average BW was 74.7 kg, 2.3% of population has a BW above 101.5 kg, due to this the average BW of 75kg and high BW of 100 kg is used. Table 6 is the extreme forces (N) and moments (Nm) for the BW of 100. For the coordinate system in Table 6, the system

is related to a right-side implant, where the origin is in the middle of tibial plateau at the height of the lowest part of the polyethylene insert. F_x and F_y are the lateral and anterior directions, $-F_z$ is the axial force component in the direction of the implant shaft. F_{res} and M_{res} are from resultant forces respective components. D is the respective extrema from Figures 2-5 of the study [134].

Table 6: Forces (N) and moments (Nm) of EXTREME100 of knee implants [134]

Component	D	Walking	Ascending Stairs	Descending Stairs	OL Stance	Stand up	Sitting down	Knee Bend	Jogging
F_{res} [N]	1	3110	4209	4787	3676	3870	4036	3608	5551
	2	3581	4572	4348	N/A	N/A	N/A	N/A	N/A
F_x [N]	1	-294	307	-416	222	257	301	318	-423
	2	292	-283	308	N/A	N/A	N/A	N/A	697
	3	-209	N/A	N/A	N/A	N/A	N/A	N/A	N/A
F_y [N]	1	-605	220	-565	-557	-266	392	324	-1148
	2	221	-679	368	N/A	N/A	N/A	N/A	N/A
	3	N/A	-438	N/A	N/A	N/A	N/A	N/A	N/A
$-F_z$ [N]	1	3100	4169	4776	3667	3867	4033	3605	5396
	2	3571	4552	4347	N/A	N/A	N/A	N/A	N/A
M_x [Nm]	1	25.9	30.5	59.1	38.7	21.4	28.6	46.1	39.8
	2	32.2	36	N/A	N/A	N/A	N/A	N/A	N/A
M_y [Nm]	1	-50.3	-48.8	-68.8	-57.3	25.1	22.8	23.3	-57.1
	2	-53.2	-55.1	N/A	N/A	N/A	N/A	N/A	N/A
	3	27.3	37.2	N/A	N/A	N/A	N/A	N/A	N/A
M_z [Nm]	1	12	10.5	-18.5	-13.3	-11.4	-10.8	-13.9	-13.7
	2	-18.9	-13.9	N/A	N/A	N/A	N/A	N/A	N/A

3.7.2 Standardized Loads Acting in Hip Implants

Following the same goals as the previous study [134] and featuring some of the same authors, the goal is to standardize loads in hip implants. This study confirms to ISO 7206-4 for endurance tests of the stem and ISO7026-6 for endurance testing of the neck. *In vivo* measurements were performed on ten subjects that all suffered from coxarthrosis. A titanium implant was modified to measure the forces and moments. ADL analyzed are cycling, sit down, stand up, knee bend, walking, stance, stairs up, stairs down and jogging. Origin of the coordain system is in the center of the femoral head, Z axis is upwards and defined by the line connecting the neck axis and the intercondylar notch. X axis is lateral and parallel to the proximal contour of the condyles, Y axis points to the anterior direction. All measured loads are linearly adjusted from the individual's weight to average BW of 75kg. Table 7 is the AVER75 and HIGH100 peak forces and moments of hip implants. AVER75 are six load components that are averaged loads with a BW of 75kg. F_{res} and M_{res} are vector sums of their components (X, Y, Z, moments/loads), marking them as the resultant forces. HIGH100 is the highest peak force relative to all others, with a body weight of 100kg.

Table 7: Forces and moments of hip implants.
(Minima/Maxima forces or moments for X, Y, and Z axis)

Load type	Cycling	Sit Down	Stand up	Knee Bend	Walking	Stance	Stairs up	Stairs down	Jogging
Peak F_{res} for AVER75 Average [N]	731	1360	1600	1699	1925	2077	2232	2300	3065
Peak F_{res} for HIGH100 Average [N]	1256	2935	3839	3145	2880	3340	3606	3875	4839
M_{res} at instant peak of F_{res} for HIGH100 Average [NM]	1.11	1.92	2.51	2.49	0.93	1.03	1.93	0.66	0.8
Peak value of M_{res} for HIGH100 Average [NM]	1.15	2.09	2.77	2.57	1.76	1.72	2	2.73	1.6
F_x [N]	323/420	442/1002	472/1578	428/1202	265/837	347/1164	379/1164	329/1085	311/1241
F_y [N]	-357/-58	-541/-88	-612/70	-455/-52	-536/24	-1067/-68	-1067/-68	-855/-78	-1222/-21
$-F_z$ [N]	392/1131	728/2709	753/3480	1069/2882	235/2709	644/3198	558/3876	405/3662	229/4519
M_x [NM]	-0.6/1.11	-2.03/1.57	-1.11/2.61	-1.97/2.39	-1.28/1.47	-1.33/1.41	-1.21/1.82	-2.06/1.19	-1.44/0.97
M_y [NM]	-0.22/0.19	0/0.77	-0.7/0.78	0.31/0.93	-0.37/1.21	-0.71/1.71	-0.51/1.24	-0.88/1.5	-0.49/1.07
M_z [NM]	-0.25/0.25	-0.57/0.34	-0.22/0.7	-0.93/0.43	-0.5/0.63	-0.55/0.93	-0.44/0.44	-1.04/0.3	-0.72/0.13

CHAPTER 4

LATTICE STRUCTURES

A lattice structure is an 3D open-cellular structure of repeating unit cells. Unit cells are made up of struts connected to nodes. The lattice is highly versatile in part to high stiffness-weight ratio, negative Poisson ratio, low thermal expansion coefficient, and high heat dissipation; these properties are valuable to such industries as aeronautics, automotive and medical [84]. The properties reviewed thus far are the ability to match various bone mechanical properties to prevent stress shielding and the ability to promote osseointegration. Due to the open cell design, lattices are highly porous, this porosity is 40-90%, depending on numerous parameters. Before discussing parameters of the lattice structure, these parameters must be defined. A unit cell is a 3D object constrained by X, Y and Z-plane dimensions - the lattice is composed of multiple unit cells, as seen in Figure 8.

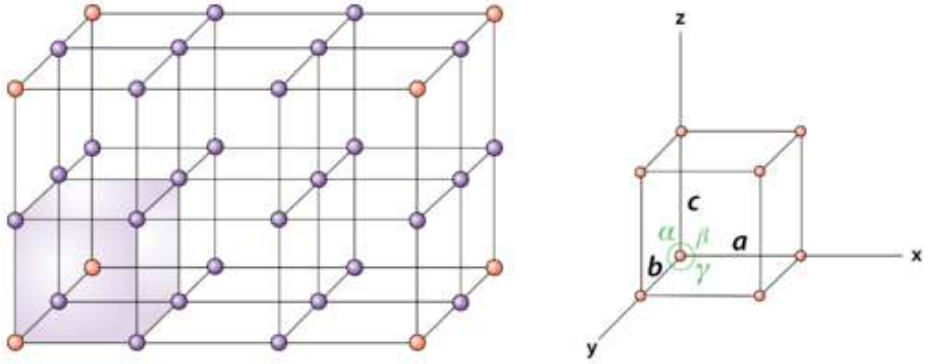

Figure 8. Lattice (left) is composed of the unit cell (right) [81]

Struts are rods forming the framework of the lattice, connected to various nodes. Nodes are connecting points for the struts, branching off to various struts. The unit cell in Figure 7 has four nodes and twelve struts, the number of struts and nodes per unit cell varies depending on the unit cell structure, such as diamond, gyroid or honeycomb. An important parameter of the lattice that will affect osteointegration and is a key point of this work is pore size. Pore size is initially measured in two dimensions but is a three-dimensional factor that varies with unit cell type. Figure 9 is an example of how pore size will be classified as the largest sphere that fits in the 3D structure pores. Some lattice structures may have rounded profile struts and nodes that are oddly shaped, such as a gyroid or Schwarz P.

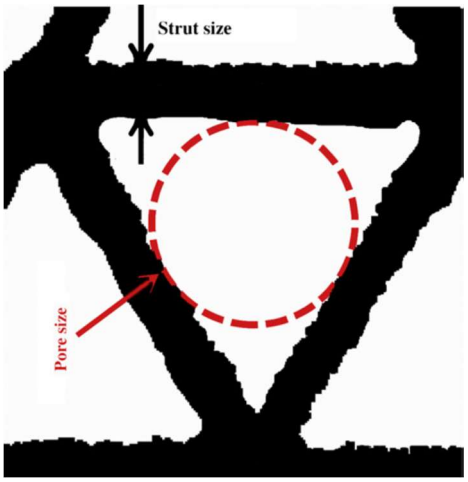

Figure 9. Pore and strut size dimensions [55]

4.1 Parameters Affecting Lattice Mechanical Properties

Various parameters affect the lattice structures mechanical properties: weight, material, relative density, microstructure, defects, structure complexity and manufacturability. This reviews literature relating to parameters affecting mechanical properties of the lattice. A lattice structure for biomedical implants should have good strength in terms of tensile,

compressive and fatigue, along with elastic modulus and viscoelasticity similar to the human bone it replaces and neighboring sections of bone that may be impacted from the inclusion of an implant.

4.1.1 Compression on Lattice Structures

The unit cell size can affect various mechanical properties, the Young's moduli and yield strength of a gyroid will decrease with the increase of unit cell size, due to strut density decreasing with increasing unit cell size [82]. Yield strength and Young's moduli will increase with strut size, which is in relation to volume fraction of the lattice. In the case of this research, a gyroid strut diameter is not constant as a straight beam strut would be in a cubic type. [83] In term of compressive stiffness and ultimate compression strength, both will decrease with an increase of porosity [52] for cubic lattice starting with porosities of 49% to 70%. For the same research, it was also observed that for the same porosity values, compressive stiffness and compressive strength will decreases with smaller strut sizes and increase with number of pores, indicating that strength depends on strut size instead of porosity [63]. EBM lattice compression testing results is reviewed. This research is based on various conditions such as different lattice types, various unit cell and strut sizes [60]. Most of the stress-strain curves observed in the report indicate three common stages. Stage 1: linear elasticity, in relation to corresponding unit cell strut bending or stretching. Stage 2: stress plateau, the progressive unit cell collage via plastic yield, elastic buckling or brittle crushing, all these factors depend on unit cell type and other parameters. Stage 3: densification, a sharp rise in stress occurs here, opposite sides of the lattice will become into contact, behavior is like a solid. The stages are demonstrated on Fig. 9. The

compressive strain at first facture is the most important factor in determining strain, as ultimate compression strain of Ti-6Al-4V lattice can be up to 93%. In accordance to the research gathered, lattice behavior can be divided into bending and stretch dominated behavior, where stretch domination means during compression, struts carrying tension will fail first most. For bending dominated lattices, struts will deform under bending or buckling (dependent on unit cell type). Observing eleven different lattice types, it was found that ultimate compression strength, compression yield strength and modulus values for Ti-6Al-4V produced by EBM increase with an increasing density.

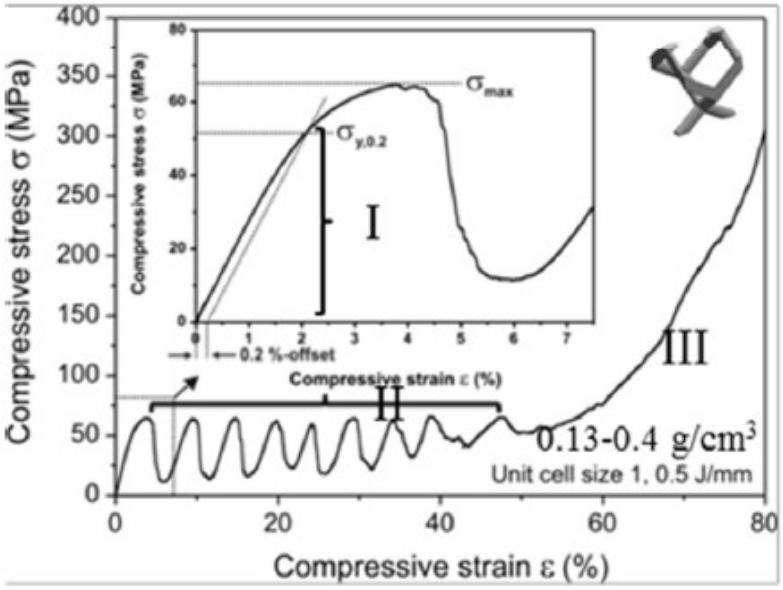

Figure 10. Stages of compression for diamond lattice [60]

4.1.2 Fatigue Properties of Lattice

Cracks from fatigue can cause catastrophic failure of a part. Using previous research of a large data set of EBM lattices, fatigue properties were examined [60]. Three stages were observed for stress vs cycle figures. Stage 1 is where the strain will begin to increase within

less than ten cycles. Stage 2 beings a plateau region where strain remains constant over a wide cycle range, called the “incubation” region. Stage 3 has a sharp rise, lending to complete part and strut failure. Figure 10 demonstrates the stages of fatigue. Fatigue is related to cycling ratcheting of the struts, in relation to the incubation region, and fatigue crack initiation throughout the struts, cyclic ratcheting is more vital in determining fatigue life of lattice [86]. Cyclic ratcheting is the phenomena of progressive application of strain in a lattice from cyclic strut bending, this phenomenon is unique to all unit cell types and will vary. It can also be observed that increasing the amount of stress on a lattice and decreasing the relative density will accelerate failure [86,60]. Elastic modulus is directly related to the type of lattice, a bending-dominated lattice or stretch dominated lattice, the latter of the two having the lower elastic modulus. Typically, low modulus Ti-6Al-4V shows poor fatigue strength in part to high porosity. It has been observed that fatigue striations appear on rough surfaces of struts, also formation of cracks near partially fused or attached Ti-6Al-4V powder on strut surfaces, along with internal pores of struts [86,60].

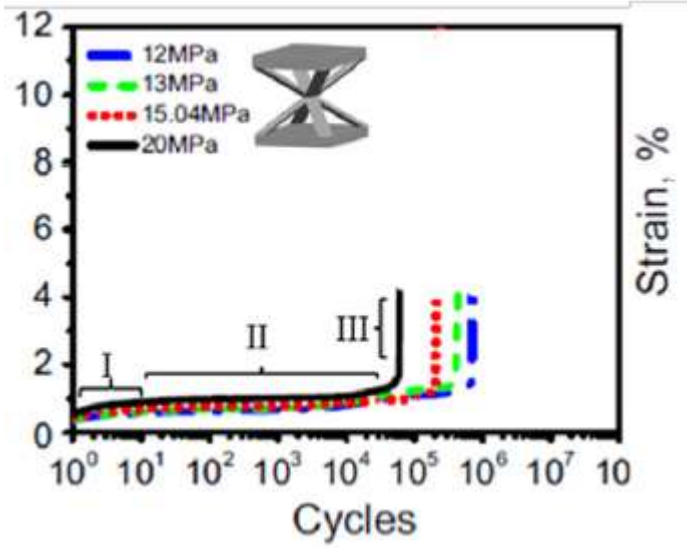

Figure 11. Stages of fatigue for G7 lattice [60]

4.2 Matching Lattice to Bone Properties

Using the large EBM data set and selected publications, information on lattices conforming to bone mechanical properties are discussed. Ultimate compression strength of EBM Ti-6Al-4V lattices are equal or higher than human cancellous bone, with the highest value of 196 ± 7.1 MPa (Cubic lattice, 64% porous). The cubic lattice can be used for human cortical tibia and femur of 50 years, 10 MPa lower than those of young than 40 years. Cubic lattice of porosity 50.75% is 1632.02 ± 11.98 MPa, along with a hatched XY of porosity 59.59% at 148.40 ± 3.50 MPa for ultimate compression strength. EBM cubic and diamond lattice have high compressive yield strength values, possible use for cortical tibia and femur. Modulus of EBM Ti-6Al-4V matches cancellous bone, but lower than cortical bone. Limited fatigue data showcases EBM cubic lattices (porosity 63%) has higher fatigue strengths (105 MPa at 10^6 cycles) compared to human cortical femur (60 MPa at 10^6 cycles). The cortical tibia has a higher fatigue strength of 160 MPa at 10^6 cycles, which the large EBM dataset does not have any lattices that can match the high fatigue strength – reducing porosity is believed to improve fatigue strength, but at the cost of higher density. Cubic EBM lattices can endure strain up to 2% at 10^6 cycles, which aligns with tensile strain of cortical fibula and humerus bone. No data is present for compressive strain of cortical bone, but tensile strain is 1-4%. Analyzing the UCS, CYS, modulus, strain and fatigue strength, for the data set of EBM lattices, cubic is the ideal replacement for bone. However, there were only 11 different lattice types reported, there is a possibility of a more ideal lattice type for implant use [60].

An EBM Ti-6Al-4V cubic lattice was produced with porosities of 50%, 60% and 70% with a stiffness (2.92-2.13 GPa) that aligns with cortical bone and trabecular bone. The UCS of 50% porosity also matches cortical bone [63]. Octahedral lattice produced by SLM with porosity from 75-%15% has a compressive strength of 20-350 MPa, which is believed to match some of the compressive strength of trabecular bone, which is 0.2-25 MPa, depending on bone type. A hip augment was fabricated based upon previous octahedral lattice, it exhibited a major pore dimeter of 500μm, porosity of 65% and a compressive strength of 53 MPa [52]. A variety of EBM Ti-6Al-4V gyroid structures with porosities of 75% and 90%, along with deformed gyroids were analyzed for use in bone defect reconstruction. All gyroid structures, except for 75% deformed gyroid meet the Young's moduli of trabecular bone. It was deemed that the appropriate gyroid structures could be suitable for areas with long bones, independent of cortical or trabecular bone that predominates regarding the Young moduli. Ultimate strength was also in the range of compressive strength of trabecular bones, meaning for static loads these gyroids could be a good substitute – ultimate strength for gyroids was below that of cortical bone. The research for gyroid points out an important factor of mechanical properties of biomedical implants, a lot of implants are accompanied by an internal fixation system, such as a plate with screws. Physiological loads are thusly distributed between implant and fixation system, creating a total stiffness from plate/screws with the implant. The stiffness should not exceed bone but be flexible enough to produce mechanical stimuli for bone ingrowth inside the implant. Depending on the implant being produce and the bone it is replacing or aiding, fixation systems would be recognized in the total compilation of mechanical properties [85].

4.3 Lattice Manufacturability

There are respective limits for EBM and SLM in terms of printing small and large struts and pore sizes. For example, EBM Acram A2 is limited to electron beam size of 250μm and Acram Q20 electron beam size is 140μm, it is not possible to produce struts thinner than those sizes. Dimensional accuracy will also vary, for EBM the deviation from desired strut size to actual is around 20% for oversized and 21% for undersized. Surface roughness will affect various mechanical properties, EBM parts are rougher than SLM due to coarser powders (EBM 45-105μm EBM, SLM 20-45μm), large electron beam size (EBM 140-250μm, SLM 70-115μm), large layer thickness (EBM 50/70μm, SLM 30/50μm), adherence of partially fused powder, stair-case effect and dynamic unstable melt flow. However, a rough surface can benefit osteointegration, this will be discussed in Chapter 4 [60]. Limits on unit cell size for lattices for SLM are shown to be 5-8mm due to large overhang [84]. Difficulties are also reported on manufacturing lattices with angled struts, such as the octahedral structure with 45°. The angled struts are built with each vertical layer, resulting in a larger strand diameter. Angled struts are seen to have more sintered finish, due to heat being dissipated through the powder, causing powders to be partially fused to the surface. Heat from neighboring struts can heat the powder bed, causing a reduction in amount of energy needed to melt the powder, leading to a larger strut diameter [52]. It was also seen for EBM that strut angle influences the strut quality [60].

In relation to L-PBF parameters affecting mechanical properties, quality is a large factor in insuring properly built parts that will not affect mechanical performance. It has been shown that low beam energy (<0.03 J, SLM, Octahedral lattice) can cause necking in lattice

structures, forming stress concentrations at the necking areas, resulting in complete failure from cracks in struts. The same structures were created with high beam energy (>0.07) and stress concertation wasn't as populated, allowing for deformation instead of complete failure [52].

A major issue with L-PBF is the onset of defects during the build process. Porosity may occur internally from lack of fusion, gas pores in the powder from gas-atomization production process, and trapped gas pores during the build process. These defects effect strength and fatigue properties of the part. Machine parameters such as laser power have a large effect on porosity, surface finish and lack of fusion [123]. Powder bed anomalies also influence part quality, such as incomplete spread – lack of powder causes defect to form. Recoater hopping/streaking, where lines occur on the part finish [124]. Part distortion and residual stress result in part failure, these failures are caused typically by scanning strategy [125]. EBM also suffers from irregularly-shaped lack-of-fusion defects around 100μm. Closed pores from 30-80μm were seen in EBM cubic, G7 and rhombic dodecahedron lattices. For EBM it is believed that these defects are caused by unstable melt flow/evaporation of chemical elements, pores from powder, insufficient melting of local layer-layer contacts and 8% liquid to solid shrinkage of Ti-6Al-4V. It's seen for both SLM and EBM that Hot Isostatic Pressing (HIP) can reduce defects, reduce surface roughness and close pores.

CHAPTER 5

OSTEOGENESIS

This chapter reviews the osteogenesis process, which is the process of bone formation in accordance with orthopedic implants. The four stages of osteointegration are reviewed with emphasis on medical terminology. The purpose of Chapter 5 is to understand osteointegration to design better orthoepic implants and understand what the lattice structures would experience in the human body in terms of cell to cell communication and bone growth.

5.1 Osteointegration

Osteogenesis of a bone implant is purely driven cell process. Molecules extracted from the cells are how cells communicate with each other. The appearance of difference cells occurs in a sequence which is vital to osteointegration. This sequence can be organized into four phases, these four phases are like what is seen in wound healing but is applicable to bone healing and growth. The four phases are: hemostasis phase, inflammatory phase, proliferative phase and remodeling phase. Various cell types involved in the osteointegration process are controlled by genes that are activated by soluble cytokines which consist of soluble protein factors, small molecules of histamine, prostaglandins and more, and lastly molecules from extracellular matrix. Messenger molecules communicate with receptors on cell surface, in turn transmembrane receptor proteins become enzymatically active, which activities an intracellular second messenger system. This second messenger system will either amplify or change information through the nuclear

membrane to DNA. Thus, cellular response begins by activations of genes and certain proteins, through secretory products or intracellular regulatory proteins. The adjacent cells will communicate via direct membrane channels, but for over distances, messengers such as cytokine and hormones are used. The extracellular matrix also relays information to cells via attachment with specific receptors. This osteointegration process review is influenced by a group of doctor's didactic explanation of the four phases of osseointegration of a dental implant, from the publication "Osseointegration – communication of cells" by Dr. Terheyden, Dr. Lang, Dr. Bierbaum, and Dr. Stadliner [135]. This research article also includes an animated video that summarize the publication, which is highly recommend for those unfamiliar with this process [136].

5.1.1 Hemostasis Phase

Hemostasis phase occurs within minutes to hours of an operation, the operation site will be considered a defect. Bone trauma matrix proteins, growth and differentiation factors become active from heparin hydrolases, and from blood platelets via bone trauma. These molecules may also be released from the destruction of bone resulting in bone debris. Injured blood vessels release polymerization of fibrinogen that lay the first extracellular matrix in the defect site. Polymerization of fibrinogen is initiated by platelets and intrinsic clotting cascade, but the action itself is performed by thrombin. The implant surface interacts with water molecules and ions, these ions are followed by plasma protein. Protein absorption increases concentration of proteins on the surface. Protein will bind the surface, such as albumin, eventually replaced by vitronectin or fibronectin. With protein absorption, cells attach to the implant structure (in this case, titanium), this attachment to the surface

is reliant on the blood proteins adhered to the surface. Fibronectin contains cell binding sites RGD sequence that cooperate with integrins, a cellular adhesion protein. Where vascular injuries are present, platelets will form white thrombus that seal vascular leaks. Various bioactive molecules such as thrombin, ADP, collagens, fibrinogen and thrombospondin are created. Fibrinogen and links platelets will form a platelet plug. Fibrin bounded on implant surface will bind thrombocytes over glycoprotein Ib/IIIa receptors to the implant surface, leading to activation and degranulation of thrombocytes. Vasoconstriction will occur from platelets like serotonin and thromboxane. Degranulating platelets will release cytokines, where the next phase, the inflammatory phase begins [135].

5.1.2 Inflammatory Phase

Inflammatory phase occurs 10 minutes after surgery and will last a few days. Platelets with degranulate, releasing growth factors such as transforming growth factor beta (TGF-β), platelet-derived growth factor (PDGF) and basic fibroblast growth factor (bFGF). Platelets release vasodilative which increase blood flow and reducing blood stream velocity, along with inducing hyperaemia. Vasoconstriction from hemostatic phase will turn into vasodilatation. At the beginning of this phase, an innate immune system releases molecular and cellular elements, such as poly morphonuclear leucocytes (PMN) and macrophages. PMN migrate through gaps in blood vessels, this is called diapedesis. Diapedesis occurs from adhesion of lectins in inner lining of blood vessels. Leucocytes will attach to the blood vessel, from here intercellular adhesion molecule-1 (ICAM-1), ICAM-2 and vascular cell adhesion molecule-1 (VCAM-1) will gather granulocyte from the blood stream to bind them to integrins on leucocyte. From this adhesion, endothelial cells will open gaps where

granulocyte cells will move through. PMN will produce elastase and collagenase to move through the basal lamina of a blood vessel. Once these cells have moved on, amoeboid migration begins by chemotaxis. These chemotactic substances from PMN are fibrinopeptides from fibrin activation through thrombin, which are from fibrinolysis, complement 5a, leucotriene B4 from PMN, bacterial proteins (N-formyl methionyl peptides), platelet activating factor (PAF), tumour necrosis factor alpha (TNF-alpha), Platelet factor 4 (PF4), PDGF and interleukin-8 (IL-8). If more bacteria are detected, PMW will release proinflammatory cytokines; the more bacteria present, the great the cellular immune response. PMN can kill bacteria by released reactive radicals, this is also toxic to host cells and healthy tissue. Along with releasing digestive enzymes such as collagenase and elastase that are toxic to tissue. If bacteria cannot be controlled, then a toxic wound environment will develop, where proinflammatory cytokines and toxic radical are high in number. High presence of urokinase plasminogen activator uPA can harm the extracellular matrix, resulting in the fibrin network to degrade. Limiting the number of bacteria in a wound is important due to excess bacteria causing harm to tissues, resulting in implant failure. Elimination of bacteria leads to the proliferative phase. PMN are replaced with lymphocytes and macrophages, what lymphocytes do for the repair process is not well defined, but they do appear to release cytokines which are mitogens and chemoattractants for fibroblasts, along with extracting old neutrophils. As more bacteria are reduced, more macrophages are produced, while bacteria are still present, macrophages release proinflammatory cytokines, this release also signs the end of the inflammatory phase. Once all tissue debris is removed, macrophages also release angiogenic and fibrogenic growth factors. Fibroblast activation is related to the level of cyclooxygenase activity and

prostaglandin production, these factors are also affected by the level of radical nitric oxide (NO) present and inducible nitric oxide synthase (iNOS). Now that the defect sight has been cleaned, cells release tissue inhibitors of metalloproteinases (TIMPs), the TIMPs consume the digestive enzymes of PMN, while protecting protein of the extracellular matrix – promoting growth factors in the extracellular matrix. This follows the release of bFGF and PDGF growth factors from macrophages, high amounts of fibronectin lead to fibroblast attach to integrin biding sites, wherein cells enter the wound; leading to the start of the proliferative phase [135].

5.1.3 Proliferative Phase

The proliferative phase occurs from a few days to a few weeks. The phase beings with formation of a new extracellular matrix and the beginning of angiogenesis, the new tissue is granulation tissue. Fibroblasts from nearby healthy tissue move into the blood clot due to FGF released by macrophages. Through the secretion of matrix metalloproteinases, the fibroblasts drill tunnels into extracellular matrix of the fibrin clot. Metalloproteinases create integrin binding site from fibrin clot, fibroblasts using integrins will attach to RDG peptides of fibronectin to gain deeper access to the wound. The clot matrix is to be replaced, which is where production of insoluble cellular fibronectin and other insoluble proteins such as collagens, vitronectin, decorin and proteoglycans begins. Fibroblasts will indicate movement based on the secretion of growth factors from the macrophages of PDGF, TGF-β, basic FGF and connective tissue growth factor (CTGF). While this occurs, angiogenesis process beings by hypoxia. The hypoxia attracts macrophages, which transform their metabolism to ATP, the macrophages growth factor for angiogenesis is vascular

endothelial growth factor (VEGF) – simulated by hypoxia inducible factor (HIF-1). The VEGF starts the production of endothelial cells, along with other growth factors such as PDGF and FGF. Further responses of VEGF are pericytes from outer walls of the vessel, they digest basal lamina around the vessel. These pericytes lead to new endothelial progenitor cells, thus they move to areas of low oxygen tensions, via attraction of chemokine stromal cell derived factor (SDF-1), produced from the wound. This process is referred to as homing of endothelial cells, from here the cells form groups, arranging themselves into tubes; these new tubes connect to existing blood vessels. With the creation of these blood vessels, blood can now flow. Angiogenesis is the prerequisite for osteogenesis, new bone will only form within 200μm of the nearest blood vessel. Osteoprogenitor cell attaches the implant surface using integrins. Integrins can attach to the extra cellular matrix proteins like fibronectin with RDG motif. For an osteoblast to attach to a metal implant surface, a protein layer must be present. The bone precursor cell produces insoluble cellular fibronectin for cellular attachment to the metal implant. Once cellular attachment is achieved, the osteoprogenitor becomes an osteoblast. Osteoblast is a molecular maker, releasing osteocalcin and alkaline phosphate. Osteoblasts come from mesenchymal stem cells, these stem cells occur from pericytes, from the walls of smallest blood vessels. Pericytes are from bone marrow cells. The bone morphogenetic proteins bind to receptors on surface of bone precursors cells. Receptors I and II activate SMAD protein, where SMAD protein binds to DNA and activates genes Runx. Bone morphogenic proteins (BMP) will bind to single receptors such as extracellular signal regulated kinases (ERK) and mitogen activated protein kinase (MAPK). BMP are found in bone matrix; wherein large quantities of active growth material is available. Where these proteins,

growth and differentiation factors become active from bone trauma and are moved by heparin hydrolases from blood platelets. Various growth factors such as BMP, FGF, PDGF, VEGF are also secreted from matrix by soluble heparin degrading enzymes, these enzymes are then released by platelets, lymphocytes or mast cells. Special proteolytic enzymes such as PDGF-B, VEGF and TGF-β are also released. These factors are also produced by myofibroblasts and osteoblasts. BMPs appear in the wound after three days, meaning bone growth is initially delayed. Various implants have different mechanical stability, orthopedic implants use plates, screws, pins, friction fit and bone cement [137]. Dental implants are held with friction fit via primary bone. Mechanical stability of an implant is also indicated by primary stability. Primary stability is where the highest dynamic load is lesser than the friction holding load. Micromovement can loosen the implant from small movements, hence the need for overloading the implant upon an early phase. These micromovements are common in orthopedic and dental implants [138,139]. Around one week after implantation, bone will start to form secondary bone contacts. The first bone formation is woven bone, the collagen fibers are randomly oriented. For dental implants, woven bone grows along current bone and along the groves of threads. With initial formation, the new bone is not load oriented. In accordance to human volunteer study, it was found that surface modifiers for implants such as ultrahydrophilic SLA can yield faster bone contacts at two and four weeks when compared to a standard SLA surface. New bone begins with release of collagen matrix from osteoblasts, the type of collagen is type II or type III depending on endochondral or intramembranous ossifications. In the end, both type II and type III collagen are replaced by collagen type I. Mineralization process for primary bone formation is quick, woven bone is removed by osteoclasts, replaced by lamellar bone.

Nanometer uniaxially oriented hydroxyapatite crystal plates are formed in the collage fibers. This nanostructure is the key to bones mechanical properties of elasticity and strength, along with bones biological properties. This removal of woven bone from osteoclasts is where the remodeling stage beings [135]. Figure 12 is a SEM image of a titanium thread featuring cell proliferation after 72 hours of in-vitro cell culturing.

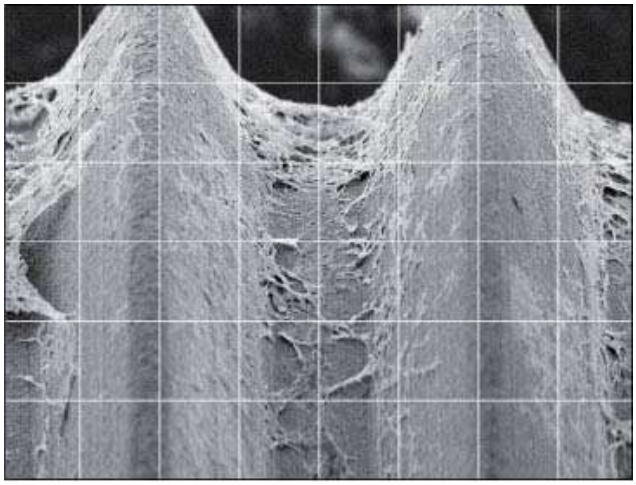

Figure 12. SEM of cellular proliferation on titanium threads after 72 hours, *in vivo* analysis [149]

5.1.4 Remodeling Phase

The remodeling phase can last around several years with complete replacement of woven and old bone with new primary bone. The osteoclasts will appear in the wound after a few days, it will remove primary bone implant contacts to replace with new bone. Lamellar bone is bone created during remodeling; this name comes from the parallel orientation of collagen fibers. Trabeculae will lay out occlusal loads to surrounding bones and to the implant itself, this trabeculae structure can be described as arches in a gothic church. Wolfs law indicates that this trabeculae structure will be built as light as possible, this structure

will also decrease in size during this phase. It is observed that osteoblasts and osteoclasts work interdependently in order to maintain balance of porous and dense bone. During the beginning, osteoclast does not act until osteoblasts do, this controls osteoclastogenesis from RANKL and osteoprotegerin, which are both made by osteoblast. The osteoblast will release RANKL, which is a ligand of receptor activator of nuclear factor kappa beta (RANK) which itself activates osteoclastogenesis with macrophage colony stimulating factor (M-CSF). Osteoprotegerin will preserve bone with osteoclastogenesis. Osteoblast can utilize various bone enhancing and activating messenger molecules such as IL-11, sclerostin, prostaglandin E2, parathyroid hormone (PTH) protein, vitamin D and estradiol. PTH will cause osteoblast to release osteoprotegerin, which causes the appearance of more osteoclast and bone degradation. Osteoclast will attach to the surface walls of blood vessels via SDF-1/CXCR-4. Through diapedesis, the cells will leave the blood stream, then they will move to the basal lamina via matrix metalloproteinase MMP-9. SDF-1, IL-8 and MCP-1/CCL2 are chemoattracted for osteoclast precursor cells to lead them to the bone site. These precursor cells will combine into multinuclear giant cells. Membrane bound proteins are made via neighboring osteoblasts from contact of cells and osteoclast precursors. For the human body, osteoclast will last on average 12 days. Terminally differentiated osteoclasts will absorb the remains of osteoid via collagenases and take over RGD peptide ending from the non-collagenous bone matrix proteins. Lining cells will release from the bone surface, this surface will house osteoclasts, creating a ring like seal with integrin attachment to bone matrix proteins like osteopontin. A resorption lacuna is created between bone and osteoclasts to protect neighbor cells from acid, overly aggressive enzymes and bone resorption. Actively resorbing osteoclast create microscopic folds where hydrochloric

acid is created to demineralize the bone matrix for enzyme cathepsin K to absorb bone collagen. Growth and differentiation factors such as BMP, IGF, TGFβ in the bone matrix are inactive, but can be activated by proteolytic enzymes. As of now, the process of using these growth and differentiation factors is unknown. Osteoclasts do release BMP-6, which can signal BMP from the degraded matrix, BMP-6 and chemokine sphingosine 1 phosphate (S1P) are secreted from the tissue side of the osteoclast. BMP-6 is also the coupling factor for bone resorption and fill, along with differentiating mesenchymal stem cells to osteoblasts to promote new bone. Osteoblastic precursor cells can tell how much bone is needed to fill voids using surface topography via pseudopodia. Osteoclasts will create a tunnel into old bone, which is filled with concentric layers of new lamellar bone. This new bone will contain a central blood vessel, which is called Haversian system or osteone. New bone is formed via mechanotranduction via osteocyte. This is done so bone has good load bearing abilities, the mechanical stimuli is converted into a cytokine signal to the osteoblast. The osteocyte is inside bone and contains cytoplasmatic process in nanoscale bone channels, the fluid shift theory indicates loading of bone causes interstitial pericellular fluid shifts in the channels, where primary cilia organs in the cell membrane induce intracellular signals. The signals travel throughout cellular networks to nearby osteocytes, this network is called osteocyte syncytium. During this communication small messengers such as nitric oxide and prostaglandin signaling. Osteocytes will message osteoblasts using sclerostin, a soluble inhibitor of canonical Wnt signaling, to the PTH signal transduction system [135].

5.2 Pore Size and Osteogenesis

Open cellular structures, also known as lattice structures for orthopedic implant applications are valued for two reasons. The ability to tailor compressive and fatigue strengths for bone compatibility and the ability to promote osseointegration – to grow bone in porous areas to promote stabilization of implant. Varying the size of these pores will affect osseointegration. The average pore size deemed appropriate for osseointegration varies from 400-1000μm [55,62,73,89,140-147]. The classification of what dimensionality pore size is per lattice is unique to every research, Figure 8 is a common representation of what pore size is. One of the goals of this research is to verify mechanical properties of various pore sizes, but another goal is to keep the pore sizes and lattice types in aligned with what would be used in a cell culturing study or in-vivo experiment. The porosity of the implant is vital to long life of the implant, as osteointegration not only provides stabilization, but it provides additional mechanical strength to the implant. Since these structures are complex, it's important a steady flow of nutrients, blood and oxygen can flow in and out of these parts internally, this is coined permeability. If this flow is successful, then the possibility of promoting angiogenesis (new blood vessels) and vasculogenesis (developments of vascular networks) is possible. Permeability is vital to osteogenesis, as waste removal is vital to growth of bone cells, as mentioned in the previous sections. This cell to cell communication is vital to various nutrients viewed as proteins and growth factors. Higher permeability indicate less resistance in the internal lattice, and high fluid velocities. However, this can give cells less time to attach to surfaces, as seen with larger pore sizes. Smaller pore size decreases permeability, where internal flow resistance is greater - allowing cells to adhere to surfaces [55]. In the same study, it was

viewed that larger pores size is ideal for cell growth due to more open space for cells to grow, this is called surface area. Along with higher medium diffusivity with initial larger pore size and less pore occlusion that favored the oxygen and nutrient supply. Smaller pores also have increased proliferation due to higher surface area, allowing better growth and bone adhesion, along with better cell bridging for pores [62]. It is believed that larger surface area is key to greater osteointegration, this term is one of the key areas of interest. Mature bone growth is not possible without the development of angiogenesis and the vascular network, reports indicate that bone cannot grown if not within 200μm of a nearest blood vessel [135] and cells cannot survive if not in a vicinity of 25-100um of a blood supply [144]. A cell culturing study on a gyroid structure with pores around 255μm was deemed a failure in generating bone growth after 10 days; a dense layer of dead cells was found on this structure. It was believed that both the faults of static culturing and the size of the pores that caused pore occlusion were to blame [144]. A study on static and dynamic cell culturing of three different lattice structures (cubic, diagonal and pyramidal) found that smaller pore sizes (400-620μm) with a pyramidal unit cell had higher metabolic cell activity and migration when compared to larger pore sizes. However, these larger pore sizes were associated with different unit cells [62]. A dental study features various pore sizes of 300-650μm with diamond unit cells, and the study found that pore sizes larger than 650μm do not enhance cell ingrowth, with the ideal size found to be 250-650μm. Diamond crystal lattice structures featuring pore sizes 300, 600 and 900μm were tested *in vivo* with rabbits, it was found that 600μm and 900μm were better at vascularization bone compared to 300μm. This report indicated (as did others) that higher average curvature will induce higher tissue amplification *in vitro*. Essentially, the same unit cell with different pore sizes

has the same cross-sectional shape, but the average curvature of the pore becomes higher in inverse proportion to the pore size. Through this belief, smaller pore sizes should have an advantage, although the study found that the smaller pore size 300μm was truly affected by negative vascularization. However, this theory could be correct, since 600μm at 2 weeks of growth had higher bone ingrowth when compared to 900μm. There is a possibility of an ideal size that fits both vascularization and positive effects of curvature.

Surface area was also reviewed, in this case using fixation ability of *in vivo* implant; it was theorized that 300μm would have the greatest fixation due to greater surface area. At 2 weeks, 600μm was found to have better implant fixation than 300μm and 900μm, it was believed that reduced vascularization of 300μm is what causes the loss of implant fixation. At 4 and 8 weeks of *in vivo* testing, implant fixation for all three pore sizes was high. It was found after 8 weeks that the bone matured into cortical bone and cortical continuity. Marrow-like tissue also grew into the pores of the implant, proving that bone and soft tissue can grow into the pores. It is believed that pore throat size is essential to this vascular tissue-ingrowth and bone conductivity. The study concluded that 600μm is the ideal pore size for diamond crystal lattice due to its early bone growth, deep bone growth and mechanical properties [142].

5.3 Unit Cell Geometry and Osteogenesis

The structure of the unit cell used in lattice structures is seen to have various effects on osseointegration. It is believed that the unit cell wall size and structure have a higher influence on bone growth than pore size, but the study that confirms this only relies on

channels instead of a complex 3D lattice [148]. The interconnectivity of pores must be understood as it influences osteogenesis. A study on replicating commercial implants of various structures such as diamond crystal lattice regular distribution, diamond crystal lattice irregular distribution, diamond crystal lattice gradient distribution and tetrahedral structure with truss frame. The diamond crystal lattices of regular and irregular were seen to perform the best with bone growth during cell culturing, while diamond crystal lattice gradient distribution performed the worst. However, all these lattice types did promote osteogenesis. An *in vivo* push out test of these lattices in rabbits showcased good mechanical stability when compared to a compact implant (control) [141]. A study focusing on cubic, diagonal and pyramidal lattice structures found the pyramidal structure had the highest metabolic cell activity and migration when compared to cubic and diagonal [62]. A common unit cell used in this area of research is the diamond unit cell, it is believed to be ideal due to its ability to mimic properties of cancellous bone and having relatively low stiffness in relation to its density [145]. The strut size does not only affect mechanical properties of the lattice, but in this case the surface area. In a comparison of 120μm and 230μm strut sizes, 120μm has a more direct bone-titanium contact in a in-vivo study with rats. It was found that bone volume was higher in 120μm compared to 230μm for the *in vivo* analysis [143]. The shape of the pores influences cell distribution, where cells will bridge the corners. It was concluded that bridging behavior is material geometry independent [55]. A study on diamond crystal lattice structures of various pore sizes (300,600,900μm) concluded the use of diamond crystal due to analysis of *in vitro* testing that tissue amplification was seen to be better for hexagonal shapes compared to

square/triangular shapes. These results might indicate the diamond crystal lattice a superior structure for tissue amplification [142].

CHAPTER 6

IN SITU PROCESS MONITORING VIA GLOBAL IR

The onset of defects in L-PBF is a common occurrence during the production of parts. Due to the layered structure of these components, defects occur due to incorrect process parameters, mechanical failures and contamination. For example, gas entrapment inside gas atomized metal powders causes spherical pores in EBM [170]. High laser energy density for SLM can cause high porosity, warpage and splatter satellites. Low laser energy density may cause cracks and balling from high viscosity of the metal pool [171]. Process monitoring is a method of monitoring the L-PBF during the production of components via sensors. Through the monitoring of the build process, defects and anomalies can be observed and monitored through a variety of image-processing and machine-learning techniques to identify and track the location and severity of potential problems. Various sensors are used for monitoring, such as melt pool radiation sensors [172], visual camera [173], infrared (IR) thermography [174], pyrometer [175] and melt-pool monitoring [176]. Gathering data from the sensors is valuable, but processing of the data can indicate further detail of defect formation, how process parameters of the machine cause defect formation and identification of defects.

Many different processing techniques exist for each *in situ* sensor, such as image processing, which can create optimal images for analyzing defects and anomalies [172,174]. Machine learning algorithms are a powerful tool in processing data due to the various types of classification that can be performed. Principle Component Analysis (PCA)

can be used to identify defects per layer by highlighting key information in images, in addition to PCA; k-means clustering can be used to create automated defect detection [173]. Neural networks are valuable tools for extracting features from sensors to identify defects, such as Deep Belief Network (DBN) and Convolutional Neural Network (CNN). A DBN was used monitor quality of components via plume and spatter image signatures. This DPN was compared to other neural networks such as CNN and Multilayer Perceptron Neural Networks (MPNN), where DBN outperformed both CNN and MPNN in terms of classification accuracy [177]. Another valuable aspect of DBN found in this study was the convivence the program offered compared to other neural networks, with less image preprocessing and less empirical analysis during *in situ* monitoring. However, the CNN only performed 0.68% worse than the DBN [177].

A CNN was used via powder bed camera to detect powder bed anomalies such as recoating hopping, recoater streaking and incomplete spreading. A case study of multiple builds and materials was analyzed and found the CNN was robust for anomaly detection. The CNN is a modified form of Multi-scale CNN (MsCNN), where it was compared against a normal CNN and Bag-of-Words (BoW). BoW is a type of image classification, a comparison of MSCNN and CNN revealed MSCNN to be superior [177].

Following the comparison of ideal neural networks, the ideal form of process monitoring needs to be identified, as a goal needs to be set. The ideal form of process monitoring is a feedback loop integrated between *in situ* sensors and machine parameters. For example, if

an IR camera detects balling on the current layer as the laser is scanning, the machine would alter the laser energy density parameters to correct this defect.

A closed-loop control system, along with NDE could make a case for reliable manufacturing of high-risk parts more attractive for various industries. It's observed that better process monitoring is a key factor in the emergence of AM technology in industry. The more reliable and better quality the parts are, the further demand is increased for L-PBF technology [1]. L-PBF is also an expensive process, even more with expensive powder such as titanium and Inconel, reducing failed prints would lessen the economic burden this technology bears.

6.1 Case Study

Previous work of this author involved implementing a CNN to detect geometries from *in situ* data [198]. The *in situ* data was gathered via a global IR camera. The SLM machine used is of an open architecture design, specifically made for *in situ* data gathering. A CAD part was created via SolidWorks, containing multiple features that change throughout layers. The features mentioned are squares, circles and triangles in an array of sizes and positions that provide statically-significant quantity of detection opportunities for the sensor system. The part has four feature layers and four solid layers. The part exterior dimensions are 25.4×81×8 mm. The shapes at the first layer are sized at 3.5, 3, 2, 1 and 0.75 mm^2, after each feature layer, a solid 1mm layer is used to build upon the next feature layer; all features are cut into the part. The second feature layer mimics the first feature layer, but all the dimensions are increased by 20% - the first column of each shape is left

unchanged for statistical reasons. For the third feature layer, the aspect ratio for all symbols are changed by 25%. Circles have turned into ellipsoids, enlarging from various angles. Squares and triangles are enlarged by 25% on the X-axis; the first column of all shapes is the same as the first feature. The fourth feature set is a mimic of the first feature set. Figure 13 are the first- and third-layer feature geometries, note the difference in dimensions and geometries.

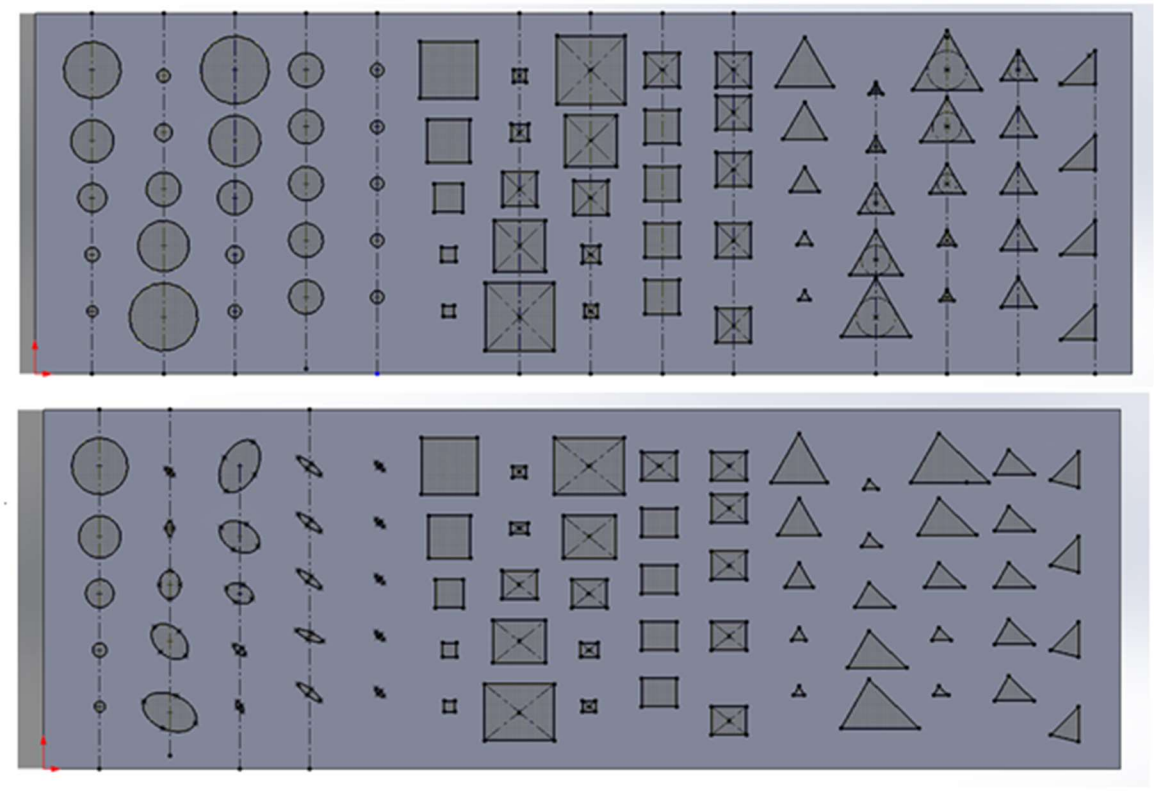

Figure 13. First and third-layer of CAD part, note the change of dimensions/geometries between layers

6.1.1 Image Pre-processing

After collecting the IR data, noise is present throughout the images, as seen in Figure 14. To remove this noise, image processing techniques are used to enhance the images and

images and improve object detection as part of the pre-processing for a CNN. First, a Fast Fourier Transform (FFT) is applied on IR frames. The edges of the shapes and pixels differ than the background appear clearly in the magnitude of FFT, seen in Figure 15. The second stage is Principal Component Analysis (PCA), also known as Principal Component Thermography (PCT) [178], is an orthogonal linear transformation that transforms the thermogram sequence into a new coordinate system. The idea behind PCA is to remove possible correlation in the data by creating a new uncorrelated dataset called Principal Components (PC). This is a known technique used in thermal NDT for data reduction and flaw contrast enhancement [179]. Once eigenvectors are found from the covariance matrix, eigenvalues are ordered from highest to lowest. This gives the components an order of significance, in which the first PC content contains the most object information. Lastly, a filter is applied on the first PC image, known as a Laplacian filter – where areas of rapid change (edges) will appear. Figure 16 is end result with an image with highly emphasized edges that makes object-detection algorithms more efficient and accurate. This approach is valid because areas of interest will always be defined by sharp transitions from powder to solid metal. The overall approach is to identify these areas of transition and compare them with the initial CAD model, enabling the monitoring of important image features. Some features worth monitoring from layer to layer are object location, total object area, aspect ratio, and maximum (or minimum) temperature.

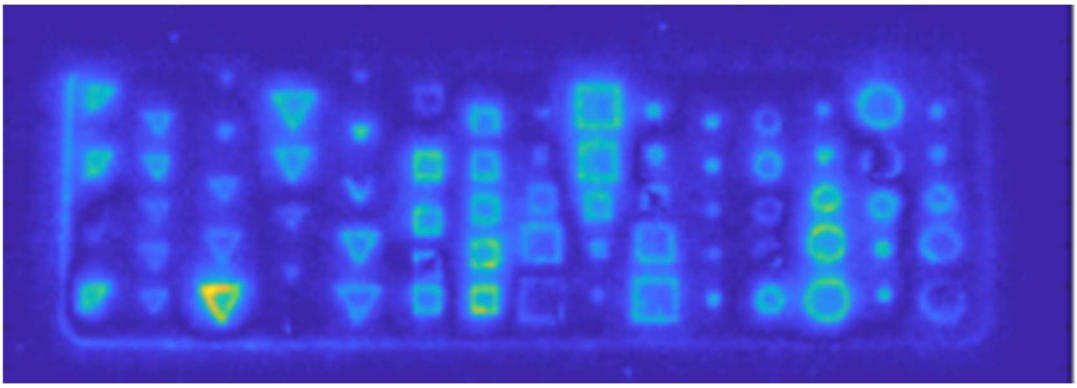

Figure 14. Raw IR Image

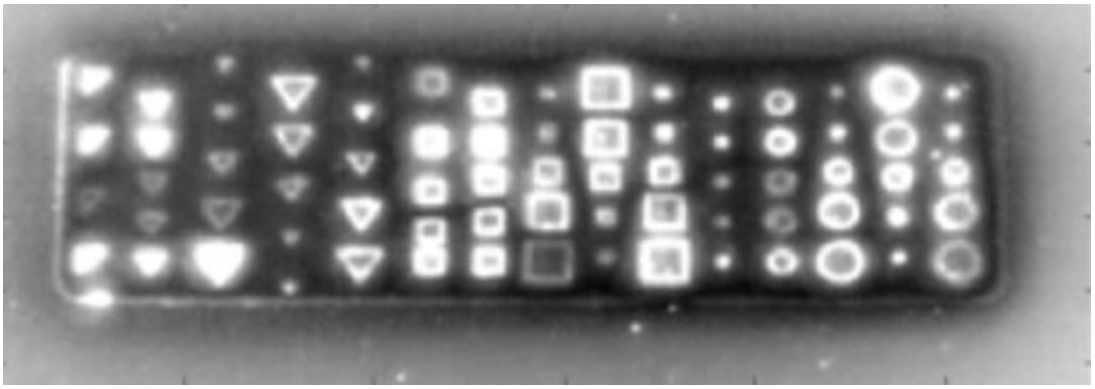

Figure 15. FFT applied on raw IR image

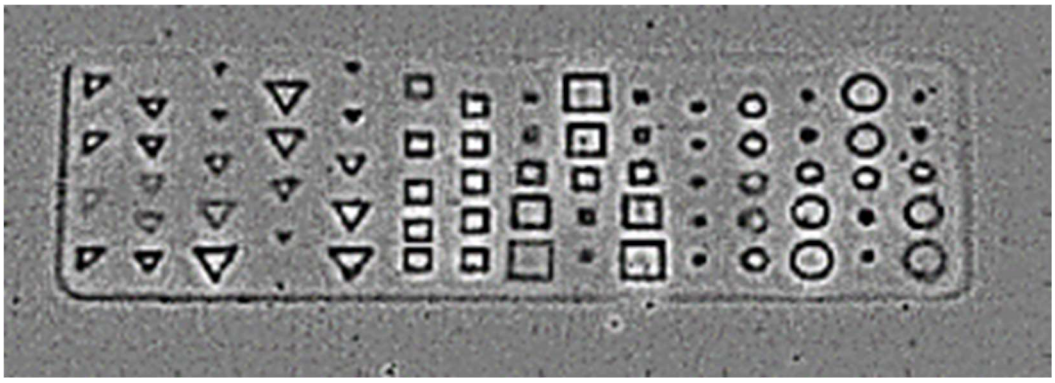

Figure 16. Complete pre-processed data after PCA/Laplacian filter application

6.1.2 Convolutional Neural Network and Training

A Convolutional Neural Network (CNN) is a machine learning algorithm where Deep Learning is applied to train a neural network on recognizing patterns with high accuracy. Due to the limited data available, transfer learning with AlexNet is used to make up for this deficiency [180]. Based upon the author's previous work using Artificial Neural Networks (ANN), it was found that CNN would net better results due to high classification accuracies. CNN was also ideal for extracting objects and edges [181], typically these images must be converted to binary images [182]. Previous work of the author found with ANN that binary images would discard valuable information within the IR imagery, rendering inaccurate results [198]. It should be noted that the data has noise, even with applying image processing techniques, noise from the camera resolution is still present and affects end results. The classifications for the CNN are circle, square and triangle.

CAD images are used to train the CNN. A pre-processing technique was applied to the CAD images to create an appearance similar to the first PC. Using CAD images as training data is ideal due to the CAD imagery being the absolute perfect representation of the part, anomalies can be detected easily due to the ideal representation. A sliding window is applied to separate each shape in its own image, the orientation of the shapes is changed, along with sizing of the shapes to obtain better results. This process was applied for each different layer of the CAD part.

Two approaches for training the data were used, converting the CAD image to a binary image was the first approach, and the second approach (Figure 17), pre-processing was

applied to create images similar to the IR imagery – no binary conversion was applied. It was found the second approach is ideal because there is no information lost (shape, defects), that typically be found by applying a binary conversion to the images. The input image for the binary training set is the first PC of the IR image with a filter applied to it, then converted to binary. The input image set for the second approach training set is the first PC with just a filter applied.

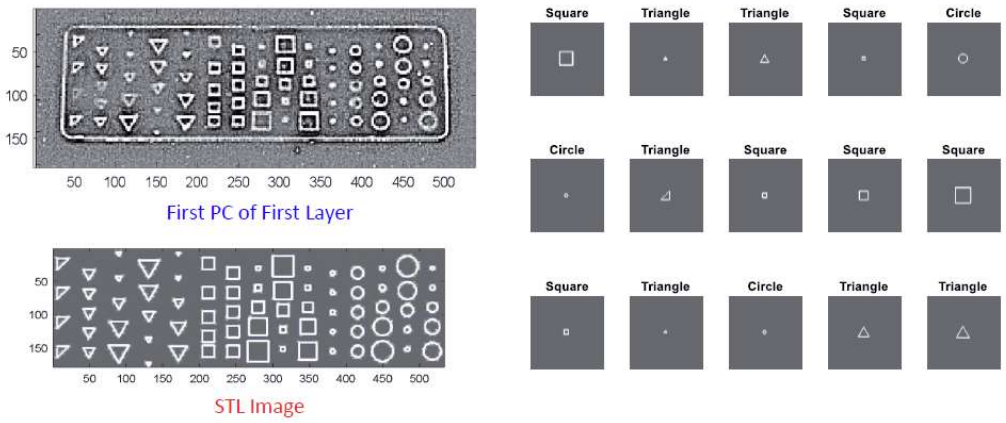

Figure 17. Training and test images for second approach

6.1.3 Results

Analyzing both training approaches, Table 8 and 9 are the results for both binary and non-binary approaches. Validation accuracy is the overall accuracy of the neural network in relation to how well it will classify new information (images). Overall, the binary training set is ideal for triangles, where the non-binary training set is ideal for circles and squares. For neural networks, validation accuracy should be better than 50%, as 50% is representative of a coin flip. It is apparent that circles are difficult to analyze with either

approach, or this may be because of the round edges are difficult to define, which could be the fault of low resolution of global IR.

Table 8: Binary training validation results

Shape	**Validation Accuracy**
Triangles	1
Circles	0.36
Squares	0.53

Table 9: Non-binary training validation results

Shape	**Validation Accuracy**
Triangles	0.64
Circles	0.45
Squares	0.76

CHAPTER 7

DESIGN OF EXPERIMENTS

7.1 Introduction

One of the goals of this thesis is to validate diamond and cubic lattices structures, in terms of design, and manufacturability. Diamond and cubic lattices have already been manufactured and show promise in areas of mechanical strength and bone growth. For example, it has been shown that a diamond unit cell is ideal for orthopedic applications because of its simplicity, low stiffness in relation to density, mechanical properties similar to bone and ability to promote osseointegration [145,60]. The cubic lattice has been shown to match mechanical properties similar to human bone, while also being considered one of the most ideal lattices for orthopedic implants according to a large study of EBM lattice structures [60]. It has been shown that osseointegration can occur in cubic lattices [62]. These two lattices were designed in various pore sizes, 400, 500, 600 and 900μm. These pore sizes are representative of what is believed to be the ideal pore sizes for promoting osseointegration [55,62,73,89,140-147].

7.2 Materials and Methods

This section will review the process of designing the lattice structures using CAD software, a discussion of the titanium material used, and the selective laser melting system used for this experiment.

7.2.1 Computer-aided Design

Two different CAD software's were used to design the lattices, the cubic lattice was designed with SolidWorks and the diamond lattice was designed with 3DXpert. The SolidWorks design was made via a 10mm cube with extruded squares to build a cubic lattice. As SolidWorks isn't optimized for the extrusion of thousands of holes, this procedure is lengthy, but it provides less errors during the file conversion to a stereolithography (STL) file, in comparison to other methods of lattice creation. 3DXpert is optimized for lattice structure creation; using a 10mm cube, a user can simply use lattice topology optimization. This optimization procedure will lay out the placement of struts and nodes based on user defined parameters of unit cell size, strut thickness, node thickness, lattice type, node type and strut type. Both diamond and cubic lattices are $10mm^3$ cubes. Both lattices will be produced with 400, 500, 600, and 900µm pore sizes and all lattices have 2mm strut diameters.

Tensile specimens of cubic and diamond lattices were produced for all pore sizes via SolidWorks, the 3DXpert files for diamond lattices were converted to STL files and uploaded into SolidWorks. The tensile specimen follows ASTM E8/E8M Standard Test Methods for Tension Testing of Metallic Materials in regard to tensile specimen for powder metallurgy (P/M) products [184]. Figure 18 is the cubic lattice CAD files; Figure 19 is the

diamond lattice CAD files, and Figure 20 is a tensile specimen of a diamond lattice made CAD file.

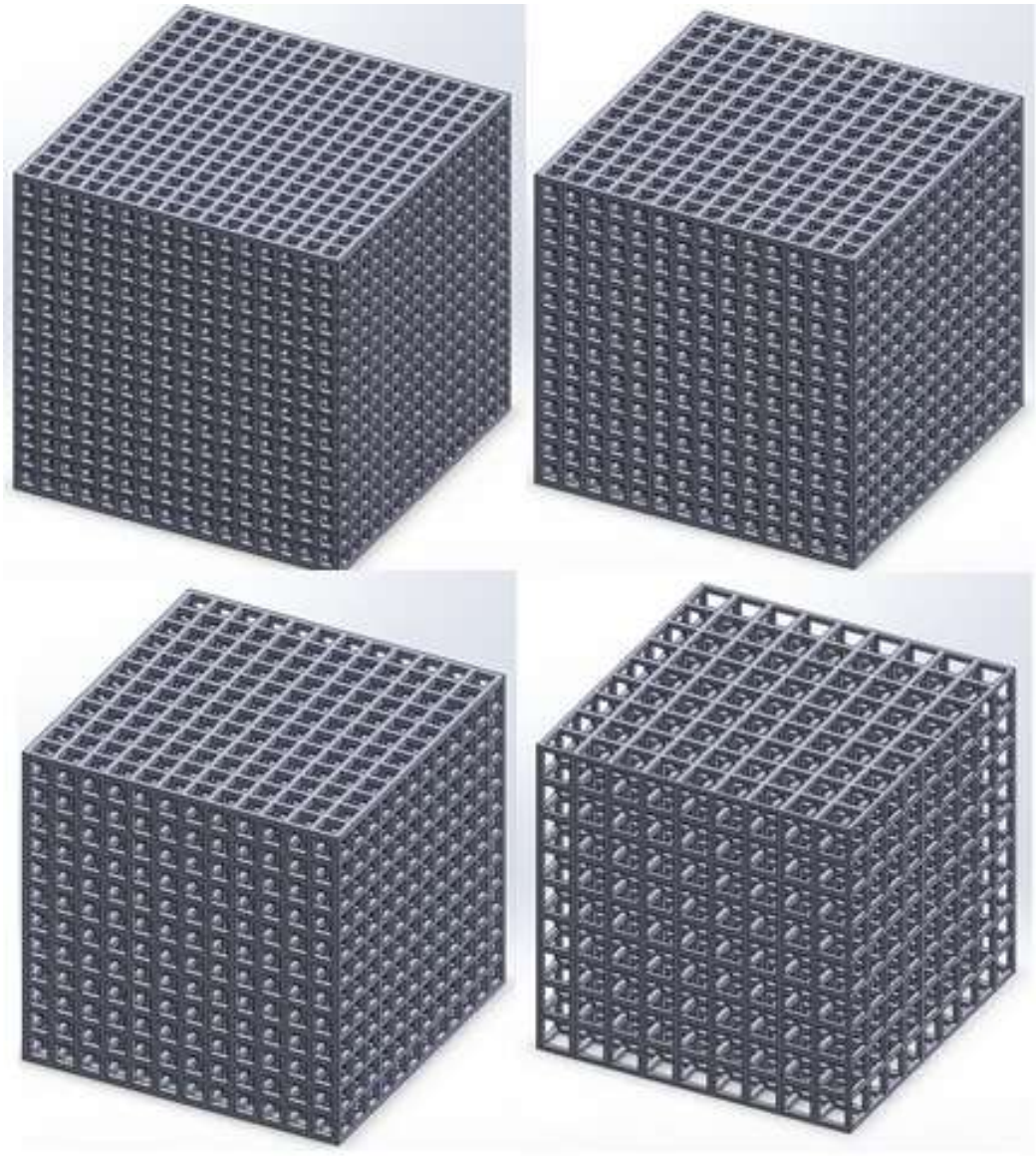

Figure 18. Cubic lattice from SolidWorks, left to right: 400µm, 500µm, 600µm, 900µm

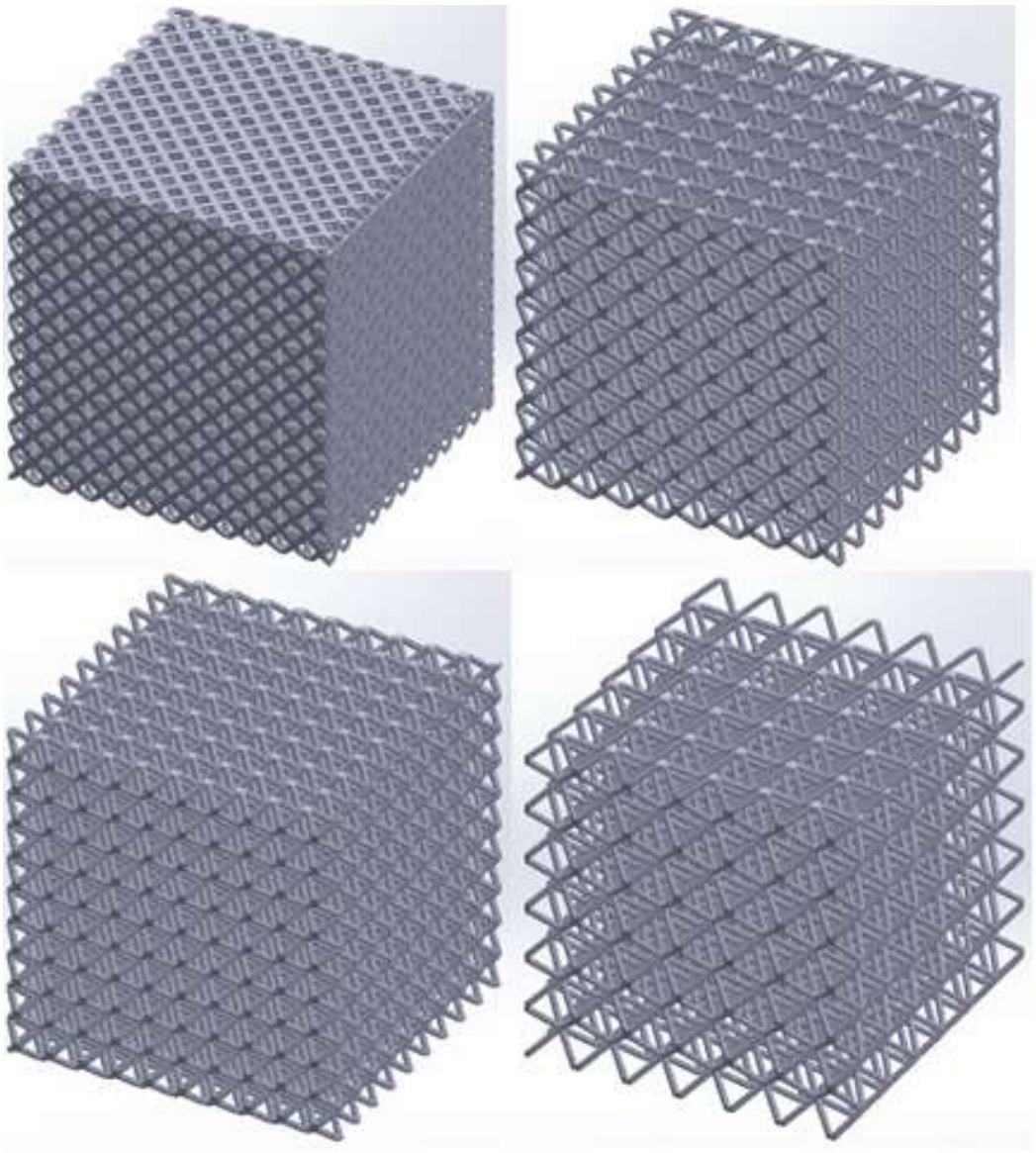

Figure 19. Diamond lattice from 3DXpert, left to right: 400µm, 500µm, 600µm, 900µm

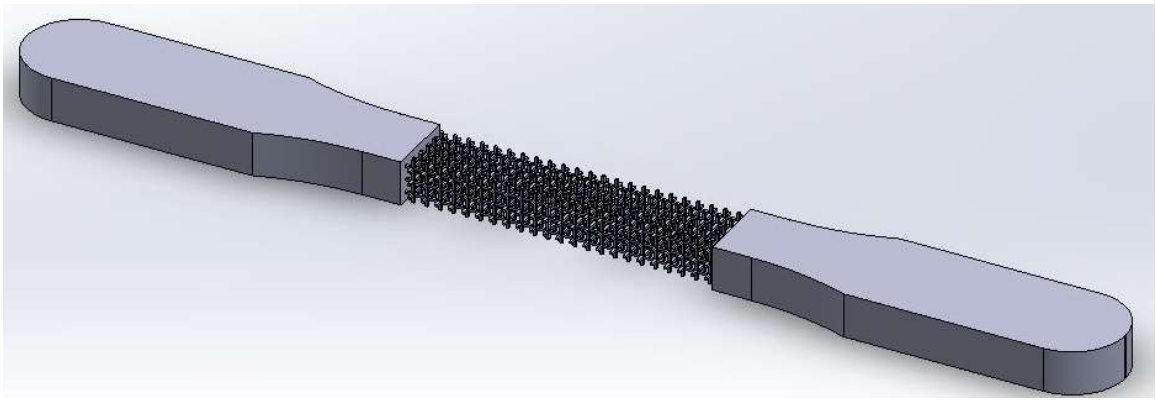

Figure 20. Tensile specimen of diamond lattice pore size 600µm

7.2.2 Materials

Ti-6Al-4V powder from AP&C is used for SLM. This powder was leftover powder from a previous SLM machine, the powder was sieved to reduce any irregularities to 15-53µm.

7.2.3 Selective Laser Melting

An open architecture SLM system called DART developed by University of Dayton Research Institute for *insitu* process monitoring was used to create all the lattice cubes and tensile specimen. The laser is IPG YLR500 500W laser with a spot size of 80µm. The laser power per build varied around 150W. The laser scanning speed is 950 mm/s and the hatching distance is 0.08mm. The laser powder thickness is 0.08mm. All parts produced were stress relived. The diamond, cubic and tensile specimens were divided into three separate builds. The reason for dividing the build was due to the 4x4 inch build plate, all the specimens could not fit on one build. Within each build, a 10mm solid cube for lattice cubes and a solid tensile specimen were also printed to evaluate build quality via NDE. The build of the diamond lattices resulted in an error where only 7mm on the Y axis was

created, thus the diamond cubes are 7x10x10mm. The cubic lattices were successfully printed. Although NDE was not performed due to time restrictions, SLM can successfully produce lattice pore sizes up to 400µm small from the perspective of a human eye, however it is possible that inner pores are obstructed. The only way to identify this is with SEM or CT-scanning, which will be performed in the future. Figure 21 is the built cubic lattice, Figure 22 is the built diamond lattice, and Figure 23 is the built tensile lattices

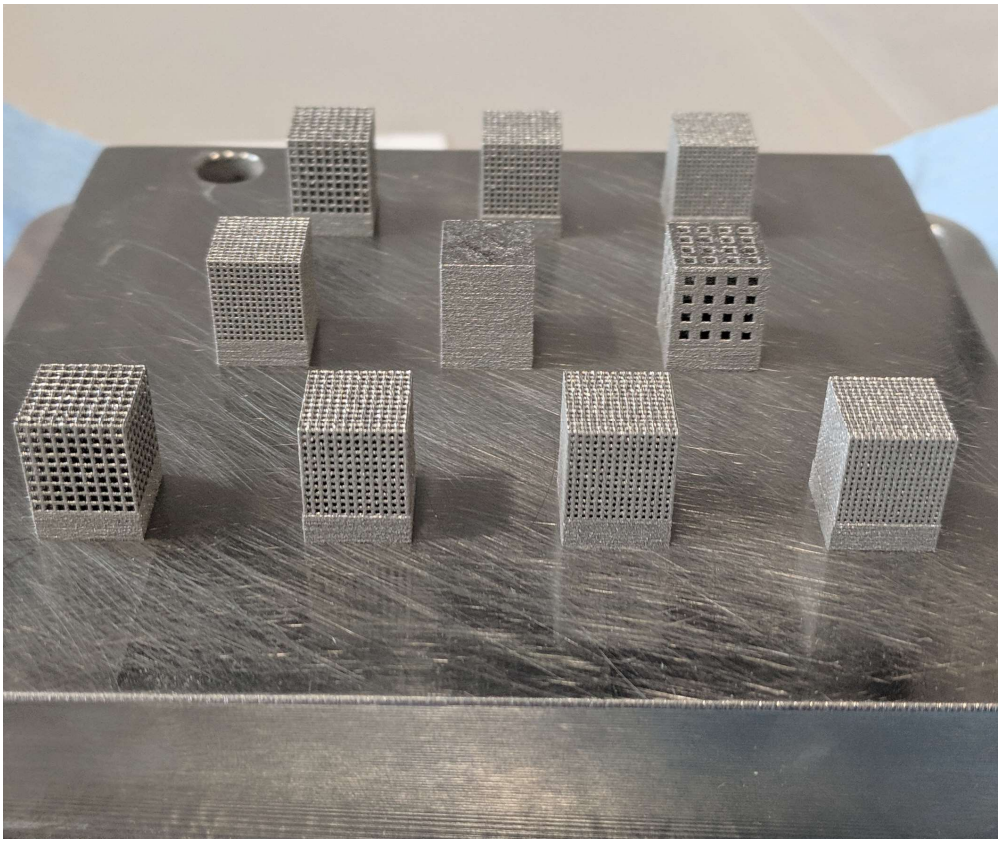

Figure 21. Cubic lattices via SLM

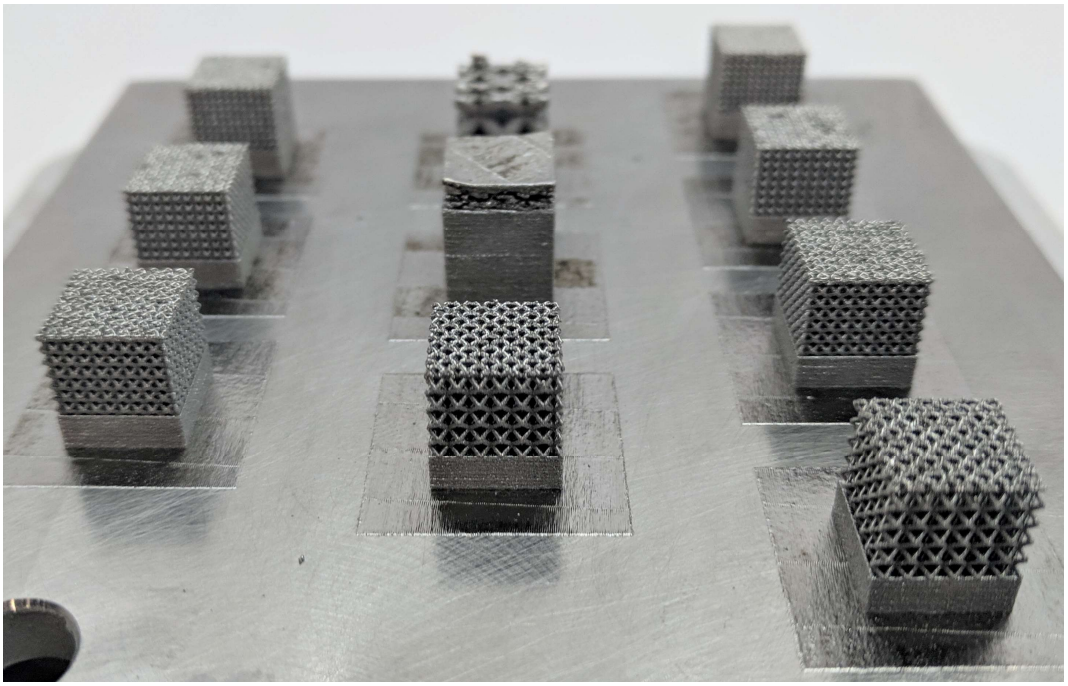

Figure 22. Diamond lattices via SLM, note the defect formation on the middle cube

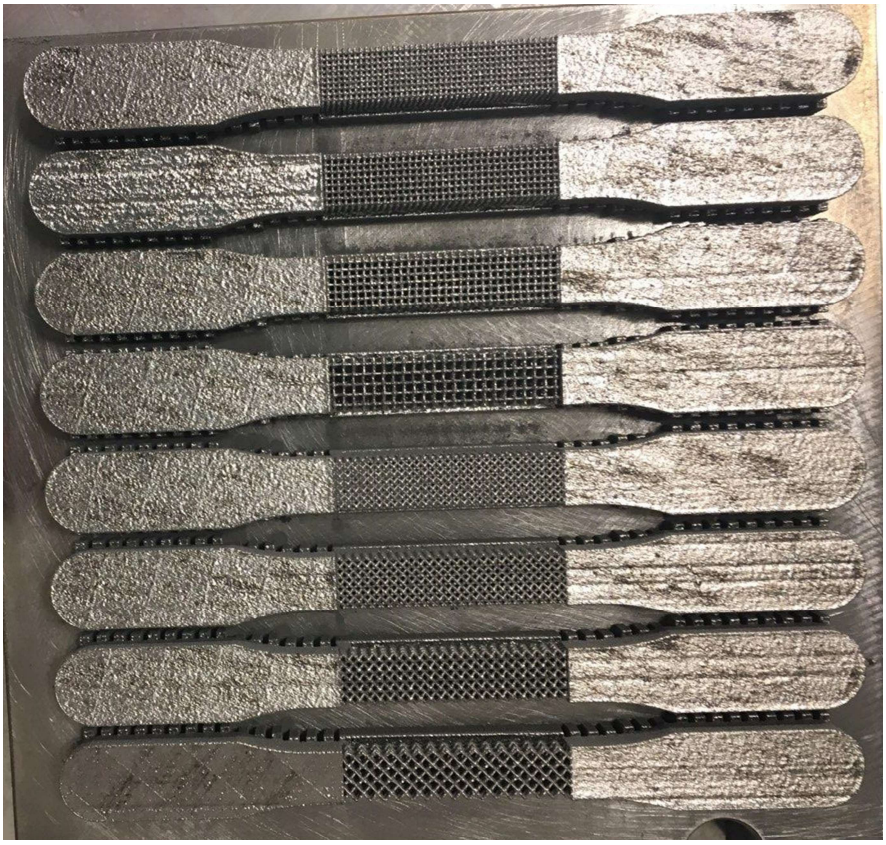

Figure 23. Tensile specimen via SLM, diamond and cubic lattices

CHAPTER 8

IN SITU PROCESS MONITORING WITH IR TOMOGRAPHY

Using Infrared Tomography data from the build of the cubic lattices via the open architecture SLM DART system, image classification was performed via CNN. Similar in approach to Chapter 6, the main difference is the creation of an augmented training set, instead of relying on pretrained data, such as Alex net. Creation of a neural network that can recognize geometries from CAD data is valuable for defect detection and quality assurance of parts, as described in Chapter 6. This chapter will review the pre-processing of the IR tomography, the makeup of the convolutional neural network and results of the neural network.

8.1 Case Study

There are concrete differences between the global infrared camera and infrared tomography. IR tomography could be classified as a visual camera with an infrared filter; however, a better description is to consider IR tomography as near-infrared, with a wavelength between 0.75-1.4 μm. The wavelength of IR tomography is smaller than the global IR, global IR wavelength is around 3-8μm. IR thermography has a higher resolution when compared to global infrared, which is ideal for detection of geometries. The resolution is the result of using an optical camera, which are commercially available in higher pixel resolutions than true IR detectors. It is also believed that less pre-processing will have to be performed to the image input for the CNN. This case study focused

exclusively on IR tomography of the cubic lattice, focusing on sizes 400, 500, 600, and 900μm.

8.2 Programming Environment

MATLAB R2018b was used for developing of image processing and neural network. The following toolboxes were also used: MATLAB Compiler, Image Processing Toolbox, Statistics Toolbox and the Neural Network Toolbox.

8.3 Image Pre-processing

Due to the enhanced clarity and reduced noise of the IR Tomography, in comparison to global IR, minimal pre-processing was performed. PCA is performed on the IR image, the first PC is used as it represents the data the best. When applying PCA, a certain amount of image information is lost during the process to bring out key features that are deemed important. This loss of information could be crippling to a neural network, however since the images are fairly simple, it is easy to identify if key information was lost. It is believed in this case that all necessary information is present. Figure 24 is comparison of a raw grayscale IR tomography image and the processed image using the first PC.

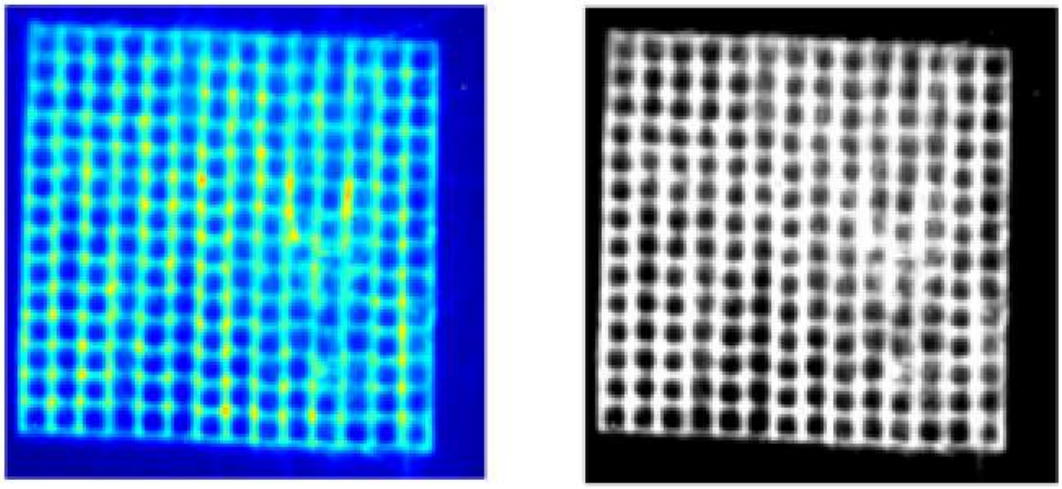

Figure 24. Left: raw IR Tomography, right: first PC of PCA of 600µm cubic lattice

8.4 Convolutional Neural Network

8.4.1 Training Data

Similar to Chapter 6, CAD images of the lattices are used to train the neural network. The CAD representation of the lattices are the perfect representations of a part; hence it is believed to properly train a neural network to recognized geometries, using the perfect representation is ideal. Due to the simple structure of the cubic lattice, there are only two possible training images per lattice pore size, one image is the full face of the lattice and the other image are the struts of the lattice being built. Figure 25 contains the two CAD images. Taking all four lattices sizes, there are only eight possible training images for the neural network, eight images is too small to train a neural network. To make up for this lack of training data, the training images were augmented. Data augmentation is common in neural networks for creating a larger training dataset, as the augmentation creates new images. There are various techniques to augment data, such as image shifting, zooming

in/out, noise induction and altering colors [186]. The augmentation is done through two techniques, the first technique is a random rotation of the training data from 0 to 90 degrees. The training images are 300x300x3. The second technique is to apply random isotropic scaling to the image. Figure 26 showcases some augmented images.

There are 100 training images for each CAD image, meaning there are 800 training images total when taking consideration of two CAD images for all four lattice structures. This indicates that there are 8 classes being trained on the neural network.

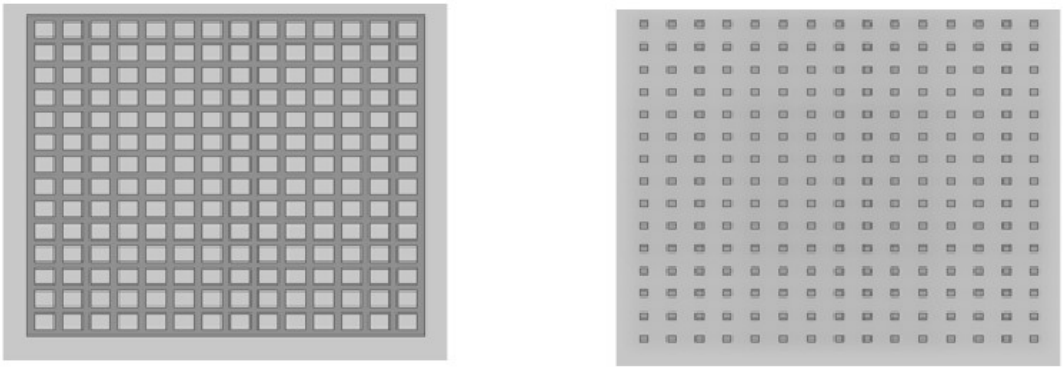

Figure 25. Left: Face of lattice, right: struts of lattice

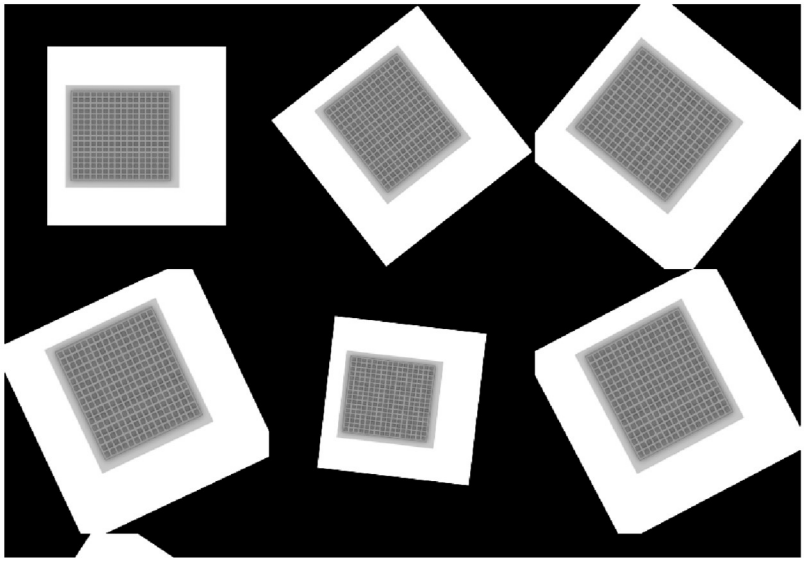

Figure 26. Augmented training data set

8.4.2 Input Layer

The input layer is the first layer in the CNN, it is where the input image is applied into the neural network, along with data normalization. The input images are all 400, 500, 600 and 900μm cubic lattices applied via PCA, only using the first PC. The input images are resized to 300x300x3 to match the training data. For every run of the neural network, only one input image is used, thus each lattice structure has its own unique neural network [187].

8.4.3 Hidden Layers

The first layer is the image input layer, typical to most CNN. The main portion of our hidden layers can be divided into six sections. Each section contains a convolution layer, a batch normalization layer, a ReLU layer and a max pooling layer. Each six section contains these four layers, they are all applied in series. The convolution layer is where a convolution filter is applied to the input image, the filters are moved across the input image, where the dot product of weights and input is found. The filter sizing and number of filters can be changed, for this neural network the filter size is three and the number of filters vary per section. Batch normalization normalizes each input channel based on the value of a mini-batch, this is done to decrease training time by keeping mean activation near zero and the standard deviation of activation near 1. The ReLU layer turns any negative values found in the inputs to zero. Max pooling layer reduces computation in the network and reduces overfitting by reducing spatial size of representation, this reduces overall parameters. The pool size is a property that can be changed but is common to be two by two or three by three. The main difference of each section is the number of filters for the convolution layer. The first section contains three filters, this value will change in the following order for each

six sections: 3, 16, 32, 64, 3, 128. After these sections are the last three layers: fully connected layer, Softmax layer, and classification layer. The fully connected layer represents the feature vector for the network, taking in the number of image categories, which in this case is eight, and performing feature extraction based on the previous layers. Softmax layer assigns probabilities to each class, thus the total probability is 1, this is done to speed up the training process. The last layer is the classification layer, where cross entropy loss for all classifications is computed, working in conjunction with the Softmax layer [187, 188].

8.4.4 Training Options

MATLAB has a host of options for training neural networks, essential for fine tuning a neural network. This CNN follows stochastic gradient descent with momentum optimizer. Initial learn rate is set to 0.01, which affects the over learning rate of training. A value that is too high or too low can lead to bad results. Eleven epochs are used, each epoch is classified as full pass through the entire training set. The option to display training data is selected. Shuffling of data is selected for every epoch, meaning with every epoch the training and validation data are shuffled. Mini-batch size is restricted to 64, due to computer memory; the min-batch will update the weights of the stochastic gradient descent to update the entire network to a small subset of training, restricted by a small training set by the indicated mini-batch value. Validation data is utilized to find the validation accuracy [192].

8.4.5 Results and Discussion

To check network performance, validation accuracy was used. Validation accuracy is how well the neural network performs when encountered with new data, essentially ensuring that results are reproducible. The results are posted in Table 10. A strut image is used from the same time period of the build for all cubic lattice pore sizes. The neural networks run for five times, each time the validation accuracy is recorded, then the mean validation accuracy of the five runs is used for each lattice pore size.

Table 10: Validation Accuracy for strut input image

Cubic lattice strut sizes	**Validation Accuracy (%)**
P400	70%
P500	65%
P600	82.5%
P900	58.75%

P900 is the lowest accuracy, P900 is the largest outlier when compared to P400 or P600, there is less strut material and more space between the struts. From a visual inspection, P500 and P600 are difficult to distinguish, while P400 and P900 stand out the most. There is a similarity to P500/P600 with P400, then say P600 to P900. The standard deviation for Table 10 is 10.07, with an overall mean of 69.06. Figure 27 are two strut input images.

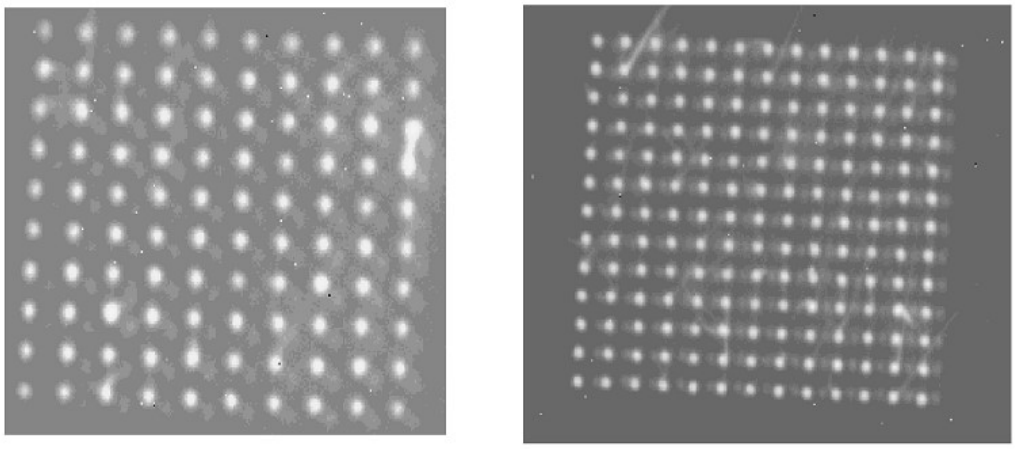

Figure 27. Input strut image of P400 and P500

Figure 25 is the plot of training accuracy and loss for P600. The dotted lines for the accuracy are the validation accuracy and the dotted lines for the loss are the validation loss. It is ideal for a neural network loss to become lower in value as more iterations occur. The validation accuracy for this plot is 75%. Figure 28 is training and loss plot for P500, validation accuracy 87.5%. validation accuracy for this plot is 75%. Figure 29 is training and loss plot for P500, validation accuracy 87.5%.

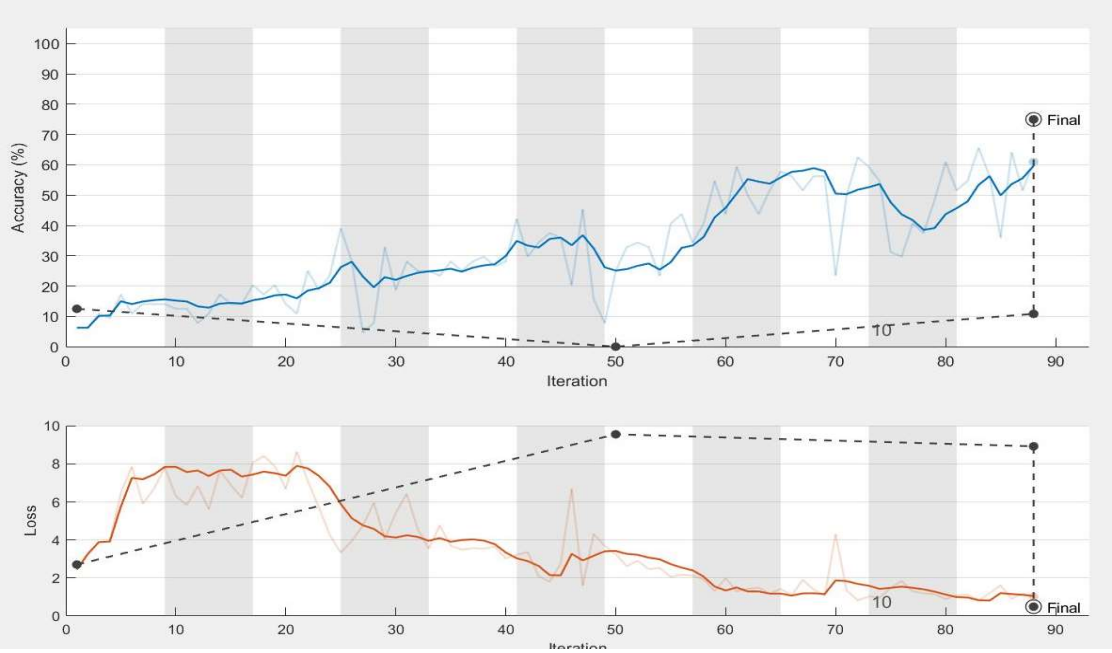

Figure 28. Training accuracy and loss for P400

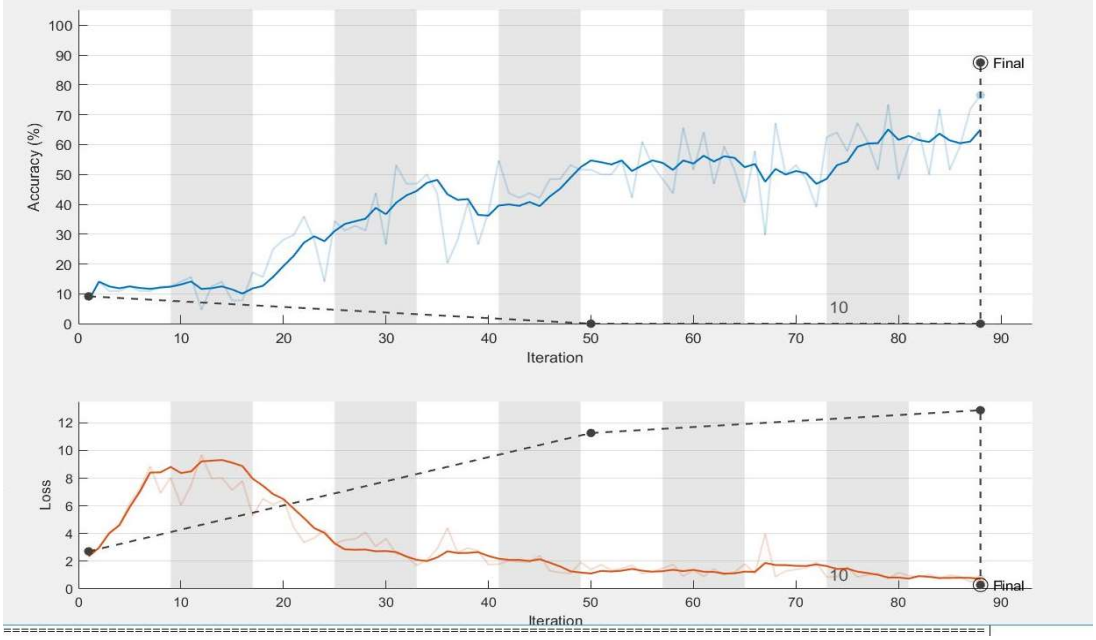

Figure 29. Training accuracy and loss for P600

Table 11 are results of the full-face lattice, the same constrains are applied from Table 8. Each neural network ran for five times, then the mean of the five runs is computed to be the validation accuracy per pore size.

Table 11: Validation Accuracy for full-face input image

Cubic lattice full-face sizes	**Validation Accuracy (%)**
P400	77.5%
P500	55%
P600	65%
P900	62.5%

Compared to Table 10, the lowest validation accuracy is P500. The previous observation of P900 being an outlier may not apply for the full-face imagery, due to P900 and P600 being similar in accuracy. The standard deviation for Table 9 is 9.35 and the overall mean is 65. Figure 30 are two full-face input images, Figures 31 and 32 are training accuracy and loss plots, the respective validation accuracies are 62.5 and 50.

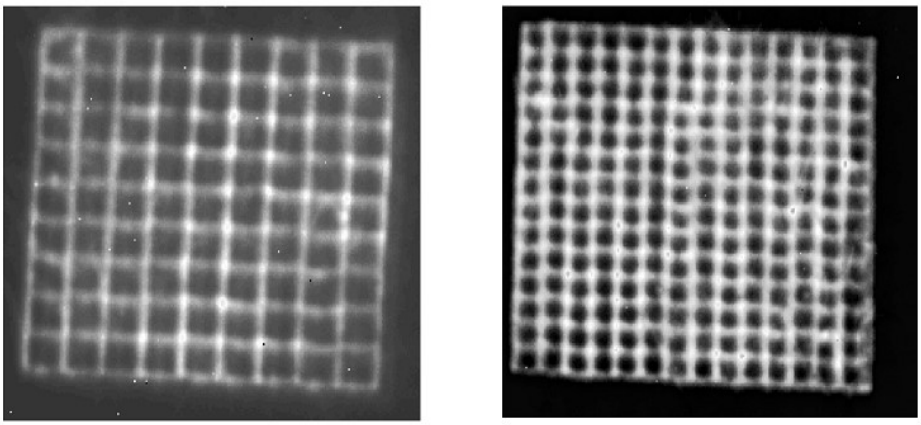

Figure 30. Input full-face image of P900 and P500

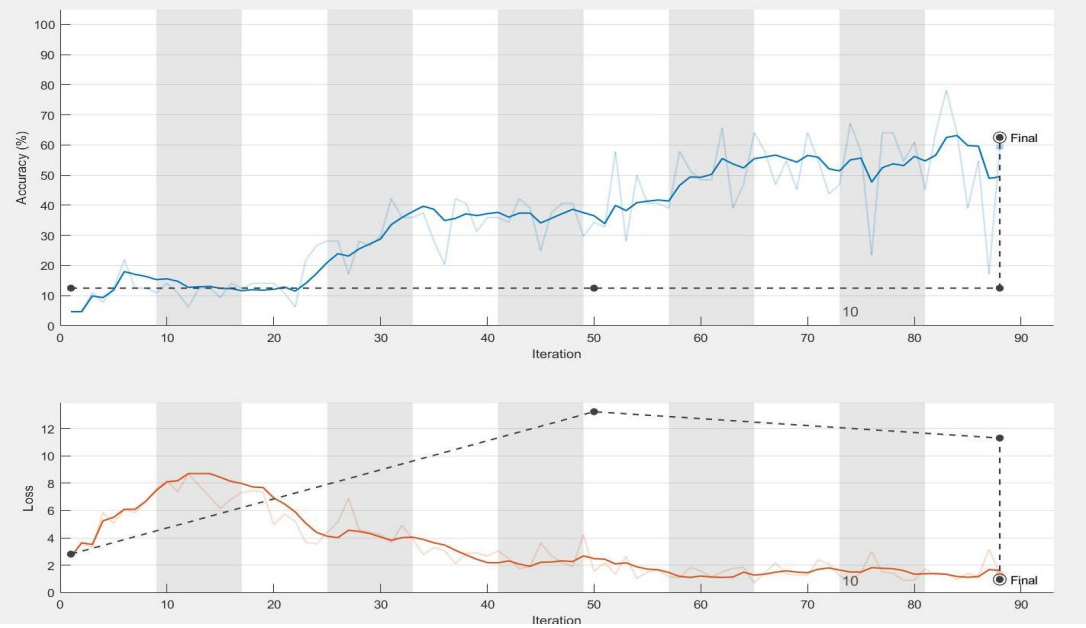

Figure 31. Training accuracy and loss for P600

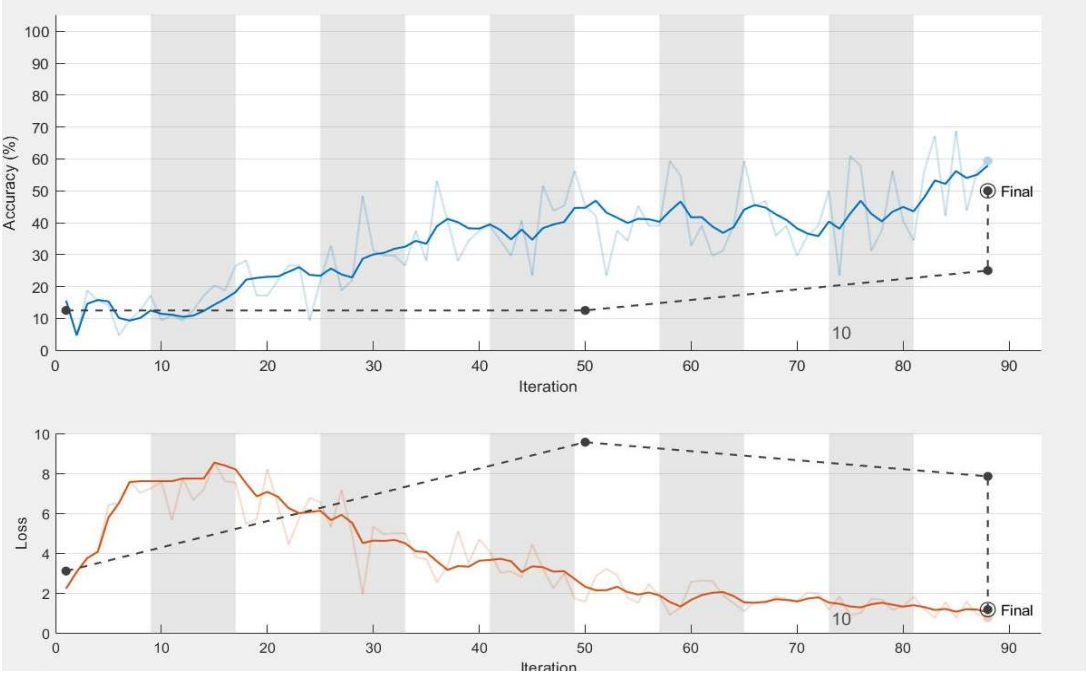

Figure 32. Training accuracy and loss for P500

Taking into consideration of Tables 10 and 11, the validation accuracy for strut images are higher than full-face images. Full-face images contain more noise and more detail, it is possible that with better image processing (i.e. filtering), that the results could be better for the full-face. Any advantages for the full-face would also net towards the strut images. It is also possible that the correlation of a better performing strut imagery will always exist.

8.4.6 Neural Network Overfitting

The CNN presented in this thesis does suffer from occasional overfitting. Neural networks are complex models with numerous hidden layers, the more layers, the more complex the neural network becomes. Essentially, overfitting is when the network is ideal to the training but does not perform well when introduced to new data, such as the validation set. Occasionally, a low validation score will occur, such as 12.5% or 25%. During the early phase of building this CNN, overfitting was more common issue, but it was solved through reducing the training classes to 100 images instead of 200 or 300. Figure 33 is a training accuracy and loss plot of a validation 12.5%.

There are numerous techniques to overcome this overfitting issue, such as L1/L2 Regularization, which monitors and corrects weight values to reduce complexities. Dropout will randomly drop neurons from the network while training is ongoing, essentially making the network smaller. Lastly, early stopping is effective at preventing overfitting, by analyzing when your validation curve begins to drop. When this drop occurs, simply stop the network and analyze what epoch/iteration the neural network drops.

There was an attempt at using all the above techniques but the results for the neural networks were worse than before and overfitting was still an intermittent issue. A future step would be analyzing the training data, reducing or enlarging the data set, or modifying the data augmentation. By inducing more factors of data augmentation, it is possible that the data set will become more "unique" and this overfitting issue will lessen or disappear completely. Another step would be reducing the neural network hidden layers, as there may be excessive complications in the neural network [189-191].

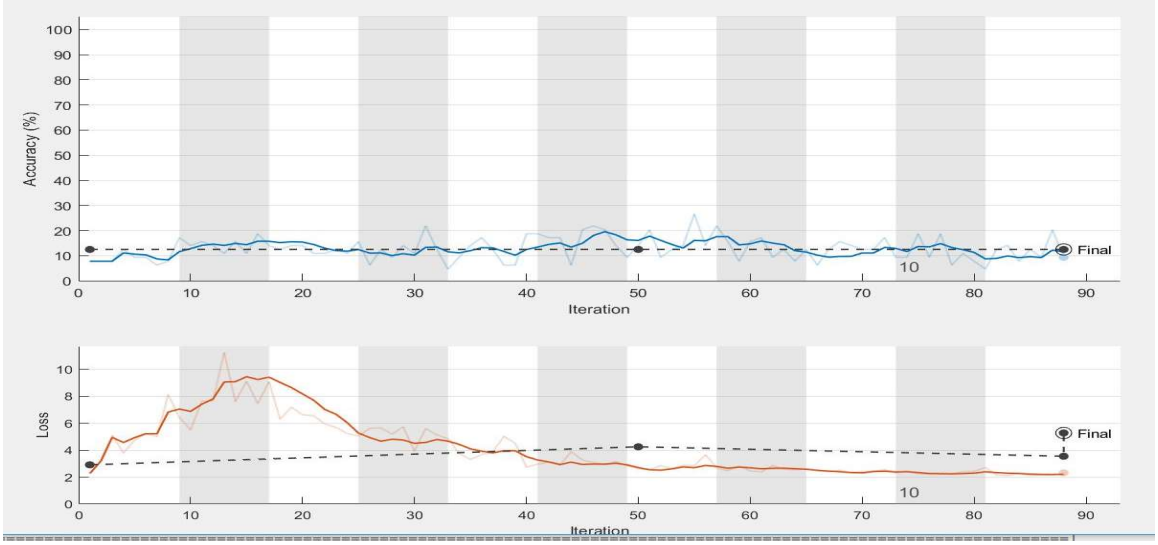

Figure 33. Overfitting of the neural network, resulting in a validation accuracy of 12.5%

CHAPTER 9

CONCLUSION AND FUTURE WORK

9.1 Conclusion

With the growing market of orthopedic implants rising due to a growing elderly population and the growth of countries such as India and China, improved orthopedic implants are needed. With current lattice based orthopedic implants, it is possible to have better implant fixation, service life and mechanical properties than current orthopedic implants. Understanding the osteogenesis process, L-PBF, bone mechanical properties, lattice mechanical properties and biocompatible materials is essential to designing and manufacturing effective metal lattice structures for orthoepic implants.

Referencing various publications, from the literature it was deemed that producing diamond and cubic lattices of pore sizes 400, 500, 600, 900μm would result in good osteointegration and bone mechanical properties. Concerns of manufacturability were addressed, as the lattices were successfully printed in Ti-6Al-4V, with the exception of a defect occurrence for the diamond lattice; caused by a machine error. Due to time limitations, compression and tensile testing were unable to be performed, along with NDE such at SEM and CT-scanning.

A convolutional neural network was created to verify geometries of cubic lattices of various pore sizes. Training the neural network with CAD images via data augmentation was performed. The overall mean validation accuracy is 69% for strut identification and

65% for full-face of the lattice. Improvements were identified in key areas to overcome overfitting and better validation accuracy. Modifications to the DART SLM machine facilitated the development of biomimetic Ti-64Al-4V lattices and the acquisition of *in situ* sensor data. These modifications, as well as the custom AI processing monitoring algorithm to detect and classify build defects, were completed in response to the FDA's recently published guidelines for process validation.

9.2 Future Work

Future work will involve performing compression and tensile material testing on all the pore sizes for diamond and cubic lattices. Performing NDE via CT-Scanning and SEM to identify correct pore sizes and defects in the lattices. The next step would be to cell culture the lattices to identify which lattice structure and pore size promotes the best osseointegration with primary bone cells and osteoblasts. Another possible future work would is FDA stage 1 clinical trial, inserting a part of a lattice in place of bone. Observing how bone will grow into the lattice and testing mechanical adherence of bone to lattice.

The FDA guidelines for process validation are the driving force of this research. As the FDA recommends the use of NDE to validate process monitoring, there are a few techniques we can apply in the future in accordance to these guidelines. NDE such as SEM, CT-scanning and X-ray tomography can be used validate internal geometries and build defects. NDE data can be used to train a neural network, this would only be beneficial to a part that has to be printed multiple times, but a more extensive training dataset would lead to better classification. Other type of *in situ* sensors such as visual camera, high-speed melt

pool, and laser profilometry can also be used to aid neural network training. These sensors all have various advantages and disadvantages, some are better at detecting certain defects than others, where they might be ideal for their own neural network implementation. For example, a high-speed melt pool camera would be ideal for detecting defect occurrence for high/low laser energy power, detecting cracking and balling.

As previously mentioned in Chapter 6, the ideal form of process monitoring is a closed loop feedback that can immediately identify defects and correct machine parameters to prevent the spread of further defects. Although this type of closed loop feedback is years away from implementation, the neural network presented in this thesis is a representation of this control system in terms of defect identification and a representation of process validation for the FDA.

The convolutional neural network should be experimented with techniques to remove overfitting, applying such techniques as L1/L2 regularization, dropout and early stopping. Modification of training data size and other data augmentation techniques can be performed to lessen overfitting and achieve better validation accuracy. MATLAB is also limited on the amount of options and modifications the user can apply to the neural network and training. It is highly recommended that further neural network and deep learning would be transferred to a Python-based workspace. Using Python would open up further customization of the neural network and other deep learning algorithms, such as deep belief networks. MATLAB is an extremely useful tool, but it is evident that MATLAB itself is

still learning how to implement CNN and other deep learning into their suites and toolboxes.

REFERENCES

1. "Wohlers Report 2014," Wohlers Associates, Fort Collins, Colorado, United States, 2014. Accessed: Jan. 2019. [Online]. Available: https://www.wohlersassociates.com/2014report.htm

2. W.S.W. Harun, M.S.I.N. Kamariah, N. Muhamad, S.A.C. Ghani, Faiz Ahmad, Z. Mohamed, "A review of powder additive manufacturing processes for metallic biomaterials," *Powder Tech.*, Dec. 2017. doi: 10.1016/j.powtec.2017.12.058.

3. F. P. Melchels, J. Feijen, D. W. Grijpma, "A review on stereolithography and its applications in biomedical engineering", *Biomaterials*, vol. 31, no. 24, pg. 6121-6130, Aug. 2010. doi: /10.1016/j.biomaterials.2010.04.050.

4. D. Espalin, K. Arcaute, D. Rodriguez, F. Medina, M. Posner, R. Wicker. (2009) Fused deposition modeling of polymethylmethacrylate for use in patient-specific reconstructive surgery. *20th Annu. Int. Solid Freeform Fabrication Symposium.* [Online]. Available: https://www.researchgate.net/publication/287394427_Fused_deposition_modeling_of_polymethylmethacrylate_for_use_in_patient-specific_reconstructive_surgery

5. R. Dhakshyani, Y. Nukman, A. O. N. Azuan. "FDM models and FEA in dysplastic hip," *Rapid Proto. Jol.*, vol. 18, no. 3, pp. 215-221, Jan. 2010. doi: /10.1108/13552541211218144

6. R.K. Quinn, N.R. Armstrong, "Electrochemical and surface analytical characterization of titanium and titanium hydride thin-film electrode oxidation," *J. Electrochem. Soc,.* vol. 125, pp. 1790-1796, 1978. doi: /10.1149/1.2131295.

7. C.N. Elias, J.H.C. Lima, R. Valiev, M.A. Meyers. “Biomedical applications of titanium and its alloys,” *JOM.,* vol. 60, pp. 46-49, Mar. 2008. doi: /10.1007/s11837-008-0031-1.

8. A. Sidambe, “Biocompatibility of Advanced Manufactured Titanium Implants—A Review,” *Materials*, vol. 7, pp. 8168-8188. 2014, doi: 10.3390/ma7128168.

9. Standard Specification for Additive Manufacturing Titanium-6 Aluminum-4 Vanadium ELI with Powder Bed Fusion; ASTM F2924–14; American Society for Testing Materials: West Conshohocken, PA, USA, 2014. [Online]. Available: https://www.astm.org/Standards/F2924.htm

10. Standard Specification for Additive Manufacturing Titanium-6 Aluminum-4 Vanadium ELI (Extra Low Interstitial) with Powder Bed Fusion; ASTM F3001–14; American Society for Testing Materials: West Conshohocken, PA, USA, 2014. [Online]. Available: https://www.astm.org/Standards/F3001.htm

11. W.S.W. Harun, M.S.I.N. Kamariah, Norhamidi Muhamad, S.A.C. Ghani, Faiz Ahmad, Z. Mohamed, “A review of powder additive manufacturing processes for metallic biomaterials,” *Powder Tech.,* Dec. 2017. doi: 10.1016/j.powtec.2017.12.058.

12. A. Dehghan, N. Namdari, M. Behrouz, F. Behzad, “Additive Manufacturing Methods A Brief Overview,” vol. 5, pp. 123-131, Sep. 2018. [Online]. Available:

13. https://www.researchgate.net/publication/327701079_Additive_Manufacturing_Methods_A_Brief_Overview

14. F. A. España, V. K. Balla, S. Bose, A. Bandyopadhyay, “Design and fabrication of CoCrMo alloy based novel structures for load bearing implants using laser engineered

net shaping," *Mat. Sci. and Eng.,* vol. 30, no. 1, pp. 50-57, Jan. 2010, doi: 10.1016/j.msec.2009.08.006.

15. V. K. Balla, A. Bhat, S. Bose, A. Bandyopadhyay, "Laser processed TiN reinforced Ti6Al4V composite coatings," *Jol. of the Mech. Behavior of Biomed. Mat.*, vol. 6, pp. 9-20, Sep. 2011. doi: 10.1016/j.jmbbm.2011.09.007.

16. J. J. Marattukalam *et al.,* "Microstructure and corrosion behavior of laser processed NiTi alloy," *Mat. Sci. and Eng.,* vol. 57, pp. 309-313, Dec. 2015. doi: /10.1016/j.msec.2015.07.067.

17. W.S.W. Harun, M.S.I.N. Kamariah, N. Muhamad, S.A.C. Ghani, F. Ahmad, Z. Mohamed, "A review of powder additive manufacturing processes for metallic biomaterials," *Powder Tech*, vol. 327, pp. 128-151, Mar. 2018. doi: /10.1016/j.powtec.2017.12.058.

18. L. Bochuan, R. Wildman, C. Tuck, I. Ashcroft, R. Hague, "Investigation the effect of particle size distribution on processing parameters optimization in selective laser melting process," *Additive Manufacturing Research Group*, 2011. [Online]. Available: https://www.semanticscholar.org/paper/INVESTIGATION-THE-EFFECT-OF-PARTICLE-SIZE-ON-IN-Liu-Wildman/bbdc5d8e37eaa34cf8f7feec0eaa48b437a57d31

19. A. Spierings, N. Herres, G.Levy, "Influence of the particle size distribution on surface quality and mechanical properties in AM steel part,". *Rapid Proto Jol.,* vol. 17, pp. 195-202, Apr. 2011. doi: /10.1108/13552541111124770.

20. S. A. Yavari *et al.*, "Fatigue behavior of porous biomaterials manufactured using selective laser melting," *Mat. Sci. and Eng.,* vol. 33, no. 8, pp. 4849-4858, 2013. doi: /10.1016/j.msec.2013.08.006.

21. K. Monroy, J. Delgado, J. Ciurana, “Study of the Pore Formation on CoCrMo Alloys by Selective Laser Melting Manufacturing Process,” *Procedia Engineering*, vol. 63, pp. 361-369, 2013. doi: /10.1016/j.proeng.2013.08.227.

22. A. Takaichi *et al.,* “Microstructures and mechanical properties of Co–29Cr–6Mo alloy fabricated by selective laser melting process for dental applications,” *Jol. of the Mech. Behavior of Biomed. Mat.,* vol. 21, pp. 67-76, May. 2013. doi: /10.1016/j.jmbbm.2013.01.021.

23. Y. Wang, Y. Yan, Y. Su, L. Qiao, “Release of metal ions from nano CoCrMo wear debris generated from tribo-corrosion processes in artificial hip implants,” *Jol. of the Mech. Behavior of Biomed. Mat.,* vol. 68, pp. 124-133, Apr. 2017. doi: /10.1016/j.jmbbm.2017.01.041.

24. A. Furqan *et al.,* “Long-term osseointegration of 3D printed CoCr constructs with an interconnected open-pore architecture prepared by electron beam melting,” *Acta Biomaterialia,* vol. 36, pp. 296-309, doi: /10.1016/j.actbio.2016.03.033.

25. K. Hazlehurst, C. J. Wang, M. Stanford, “Evaluation of the stiffness characteristics of square pore CoCrMo cellular structures manufactured using laser melting technology for potential orthopaedic applications,” *Mat & Design,* vol. 51, pp. 949-955, 2013. doi: /10.1016/j.matdes.2013.05.009.

26. Y. S. Hedberg, B. Q., Z. Shen, S. Virtanen, I. O. Wallinder, “In vitro biocompatibility of CoCrMo dental alloys fabricated by selective laser melting,” *Dental Materials*, vol. 30, no. 5, pp. 525-534, May. 2014. doi: /10.1016/j.dental.2014.02.008.

27. Y. Lu *et al.,* "Investigation on the microstructure, mechanical property and corrosion behavior of the selective laser melted CoCrW alloy for dental application," *Mat. Sci. and Eng.,* vol. 49, pp. 517-525, Apr. 2015. doi: /10.1016/j.msec.2015.01.023.

28. L. Zeng, N. Xiang, B. Wei, "A comparison of corrosion resistance of cobalt-chromium-molybdenum metal ceramic alloy fabricated with selective laser melting and traditional processing," *The Journal of Prosthetic Dentistry*, vol. 112, no. 5, pp. 1217-1224, Nov. 2014. doi: /10.1016/j.prosdent.2014.03.018.

29. A. Aherwar, A. K. Singh, A. Patnaik, "Current and Future Biocompatibility Aspects of Biomaterials for Hip Prosthesis," vol. 3 no. 1, pp. 23-43, Dec. 2015. doi: /10.3934/bioeng.2016.1.23

30. R.I.M. Asri, W.S.W. Harun, M. Samykano, N.A.C. Lah, S.A.C. Ghani, F. Tarlochan, M.R. Raza, "Corrosion and surface modification on biocompatible metals: A review," *Mat Sci and Eng.,* Vol. 77, pp. 1261-1274, Aug. 2017. doi: /10.1016/j.msec.2017.04.102.

31. T.M. Sridhar, U. K. Mudali, M. Subbaiyan, "Preparation and characterisation of electrophoretically deposited hydroxyapatite coatings on type 316L stainless steel", *Corros. Sci*. vol. 45, no. 2, pp. 237–252, doi: /10.1016/S0010-938X(02)00091-4.

32. C. García, S. Ceré, A. Durán, "Bioactive coatings prepared by sol–gel on stainless steel 316L," *J. Non-Cryst. Solids*, vol. 348, pp. 218-224, Nov. 2004. doi: /10.1016/j.jnoncrysol.2004.08.172.

33. L. Rännar, A. Koptyug, J. Olsén, K. Saeidi, Z. Shen, "Hierarchical structures of stainless steel 316L manufactured by Electron Beam Melting," *Additive Manufacturing*, vol 17, pp. 106-112, Oct. 2017. doi: /10.1016/j.addma.2017.07.003.

34. F. Xie, X. He, S. Cao, X. Qu, “Structural andmechanical characteristics of porous 316L stainless steel fabricated by indirect selective laser sintering,” *J. Mater. Process. Technol*. Vol. 213, no. 6, pp. 838–843, June. 2013. doi: /10.1016/j.jmatprotec.2012.12.014.

35. M.M. Dewidar, K.A. Khalil, J.K. Lim, “Processing and mechanical properties of porous 316L stainless steel for biomedical applications,” *Trans. Nonferrous Metals Soc. China,* vol. 17, no. 13, pp. 468-473, June. 2007. doi: /10.1016/S1003-6326(07)60117-4.

36. I. Shishkovsky, Y. Morozov, I. Smurov, “Nanofractal surface structure under laser sintering of titanium and nitinol for bone tissue engineering,” *Appl. Surf. Sci.* vol. 254, no. 4, pp. 1145–1149, Dec. 2007. doi: /10.1016/j.apsusc.2007.09.021.

37. W. Haider, “Enhanced biocompatibility of NiTi (Nitinol) via surface treatment and alloying,” Ph.D dissertation, Dept. Mech. Eng., Flordia Int. Univ., Miami., Fl., 2010. doi: /10.25148/etd.FI10041612

38. J. W. Mwangi *et al.*, “Nitinol manufacturing and micromachining: A review of processes and their suitability in processing medical-grade nitinol, *Jol. of Manuf. Proc*., vol. 38, pp. 355-369, Feb. 2019. doi: /10.1016/j.jmapro.2019.01.003.

39. T. Habijan *et al.*, “The biocompatibility of dense and porous Nickel–Titanium produced by selective laser melting,” *Mat. Sci. and Eng.,* vol. 33, no. 1, pp. 419-426, Jan. 2013. doi: /10.1016/j.msec.2012.09.008.

40. Vincent Leermiddelen Scientific, “NITINOL (SHAPE MEMORY ALLOY) SPOOL 0,15MM 10 METER,” *Vincent Leermiddelen Scientific*, 2019. [Online]. Available: http://www.leermiddelen.be/en/nitinol--shape-memory-alloy-spool-015mm-10-meter [Accessed: Feb. 2019].

41. P. Ghosal, M. C. Majumder, A. Chattopadhyay, “Study on direct laser metal deposition,” *Mat. Today: Proceedings,* vol. 5, no. 5, pp. 12509-12518, 2018. doi: /10.1016/j.matpr.2018.02.232.

42. Kamardeen O. Abdulrahman, Esther T. Akinlabi, Rasheedat M. Mahamood, Sisa Pityana, Monnamme Tlotleng, “Laser Metal Deposition of Titanium Aluminide Composites: A Review,” *Mat. Today: Proceedings,* vol. 5, no. 9, pp. 19738-19746 2018. doi: /10.1016/j.matpr.2018.06.336.

43. H. Xu, *et al., “*Investigation of gum metal coating on Ti6Al4V plate by direct laser deposition,” *Surface and Coatings Tech*., vol. 363, pp. 161-169, doi: /10.1016/j.surfcoat.2019.01.086.

44. R. Negrea, *et al.,* “Akermanite-based coatings grown by pulsed laser deposition for metallic implants employed in orthopaedics,” *Surface and Coatings Tech.,* vol. 357, pp. 1015-1026, Jan. 2018. doi: /10.1016/j.surfcoat.2018.11.008.

45. F. Xie, X. He, S. Cao, M. Mei, X. Qu, “Influence of pore characteristics on microstructure, mechanical properties and corrosion resistance of selective laser sintered porous Ti–Mo alloys for biomedical applications,” *Electrochimica Acta,* vol. 105, pp. 121-129. Aug. 2013. doi: /10.1016/j.electacta.2013.04.105.

46. F. Xie, X. He, S. Cao, X. Qu, “Structural and mechanical characteristics of porous 316L stainless steel fabricated by indirect selective laser sintering,” *Jol. of Mat. Processing Tech*., vol. 213, no. 6, pp. 838-843, June. 2013. doi: /10.1016/j.jmatprotec.2012.12.014.

47. H. Zhang, S. LeBlanc, “Processing Parameters for Selective Laser Sintering or Melting of Oxide Ceramics,” *Additive Manufacturing of High-performance Metals and Alloys,* July. 2018. doi: /10.5772/intechopen.75832.

48. A. Cerardi, M. Caneri, R. Meneghello, G. Concheri, M. Ricotta, “Mechanical characterization of polyamide cellular structures fabricated using selective laser sintering technologies,” *Mater. & Des.* vol. 46, pp. 910–915. doi: /10.1016/j.matdes.2012.11.042.

49. F. Mangano *et al.,* “ Custom-made, selective laser sintering (SLS) blade implants as a non-conventional solution for the prosthetic rehabilitation of extremely atrophied posterior mandible,” vol. 28, no. 5, pp. 1241-1247, Sep. 2012. doi: /10.1007/s10103-012-1205-1.

50. F. Liu, R. Lee, W. Lin, Y. Liao, “Selective Laser Sintering of Bio-Metal Scaffold,” *Procedia CIRP,* vol. 5, pp. 83-87. 2013. doi: /10.1016/j.procir.2013.01.017.

51. Rapid Prototyping Services Canada,” Selective Laser Sintering,” *Rapid Prototyping Services Canada,* [Online]. Available: http://rapidprototypingservicescanada.com/selective-laser-sintering-sls.php [Accessed: Feb. 2019].

52. L. Mullen, R. C. Stamp, W. K. Brooks, E. Jones, C. J. Sutcliffe, “Selective laser melting: A unit cell approach for the manufacture of porous, titanium, bone in-growth constructs, suitable for orthopedic applications,” *J. Biomed. Mater. Res.,* vol. 92 no. 2, pp. 178-188, May. 2009. doi: /10.1002/jbm.b.31219.

53. X.Z. Xin, N. Xiang, J. Chen, B. Wei, “In vitro biocompatibility of Co–Cr alloy fabricated by selective laser melting or traditional casting techniques,” *Mat. Letters*, vol. 88, pp. 101-103, Dec. 2012. doi: /10.1016/j.matlet.2012.08.032.

54. A. Fukuda *et al.*, “Osteoinduction of porous Ti implants with a channel structure fabricated by selective laser melting,” *Acta Biomaterialia*, vol. 7, no. 5, pp. 2327-2336, May. 2011. doi: /10.1016/j.actbio.2011.01.037.

55. S. V. Bael *et al.,* “The effect of pore geometry on the in vitro biological behavior of human periosteum-derived cells seeded on selective laser-melted Ti6Al4V bone scaffolds,” *Acta Biomaterialia*, vol. 8, no. 7, pp. 2824-2834. July. 2012. doi: /10.1016/j.actbio.2012.04.001.

56. M. Salmi *et al.,* "Patient-specific reconstruction with 3D modeling and DMLS additive manufacturing," *Rapid Proto. Jol.,* vol. 18 no. 3, pp. 209-214, 2012. doi: /10.1108/13552541211218126.

57. I. A.J. van Hengel *et al.,* “Selective laser melting porous metallic implants with immobilized silver nanoparticles kill and prevent biofilm formation by methicillin-resistant Staphylococcus aureus,” *Biomaterials,* vol. 140, pp. 1-15, Sep. 2017. doi: /10.1016/j.biomaterials.2017.02.030.

58. X. Pei *et al.,* “Bionic mechanical design of titanium bone tissue implants and 3D printing manufacture,” *Mat Letters,* vol. 208, pp. 133-137, 2017. doi: /10.1016/j.matlet.2017.04.128.

59. M. Shellabear, O. Nyrhilä, (2004). “DMLS-Development history and state of the art.” Proc. of the 4th LANE 2004. [Online]. Available: https://www.i3dmfg.com/wp-content/uploads/2015/07/History-of-DMLS.pdf

60. X.Z. Zhang, M. Leary, H.P. Tang, T. Song, M. Qian, “Selective electron beam manufactured Ti-6Al-4V lattice structures for orthopedic implant applications: Current

status and outstanding challenges," *Current Opinion in Solid State and Mat Sci*, vol. 22, no. 3, pp. 75-99, June. 2018. doi: /10.1016/j.cossms.2018.05.002.

61. L. Shujun, "Fabrication of open-cellular (porous) titanium alloy implants: osseointegration, vascularization and preliminary human trials," *Sci. China Mat.,* vol. 61, no. 4, pp. 525-536, April 2018. doi: /10.1007/s40843-017-9063-6.

62. J, Markhoff, J. Wieding, V. Weissmann J. Pasold, A. Jonitz-Heincke, R. Bader, "Influence of Different Three-Dimensional Open Porous Titanium Scaffold Designs on Human Osteoblasts Behavior in Static and Dynamic Cell Investigations," *Materials (Basel)*, vol. 8, no. 8, pp.5490–5507, Aug. 2015. doi: /10.3390/ma8085259.

63. J. Parthasarathy, B. Starly, S. Raman, A. Christensen, "Mechanical evaluation of porous titanium (Ti6Al4V) structures with electron beam melting (EBM)," *J. Mech. Behav. Biomed. Mater.* vol. 3, no. 3, pp. 249–259, April. 2010. doi: /10.1016/j.jmbbm.2009.10.006.

64. A. Mazzoli, M. Germani, R. Raffaeli, "Direct fabrication through electron beam melting technology of custom cranial implants designed in a PHANToM-based haptic environment," *Mater. Des.*, vol. 30, no.8, pp. 3186–3192, Sep. 2009. doi: /10.1016/j.matdes.2008.11.013.

65. L.E. Murr *et al.,* "Characterization of Ti–6Al–4V open cellular foams fabricated by additive manufacturing using electron beam melting," *Mater. Sci. Eng. A,* vol. 527, no. 7-8, pp. 1861–1868, 2010. doi: /10.1016/j.msea.2009.11.015.

66. P. Heinl, L. Müller, C. Körner, R. F. Singer, F. A. Müller, "Cellular Ti–6Al–4V structures with interconnected macro porosity for bone implants fabricated by selective

electron beam melting," *Acta Biomaterialia,* vol. 4, no. 5, pp. 1536-1544, Sep. 2008. doi: /10.1016/j.actbio.2008.03.013.

67. C.M. Haslauer, J.C. Springer, O.L.A. Harrysson, E.G. Loboa, N.A. Monteiro-Riviere, D.J. Marcellin-Little, "In vitro biocompatibility of titanium alloy discs made using direct metal fabrication," *Med. Eng. Phys.* vol. 32, no. 6, pp. 645–652, July. 2010. doi: /10.1016/j.medengphy.2010.04.003.

68. C.J. Smith, F. Derguti, E. Hernandez Nava, M. Thomas, S. Tammas-Williams, S. Gulizia, D. Fraser, I. Todd, "Dimensional accuracy of Electron Beam Melting (EBM) additive manufacture with regard to weight optimized truss structures," Jol. of Mat. Processing Tech., Vol. 229, pp. 128-138, Mar. 2016. doi: /10.1016/j.jmatprotec.2015.08.028.

69. B. Wysocki, P. Maj, R. Sitek, J. Buhagiar, K. J. Kurzydłowski, W. Święszkowski, "Laser and Electron Beam Additive Manufacturing Methods of Fabricating Titanium Bone Implants," *Applied Sciences.* vol. 7, no. 7, June. 2017. doi: /10.3390/app7070657.

70. S.A. Hacking *et al.*, "Surface roughness enhances the osseointegration of titanium headposts in non-human primates," *Jol of Neurosci. Meth.,* vol. 211, no. 2, 2012, pp. 237-244, Nov. 2012. doi: /10.1016/j.jneumeth.2012.09.002.

71. F. Rupp, L. Liang, J. Geis-Gerstorfer, L. Scheideler, F. Hüttig, "Surface characteristics of dental implants: A review," *Dent. Mat.,* vol. 34, no. 1, pp. 40-57, Jan. 2018. doi: /10.1016/j.dental.2017.09.007.

72. G. Zhao, A.L. Raines, M. Wieland, Z. Schwartz, B.D. Boyan, "Requirement for both micron- and submicron scale structure for synergistic responses of osteoblasts to

substrate surface energy and topography," *Biomaterials,* vol. 28, no. 18, pp. 2821-2829, 2007. doi: /10.1016/j.biomaterials.2007.02.024.

73. M. de Wild *et al.,* "Bone regeneration by the osteoconductivity of porous titanium implants manufactured by selective laser melting: A histological and micro computed tomography study in the rabbit," *Tissue Eng. Part A,* vol. 19, no. 23-24, pp. 2645-2654, Sep. 2013. doi: 10.1089/ten.TEA.2012.0753.

74. P. Wang, W. J. Sin, M. L. S. Nai, J. Wei, "Effects of Processing Parameters on Surface Roughness of Additive Manufactured Ti-6Al-4V via Electron Beam Melting," *Materials (Basel)*. vol. 10 no.10, Sep. 2017. doi: /10.3390/ma10101121.

75. Z. Sun, X. Tan, S.B. Tor, W.Y. Yeong, "Selective laser melting of stainless steel 316L with low porosity and high build rates," *Mater. Des*., vol. 104, pp. 197–204, Aug. 2016. doi: /10.1016/j.matdes.2016.05.035.

76. I. Drstvensek, N.I. Hren, T. Strojnik, "Application of rapid prototyping in craniomaxillofacial surgery procedures," *Int. J. Biol. Biomed. Eng*. vol. 1, no.2, pp. 29–38, 2008.

77. General Electric, "Electron Beam Melting (EBM)," *GE Additive,* [Online]. Available: https://www.ge.com/additive/additive-manufacturing/information/electron-beam-melting-technology [Accessed: Feb. 2019].

78. P. K. Gokuldoss, S. Kolla, J. Eckert, "Additive Manufacturing Processes: Selective Laser Melting, Electron Beam Melting and Binder Jetting-Selection Guidelines," vol. 10, no. 6, Jun. 2017. doi: /10.3390/ma10060672.

79. Y. Pengpeng, G. Dongdong, “Molten pool behaviour and its physical mechanism during selective laser melting of TiC/AlSi10Mg nanocomposites: simulation and experiments,”

80. *Jol. of Phys. D: Applied Phys.,* vol. 48, no. 3, Jan. 2015. doi: 10.1088/0022-3727/48/3/035303.

81. A. Sidambe, “Biocompatibility of Advanced Manufactured Titanium Implants—A Review,” *Mats*., vol. 7, no. 12, pp. 8168-8188, Dec. 2014. doi: /10.3390/ma7128168.

82. CK-12, “Unit Cells,” *CK-12 Foundation,* [Online]. Available: https://www.ck12.org/c/chemistry/unit-cells/lesson/Unit-Cells-CHEM/?referrer=concept_details [Accessed: Feb. 2019].

83. Y. Chunze, H. Liang, H. Ahmed, R. David, “Evaluations of cellular lattice structures manufactured using selective laser melting,” *Int. Jol of Mach. Tools and Manuf.,* vol. 62, pp. 32-38, Nov. 2012. doi: /10.1016/j.ijmachtools.2012.06.002.

84. Y. Chunze, H. Liang, H. Ahmed, Y. Philippe, R. David, “Advanced lightweight 316L stainless steel cellular lattice structures fabricated via selective laser melting,” *Mat & Design,* vol. 55, pp. 533-541, Mar. 2014. doi: /10.1016/j.matdes.2013.10.027.

85. Y. Tang, G. Dong, Q. Zhou and Y. F. Zhao, "Lattice Structure Design and Optimization With Additive Manufacturing Constraints*," IEEE Transactions on Automation Science and Engineering*, vol. 15, no. 4, pp. 1546-1562, Oct. 2018. doi: /10.1109/TASE.2017.2685643.

86. A. Yánez, A. Cuadrado, O. Martel, H. Afonso, D. Monopoli, “Gyroid porous titanium structures: A versatile solution to be used as scaffolds in bone defect

reconstruction," *Mat. & Design,* vol. 140, pp. 21-29, Feb. 2018. doi: /10.1016/j.matdes.2017.11.050.

87. S.J. Li *et al.,* "Compression fatigue behavior of Ti–6Al–4V mesh arrays fabricated by electron beam melting," *Acta Materialia*, vol. 60, no. 3, pp. 793-802, Feb. 2012. doi: /10.1016/j.actamat.2011.10.051.

88. W. Xiaojian *et al.,* "Topological design and additive manufacturing of porous metals for bone scaffolds and orthopaedic implants: A review," *Biomaterials*, vol. 83, Mar. 2016. doi: /10.1016/j.biomaterials.2016.01.012.

89. S. L. Sing, J. An, W. Y. Yeong, F. E. Wiria, "Laser and electron-beam powder-bed additive manufacturing of metallic implants: A review on processes, materials and designs," J. *Orthop. Res.* vol. 34, no. 3, pp. 369-385, doi:10.1002/jor.23075.

90. L. E. Murr, "Strategies for creating living, additively manufactured, open-cellular metal and alloy implants by promoting osseointegration, osteoinduction and vascularization: An overview," *Jol. of Mat. Sci. & Tech.,* vol. 35, no. 2, pp. 231-241, Feb. 2019. doi: /10.1016/j.jmst.2018.09.003.

91. M. Ridzwan, S. Shuib, A. Y. Hassan, A. A. Shokri, M. Ibrahim, "Problem of Stress Shielding and Improvement to the Hip Implant Designs: A Review," Jol. of Med. Sci. vol. 7, Mar. 2007. doi: /10.3923/jms.2007.460.467.

92. J. Rho, L. Kuhn-Spearing, P. Zioupos, "Mechanical properties and the hierarchical structure of bone," Med. Eng. & Phys., vol. 20, no. 2, pp. 92-102, Apr. 1998. doi: / 10.1016/S1350-4533(98)00007-1.

93. Y. Li, C. Yang, H. Zhao, S. Qu, X. Li, Y Li, “New Developments of Ti-Based Alloys for Biomedical Applications,” *Mats. (Basel),* vol. 7, no. 3, pp. 1709-1800, Mar. 2014. doi: /10.3390/ma7031709

94. F. G. Evans, “Mechanical properties and histology of cortical bone from younger and older men,” vol. 185, no. 1, pp. 1-11, May. 1976. doi: /10.1002/ar.1091850102.

95. O. Lindahl. A. G. H. Lindgren, “Cortical Bone in Man 1. Variation of the Amount and Density with Age and Sex,” *Acta Orthopaedica Scandinavica,* vol. 38, no. 1-4, pp. 133-140, Jun. 1967. doi: /10.3109/17453676708989627.

96. O. Lindahl. A. G. H. Lindgren, “Cortical Bone in Man II. Variation of the Amount and Density with Age and Sex,” *Acta Orthopaedica Scandinavica,* vol. 38, no. 1-4, pp. 141-147, Jun. 1967. doi: /10.3109/17453676708989628.

97. A. H. Burstein, D. T. Reilly, M. Martens, “Aging of bone tissue: mechanical properties,” *J Bone Joint Surg Am.* vol. 58, no. 1, pp. 82-86, Jan. 1976. doi: /10.2106/00004623-197658010-00015.

98. O. Lindahl, “Mechanical Properties of Dried Defatted Spongy Bone*,” Acta Orthopaedica Scandinavica,* vol. 47, no. 1, pp. 11-19, Mar. 1976. doi: /10.3109/17453677608998966.

99. M. Ding, M. Dalstra, C. Danielsen, J. Kabel, I. Hvid, F. Linde, “Age variations in the properties of human tibial trabecular bone,” *The Jol. of Bone and Joint Surgery. Brit vol.,* vo. 79, pp. 995-1002, doi: /10.1302/0301-620X.79B6.0790995.

100. F. Linde, I. Hvid, B. Pongsoipetch, “Energy absorptive properties of human trabecular bone specimens during axial compression.” *J. Orthop. Res.,* vol. 7, no. 3, pp. 432-439, doi: /10.1002/jor.1100070316.

101. A. Rohlmann, H. Zilch, G. Bergmann, R. Kolbel, “Material properties of femoral cancellous bone in axial loading,” *Arch. Orth. Traum. Surg.* vol. 97, no. 2, pp. 95-102, Sep. 1980. doi: /10.1007/BF00450930.

102. L. Mosekilde, L. Mosekilde, C.C. Danielsen, “Biomechanical competence of vertebral trabecular bone in relation to ash density and age in normal individuals”, *Bone*, vol. 8, no. 2, pp. 79-85, 1987. doi: /10.1016/8756-3282(87)90074-3.

103. T. H. Hansson, T. S. Keller, M. M. Panjabi, “A Study of the Compressive Properties of Lumbar Vertebral Trabeculae: Effects of Tissue Characteristics,” *Spine.,.* vol. 12, no. 1, pp. 56-62, doi: /10.1097/00007632-198701000-00011.

104. S. Pal, “Mechanical Properties of Biological Materials,” in *Design of Artificial Human Joints & Organs*, Boston, MA, USA: Springer, 2014, pp. 23-40.

105. *Ti6Al4V ELITitanium Alloy,* Acram AB, [Online]. Available: http://www.arcam.com/wp-content/uploads/Arcam-Ti6Al4V-ELI-Titanium-Alloy.pdf

106. P. Krakhmalev, G. Fredriksson, I. Yadroitsava, N. Kazantseva, A. du Plessis, I. Yadroitsev, “Deformation Behavior and Microstructure of Ti6Al4V Manufactured by SLM,” *Phys. Procedia,* vol. 83, pp. 778-788, 2016. doi: /10.1016/j.phpro.2016.08.080.

107. L. Facchini, E. Magalini, P. Robotti, A. Molinari, S. Hoges, K. Wissenbach, “Ductility of a Ti-6Al-4V alloy produced by selective laser melting of prealloyed powders,” *Rapid Proto. Jol,* vol. 16, no. 6, pp. 450-459, 2010. doi: /10.1108/13552541011083371.

108. M. Frey, M. Shellabear, L. Thorsson, “Mechanical testing of DMLS parts,”, *EOS GmbH Electro Opt. Sys.* 2019. [Online]. Available: https://www.i3dmfg.com/wp-content/uploads/2015/06/Whitepaper-Mechanical-Testing-of-DMLS-Parts.pdf

109. H. K. Rafi, N. V. Karthik, H. Gong, T. L. Starr, B. E. Stucker,” Microstructures and mechanical properties of Ti6Al4V parts fabricated by selective laser melting and electron beam melting,” *Jol. of Mat. Eng. and Perf.,* vol. 22, no. 12, pp. 3873-3883, Aug. 2013. doi: /10.1007/s11665-013-0658-0

110. L.E. Murr *et al.,* “Microstructure and mechanical behavior of Ti-6Al-4V produced by rapid-layer manufacturing, for biomedical applications,” *Jol, of the Mech. Behavior of Biomed. Mat,* vol. 2, no. 1, pp. 20-32, Jan. 2009. doi: /10.1016/j.jmbbm.2008.05.004.

111. A. Mertens *et al.,*” Mechanical properties of alloy Ti–6Al–4V and of stainless steel 316L processed by selective laser melting: influence of out-of-equilibrium microstructures,” *Powder Metallurgy,* vol. 57, no. 3, pp. 184-189, Jul. 2014. doi: /10.1179/1743290114Y.0000000092.

112. Standard Specification for Titanium-6Aluminum-4Vanadium Alloy Castings for Surgical Implants, F1108-14, ASTM; ASTM F1108; West Conshohocken, PA, USA, 2014. [Online]. Available: https://www.astm.org/Standards/F1108.htm

113. I. Polozov, V. Sufiiarov, E. Borisov, A. Popovich, D. Masaylo, “Producing hip implants of titanium alloys by additive manufacturing,” *Int. Jol. of Bioprinting,* vol. 2, pp. 78-84, doi: /10.18063/IJB.2016.02.004.

114. S. L. Sing, J. An, W. Y. Yeong, F. E. Wiria, “Laser and electron-beam powder-bed additive manufacturing of metallic implants: A review on processes, materials

and designs," J. *Orthop. Res.,* vol. 34, pp. 369-385, Oct. 2015. doi: /10.1002/jor.23075.

115. B. Vandenbroucke, J. Kruth, "Selective laser melting of biocompatible metals for rapid manufacturing of medical parts," *Rapid Proto. Jol.* vol. 13, no. 4, pp. 196–203, doi: /10.1108/13552540710776142.

116. L. E. Murr *et al.,* "Microstructures and mechanical properties of electron beam-rapid manufactured Ti-6Al-4V biomedical prototypes compared to wrought Ti-6Al-4V," *Mats Characterization,* vol. 60, no. 2, pp. 96–105, Feb. 2009. doi: /10.1016/j.matchar.2008.07.006.

117. W. F. Ho, "A comparison of tensile properties and corrosion behavior of cast Ti–7.5Mo with c.p. Ti, Ti–15Mo and Ti–6Al–4V alloys," *Jol. of Alloys and Comp.,* vol. 464, no. 1–2, pp. 580-583, Sep. 2008. doi: /10.1016/j.jallcom.2007.10.054.

118. Z. J. Wei, L. Cao, H. W. Wang, C. Zou, "Microstructure and mechanical properties of TiC/Ti-6Al-4V composites processed by in situ casting route," *Mat. Sci. and Tech.,* vol. 27, no. 8, pp. 1321-1327, doi: /10.1179/026708310X12699498462922.

119. G. M. Bilgin, "Optimization of the mechanical properties of Ti-6Al-4V alloy produced by three dimensional additive manufacturing using thermochemical processes," M.S. thesis, Dept. Metal. & Mat. Eng., Middle East Tech. Univ, Ankara, Turkey, 2017. [Online]. Available: http://etd.lib.metu.edu.tr/upload/12620708/index.pdf

120. M. Losertova, V. Kubeš, "Microstructure and mechanical properties of selective laser melted Ti6Al4V alloy*," IOP Conf. Series: Mat. Sci. and Eng.,* Nov. 2017. doi: /10.1088/1757-899X/266/1/012009.

121. R. Fadida, D. Rittel, A. Shirizly, "Dynamic Mechanical Behavior of Additively Manufactured Ti6Al4V With Controlled Voids," *Jol. of Applied Mech*., vol. 82, no. 4, Apr. 2015. doi: /10.1115/1.4029745.

122. S. C. Cowin, "Mechanics of Materials" in *Bone Mechanics Handbook*, 2nd ed. Boca Raton, FL, USA, CRC Press, 2003.

123. M. Ridzwan, S. Shuib, A.Y, Hassan, A. A. Shokri, M. Ibrahim, "Problem of Stress Shielding and Improvement to the Hip Implant Designs: A Review," *Jol of Med. Sci,* vol. 7, no. 3, Mar. 2017. doi: /10.3923/jms.2007.460.467.

124. H. Choo *et al.,* "Effect of laser power on defect, texture, and microstructure of a laser powder bed fusion processed 316L stainless steel," *Mat & Design,* vol. 164, Feb. 2019. doi: /10.1016/j.matdes.2018.12.006.

125. L. Scime, J. Beuth, "A multi-scale convolutional neural network for autonomous anomaly detection and classification in a laser powder bed fusion additive manufacturing process," *Ad. Manuf.,* vol. 24, pp. 273-286, doi: /10.1016/j.addma.2018.09.034.

126. A.J. Dunbar, E.R. Denlinger, J. Heigel, P. Michaleris, P. Guerrier, R. Martukanitz, T.W. Simpson, "Development of experimental method for in situ distortion and temperature measurements during the laser powder bed fusion additive manufacturing process," *Ad. Manuf.,* vol. 12, pp. 25-30. Oct. 2016. doi: /10.1016/j.addma.2016.04.007.

127. S. Tammas-Williams, P.J. Withers, I. Todd, P.B. Prangnell, “The effectiveness of hot isostatic pressing for closing porosity in titanium parts manufactured by selective electron beam melting,” *Metall. Mater. Trans.,* vol. 47, no. 5, pp. 1939–1946, Mar. 2016. doi: /10.1007/s11661-016-3429-3.

128. C. Qiu, N. J.E. Adkins, M. M. Attallah, “Microstructure and tensile properties of selectively laser-melted and of HIPed laser-melted Ti–6Al–4V,” *Mat. Sci. and Eng.: A*, vol. 578, pp. 230-239, Aug. 2013. doi: /10.1016/j.msea.2013.04.099.

129. S. Zhao, S.J. Li, W.T. Hou, Y.L. Hao, R. Yang, R.D.K. Misra, “The influence of cell morphology on the compressive fatigue behavior of Ti-6Al-4V meshes fabricated by electron beam melting,” *Jol. of the Mech. Behv. of Biomed. Mat.,* vol. 59, pp. 251-264, June. 2016. doi: /10.1016/j.jmbbm.2016.01.034.

130. J. Parthasarathy, B. Starly, S. Raman, “A design for the additive manufacture of functionally graded porous structures with tailored mechanical properties for biomedical applications,” *Jol. of Manuf. Proc.,* vol. 13, no. 2, pp. 160-170, Aug. 2011. doi: /10.1016/j.jmapro.2011.01.004.

131. X. Li, Y. Luo, C. Wang, “Preparation and characterization of porous Ti6Al4V/alginate hybrid implant by combination of electron beam melting and freeze-drying,” *Mat. Letters,* vol. 81 pp. 23-26, Aug. 2012. doi: /10.1016/j.matlet.2012.04.151.

132. W. van Grunsven, E. Hernandez-Nava, G C. Reilly, R. Goodall, “Fabrication and Mechanical Characterisation of Titanium Lattices with Graded Porosity.” *Metals*, vol. 4, no. 3, pp. 401-409, Sep. 2014. doi: /10.3390/met4030401.

133. N. W. Hrabe,, P. Heinl, B. Flinn, C. Körner, R. K. Bordia, "Compression-compression fatigue of selective electron beam melted cellular titanium (Ti-6Al-4V)," *J. Biomed. Mater. Res.,* vol. 99, no. 2, pp. 313-20, Nov. 2011. doi: /10.1002/jbm.b.31901.

134. P. Heinl, C. Körner, R. Singer, "Selective Electron Beam Melting of Cellular Titanium: Mechanical Properties," *Adv. Eng. Mater.,* vol. 10, no. 9, pp. 882-888, Aug. 2008. doi: /10.1002/adem.200800137.

135. G. Bergmann, A. Bender, F. Graichen, J. Dymke, A. Rohlmann, A. Trepczynski, M. O. Heller, I. Kutzner: "Standardized Loads Acting in Knee Implants," *PLoS One,* vol. 9, no. 1, Jan. 2014. doi: 10.1371/journal.pone.0086035.

136. Dentsply Sirona Implants Global, Cell-to-Cell Communication – Osseointegration. (Jan. 5, 2015) Accessed: Feb. 20, 2019. [Online Video]. Available: https://www.youtube.com/watch?v=j4K4sZ4eg-8

137. H. Terheyden, N. P. Lang, S. Bierbaum, B. Stadlinger, "Osseointegration—Communication of cell," Clinical oral implants research. vol. 23, no. 10, pp. 1127-35, Nov. 2011. doi: /10.1111/j.1600-0501.2011.02327.x

138. J. B. Park, "Orthopedic prosthesis fixation," *Ann. Biomed. Eng.,* vol. 20, no. 6, pp. 583-94, 1992. doi: /10.1007/BF02368607.

139. M. Nysted *et al.,* "Small and similar amounts of micromotion in an anatomical stem and a customized cementless femoral stem in regular-shaped femurs. A 5-year follow-up randomized RSA study," *Acta Orthop.* vol. 85, no. 2, pp: 152-8, Apr. 2014. doi: /10.3109/17453674.2014.899846.

140. E. R. Valstar, R. G.H.H. Nelissen, J. H.C. Reiber, P. M. Rozing, "The use of Roentgen stereophotogrammetry to study micromotion of orthopaedic implants," *ISPRS Jol of Photogrammetry and Remote Sens.,* vol. 56, no. 5–6, pp. 376-389, Aug. 2002. doi: /10.1016/S0924-2716(02)00064-3.

141. A. F. Obaton *et al.,* "In vivo XCT bone characterization of lattice structured implants fabricated by additive manufacturing," *Heliyon*, vol. 3, no. 8, Sep 2017. doi: /10.1016/j.heliyon.2017.e00374

142. Q. Ran *et al.,* "Osteogenesis of 3D printed porous Ti6Al4V implants with different pore sizes," *Jol. of the Mech. Behav. of Biomed. Mater*., vol. 84. Apr. 2018. doi: /10.1016/j.jmbbm.2018.04.010.

143. N. Taniguchi *et al.,* "Effect of pore size on bone ingrowth into porous titanium implants fabricated by additive manufacturing: An in vivo experiment," *Mater. Sci. and Eng.: C*, vol. 59, pp. 690-701, Feb. 2016. doi: /10.1016/j.msec.2015.10.069.

144. J. Van der Stok *et al.,* "Selective laser melting-produced porous titanium scaffolds regenerate bone in critical size cortical bone defects," *Jol. of orthopaedic res*., vol. 31. no. 5, May. 2013. doi: /10.1002/jor.22293.

145. F. P.W. Melchels *et al.,*"Effects of the architecture of tissue engineering scaffolds on cell seeding and culturing," *Acta Biomaterialia,* vol. 6, no. 11, pp. 4208-4217, Nov. 2010. doi: /10.1016/j.actbio.2010.06.012.

146. Z. J. Wally, *et al.,* "Selective laser melting processed Ti6Al4V lattices with graded porosities for dental applications," *Jol. of the Mech. Behav. of Biomed. Mater.,* vol. 90, pp. 20-29, Feb. 2019. doi: /10.1016/j.jmbbm.2018.08.047.

147. H. Wang, K. Su, L. Su, P. Liang, P.Ji, C. Wang, "The effect of 3D-printed Ti6Al4V scaffolds with various macropore structures on osteointegration and osteogenesis: A biomechanical evaluation," *Jol. of the Mech. Behav. of Biomed. Mater.,* vol. 88, pp. 488-496, Dec. 2018. doi: /10.1016/j.jmbbm.2018.08.049.

148. P. K. Srivas *et al.,* "Osseointegration assessment of extrusion printed Ti6Al4V scaffold towards accelerated skeletal defect healing via tissue in-growth," *Bioprinting*, vol. 6, pp. 8-17, Jun. 2017. doi: /10.1016/j.bprint.2017.04.002.

149. K. H. Frosch *et al.,* "Growth behavior, matrix production, and gene expression of human osteoblasts in defined cylindrical titanium channels," *Jol. of Biomed. Mater. Res. Part A.,* vol. 68, no. 2, pp. 325-34. Feb. 2004. doi: /10.1002/jbm.a.20010.

150. S. F. Alves, T. Wassall, "In vitro evaluation of osteoblastic cell adhesion on machined osseointegrated implants," *Braz. oral res.,* vol. 23, no. 2, pp. 131-136, June. 2009. doi: /10.1590/S1806-83242009000200007.

151. S. C. Manolagas, "Birth and Death of Bone Cells: Basic Regulatory Mechanisms and Implications for the Pathogenesis and Treatment of Osteoporosis," *Endocrine Reviews*, vol. 21, no. 2, pp. 115–137, May. 2000. doi: /10.1210/er.21.2.115.

152. K. Tanaka-Kamioka,H. Kamioka, H. Ris, S. Lim, "Osteocyte Shape Is Dependent on Actin Filaments and Osteocyte Processes Are Unique Actin-Rich Projections," *J Bone Miner Res,* vol. 13, no. 10, pp. 1555-1568, Nov. 1998. doi: /10.1359/jbmr.1998.13.10.1555.

153. M. Pilia, T. Guda, S. M. Shiels, M. Appleford, "Influence of substrate curvature on osteoblast orientation and extracellular matrix deposition," Jol. of Biol. Eng., vol. 7, no. 1, pp. 23, Oct. 2013. doi: /10.1186/1754-1611-7-23.

154. E.A. Friis, A. K. Tsao, L. D. T. Topoleski, L. C. Jones, “1 - Introduction to mechanical testing of orthopedic implants,” *in Mechanical Testing of Orthopaedic Implants*, Woodhead Publishing, 2017, ch. 1, pp. 3-15.

155. “Global Orthopedic Devices Market 2016-2020,” TechNavio, London, London, Jan. 2016. Accessed: March. 2019. [Online]. Available: https://www.technavio.com/report/global-orthopedics-and-general-medical-devices-orthopedic-market

156. “The Impact of Obesity on Bone and Joint Health,” American Academy of Orthopaedic Surgeons, Rosemont, IL, USA, Mar. 2015. [Online]. Available: https://www.aaos.org/uploadedFiles/PreProduction/About/Opinion_Statements/position/1184%20The%20Impact%20of%20Obesity%20on%20Bone%20and%20Joint%20Health(1).pdf

157. “Obesity and overweight,” World Health Organization, Geneva, Switzerland, Feb. 2018. [Online]. Available: https://www.who.int/news-room/fact-sheets/detail/obesity-and-overweight

158. D. Williams, B. Isaacson, “The 5 Hallmarks of Biomaterials Success: An Emphasis on Orthopaedics,” *Adv. in Biosci. and Biotech.,* vol. 5, no. 4, pp. 283-293, Mar. 2014. doi: /10.4236/abb.2014.54035.

159. B. Isaacson, S. Jeyapalina, “Osseointegration: A review of the fundamentals for assuring cementless skeletal fixation,” *Ortho. Res. and Rev.,* Apr. 2014. doi: /10.2147/ORR.S59274.

160. “FDA Clears Additive Implants' 3D Printed SureMAX Cervical Spacer System,” Orthopedic Design & Technology. https://www.odtmag.com/contents/view_breaking-

news/2019-03-12/fda-clears-additive-implants-3d-printed-suremax-cervical-spacer-system/48605 (accessed Mar. 2019).

161. C. Lin, T. Wirtz, F. aMarca, S. Hollister, "Structural and mechanical evaluations of a topology optimized titanium interbody fusion cage fabricated by selective laser melting process," *Jol. of Biomed. Mater. Res. Part A.,* vol. 83, no. 2, pp. 272-9, Nov. 2007, doi: /10.1002/jbm.a.31231.

162. E. Hofheinz, "EIT: 510(k) Clearance for Full 3D Printed Spine Cage," Orthopedics This Week. https://ryortho.com/breaking/eit-510k-clearance-for-full-3d-printed-spine-cage/ (accessed Mar. 2019).

163. "K2M Enhances 3D-Printed Spine Portfolio Following FDA Clearance of Two CASCADIA™ Interbody Systems Featuring Lamellar 3D Titanium Technology™," K2M. http://investors.k2m.com/news-releases/news-release-details/k2m-enhances-3d-printed-spine-portfolio-following-fda-clearance (accessed Mar. 2019).

164. S. Davies, "Interview: FDA-approved 3D printed implants just the start as Osseus prepares to go international," tct Magazine, https://www.tctmagazine.com/3d-printing-news/fda-3d-printed-implants-osseus-international/ (accessed Mar. 2019).

165. M. Di Prima *et al.,* "Additively manufactured medical products – the FDA perspective," *3D Printing in Med.*, vol. 2, no. 1, Dec. 2016. doi: /10.1186/s41205-016-0005-9.

166. L. Scime, J. Beuth, "A multi-scale convolutional neural network for autonomous anomaly detection and classification in a laser powder bed fusion additive manufacturing process," *Ad. Manuf.,* vol. 24, pp. 273-286, Dec. 2018. doi: /10.1016/j.addma.2018.09.034.

167. J. zur Jacobsmühlen, S. Kleszczynski, G. Witt and D. Merhof, "Detection of elevated regions in surface images from laser beam melting processes," *IECON 2015 - 41st Annual Conference of the IEEE Industrial Electronics Society*, Yokohama, 2015, pp. 001270-001275.

168. S. Everton, M. Hirsch, P. Stravroulakis, R. Leach, A. Clare, "Review of in-situ process monitoring and in-situ metrology for metal additive manufacturing", *Mater. & Des.*, vol. 95, April. 2016. doi: /10.1016/j.matdes.2016.01.099.

169. M.A. Ali, R. Umer, K.A. Khan, S. Bickerton, W.J. Cantwell, "Non-destructive evaluation of through-thickness permeability in 3D woven fabrics for composite fan blade applications," *Aerosp. Sci. and Tech.,* vol. 82–83, pp. 520-533, Nov. 2018. doi: /10.1016/j.ast.2018.10.003.

170. S. Suresh Kumar, B. Ravisankar, "Destructive and non-destructive evaluation of copper diffusion bonds," *Jol. of Manuf. Processes,* vol. 23, pp. 13-20, Aug. 2016. doi: /10.1016/j.jmapro.2016.05.012.

171. H. Gong, *et al.,* Influence of defects on mechanical properties of Ti–6Al–4V components produced by selective laser melting and electron beam melting," *Mater. & Des*., vol. 86, pp. 545-554, Jul. 2015. doi: /10.1016/j.matdes.2015.07.147.

172. D. Ye, K. Zhu, J. Y. H. Fuh, Y. Zhang, H. G. Soon, "The investigation of plume and spatter signatures on melted states in selective laser melting," *Optics & Laser Tech.,* vol. 111, pp. 295-406, Apr. 2019. doi: /10.1016/j.optlastec.2018.10.019.

173. T. Craeghs *et al.,* "Determination of geometrical factors in Layerwise Laser Melting using optical process monitoring, Optics and Lasers in Engineering," vol. 49, no. 12, pp. 1440-1446, doi: /10.1016/j.optlaseng.2011.06.016.

174. M. Grasso, V. Laguzza, Q. Semeraro, B. Colosimo, “In-Process Monitoring of Selective Laser Melting: Spatial Detection of Defects Via Image Data Analysis,” *ASME. J. Manuf. Sci. Eng*. vol. 139, no. 5, Aug. 2016. doi: /10.1115/1.4034715

175. J. L. Bartlett, F. M. Heim, Y. V. Murty, X. Li, “In situ defect detection in selective laser melting via full-field infrared thermography,” *Additive Manuf.,* vol. 24, pp. 595-605, Dec. 2018. doi: /10.1016/j.addma.2018.10.045

176. T. Furumoto, T. Ueda, M.R. Alkahari, A. Hosokawa, “Investigation of laser consolidation process for metal powder by two-color pyrometer and high-speed video camera”, *CIRP Ann.,* vol. 62, no. 1, pp, 223–226, 2013. doi: /10.1016/j.cirp.2013.03.032.

177. S. Berumen, F. Bechmann, S. Lindner, J. P. Kruth, T. Craeghs, “Quality control of laser and powder bed-based Additive Manufacturing (AM) technologies,” *Phys. Procedia*, vol. 5, pp. 617–622, 2010. doi: /10.1016/j.phpro.2010.08.089

178. D. Ye, J. Y. H. Fuh, Y. Zhang, G. S. Hong, K. Zhu, “In situ monitoring of selective laser melting using plume and spatter signatures by deep belief networks,” *ISA Transactions*, vol. 81, pp. 96-104, Oct. 2018. doi: /10.1016/j.isatra.2018.07.021.

179. N Rajic, “Principal component thermography for flaw contrast enhancement and flaw depth characterisation in composite structures,” *Composite Struct.,* vol. 58, no. 4, pp. 521-528, Dec. 2002. doi: /10.1016/S0263-8223(02)00161-7.

180. A. Ning *et al.,* “Application of PCA in Concrete Infrared Thermography Detection," in *2nd Int. Workshop on Mater. Eng. and Comp. Sci*., 2015. [Online]. Available:

https://www.researchgate.net/publication/301462556_Application_of_PCA_in_Concrete_Infrared_Thermography_Detection

181. A. Krizhevsky, I. Sutskever, G.E. Hinton, “ImageNet classification with deep convolutional neural networks,” *Adv. Neural Inf. Process. Syst*., vol. 25, no. 2, Jan. 2012. doi: /10.1145/3065386

182. D. Aydogan, “CNNEDGEPOT: CNN based edge detection of 2D near surface potential field data,” *Comput. & Geosciences,* vol. 46, pg. 1-8, Sep. 2012. doi: /10.1016/j.cageo.2012.04.026

183. H. A. Atabay, “Binary shape classification using Convolutional Neural Networks,” *IIOAB Jol.,* vol. 7, pp. 332-336. 2017. [Online]. Available: https://www.iioab.org/articles/IIOABJ_7.S5_332-336.pdf

184. B. Graf, S. Ammer, A. Gumenyuk, M. Rethmeier,” Design of Experiments for Laser Metal Deposition in Maintenance, Repair and Overhaul Applications,” *Procedia CIRP*, vol. 11, pp. 245-248, 2013. doi: /10.1016/j.procir.2013.07.031.

185. Standard Test Methods for Tension Testing of Metallic Materials; ASTM E8/8M; ASTM, West Conshohocken, PA, USA, 2014. [Online]. Available: https://www.astm.org/Standards/E8.htm

186. Standard Test Methods of Compression Testing of Metallic Materials at Room Temperature; ASTM E9; ASTM, West Conshohocken, PA, USA, 2014. [Online]. Available: https://www.astm.org/Standards/E9

187. A. Mikołajczyk and M. Grochowski, "Data augmentation for improving deep learning in image classification problem," *2018 International Interdisciplinary PhD*

Workshop (IIPhDW), Swinoujście, 2018, pp. 117-122. doi: 10.1109/IIPHDW.2018.8388338

188. "CS231n Convolutional Neural Networks for Visual recognition," Stanford Univ. http://cs231n.github.io/convolutional-networks/ (accessed Apr. 2019).

189. B. Rohrer, "How do Convolutional Neural Networks work?," End-to-End Machine Learning Blod. http://brohrer.github.io/how_convolutional_neural_networks_work.html (accessed Apr. 2019).

190. N. Srivastava, G. Hinton, A. Krizhevsky, I. Sutskever, R. Salakhutdinov, "Dropout: A Simple Way to Prevent Neural Networks from Overfitting," *Jol. of Mach. Learning Res,* vol 15, pp. 1929-1958. [Online]. Available: http://www.jmlr.org/papers/volume15/srivastava14a/srivastava14a.pdf?utm_content=buffer79b43&utm_medium=social&utm_source=twitter.com&utm_campaign=buffer

191. "Improve Shallow Neural Network Generalization and Avoid Overfitting," MathWorks. https://www.mathworks.com/help/deeplearning/ug/improve-neural-network-generalization-and-avoid-overfitting.html (acessed Apr. 2019).

192. P. Skalski, "Preventing Deep Neural Network from Overfitting. Mysteries of Neural Networks Part II," Towards Data Science, Sep. 2018. https://towardsdatascience.com/preventing-deep-neural-network-from-overfitting-953458db800a (accessed Apr. 2019.)

193. "trainingOptions," MathWorks. https://www.mathworks.com/help/deeplearning/ref/trainingoptions.html (accessed Apr. 2019.)

194. Standard for Additive Manufacturing – Finished Part Properties – Standard Specification for Cobalt-28 Chromium-6 Molybdenum via Powder Bed Fusion; ASTM F3213; ASTM, West Conshohocken, PA, USA, 2014. [Online]. Available: https://www.astm.org/Standards/F3213.htm

195. Standard Specification for Cobalt-28 Chromium-6 Molybdenum Alloy Castings and Casting Alloy for Surgical Implants; ASTM F75; ASTM, West Conshohocken, PA, USA, 2014. [Online]. Available: https://www.astm.org/Standards/F75

196. Standard Specification for Wrought 18Chromium-14Nickel-2.5Molybdenum Stainless Steel Bar and Wire for Surgical Implants; ASTM F138; ASTM, West Conshohocken, PA, USA, 2014. [Online]. Available: https://www.astm.org/Standards/F138.htm

197. Technical Considerations for Additive Manufactured Medical Devices; U.S. Department of Health and Human Services, FDA, Silver Spring, MD, USA, 2017. [Online]. Available: https://www.fda.gov/downloads/MedicalDevices/DeviceRegulationandGuidance/GuidanceDocuments/UCM499809.pdf

198. H. Elwarfalli, D. Papazoglou, D. Erdahl, A. Doll, “In-situ Process Monitoring with Artificial Neural Networks,” Unpublished manuscript, Univ. of Dayton, Dayton, OH, USA, 2019.